Controlled manipulation of atoms in Rydberg quantum states for application in experiments with antihydrogen

Kontrollierte Manipulation von Atomen in Rydberg Quantenzuständen zur Anwendung in Experimenten mit Antiwasserstoff

Zur Erlangung des Grades eines Doktors der Naturwissenschaften (Dr. rer. nat.)
Genehmigte Dissertation von Tim Wolz aus Miltenberg a. Main
Tag der Einreichung: 16. November 2021, Tag der Prüfung: 15. Dezember 2021

1. Gutachten: Prof. Dr. Dr. h.c. mult. Norbert Pietralla
2. Gutachten: Chloé Malbrunot, PhD
Darmstadt, Technische Universität Darmstadt

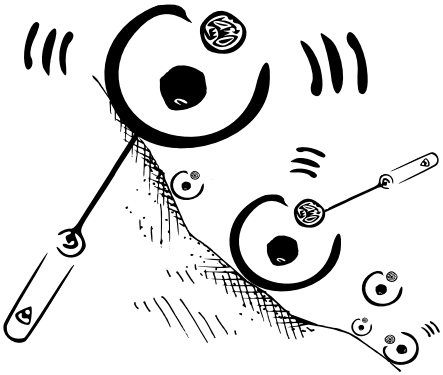

TECHNISCHE UNIVERSITÄT DARMSTADT

Fachbereich Physik
Institut für Kernphysik
AG Pietralla

Bundesministerium für Bildung und Forschung

Studienstiftung des deutschen Volkes

CERN

Controlled manipulation of atoms in Rydberg quantum states for application in experiments with antihydrogen
Kontrollierte Manipulation von Atomen in Rydberg Quantenzuständen zur Anwendung in Experimenten mit Antiwasserstoff

Genehmigte Dissertation von Tim Wolz

1. Gutachten: Prof. Dr. Dr. h.c. mult. Norbert Pietralla
2. Gutachten: Chloé Malbrunot, PhD

Tag der Einreichung: 16. November 2021
Tag der Prüfung: 15. Dezember 2021

Darmstadt, Technische Universität Darmstadt

Bitte zitieren Sie dieses Dokument als:
URN: urn:nbn:de:tuda-tuprints-203109
URL: http://tuprints.ulb.tu-darmstadt.de/20310

Dieses Dokument wird bereitgestellt von tuprints,
E-Publishing-Service der TU Darmstadt
http://tuprints.ulb.tu-darmstadt.de
tuprints@ulb.tu-darmstadt.de

Jahr der Veröffentlichung auf TUprints: 2022

Erklärungen laut Promotionsordnung

§8 Abs. 1 lit. c PromO

Ich versichere hiermit, dass die elektronische Version meiner Dissertation mit der schriftlichen Version übereinstimmt.

§8 Abs. 1 lit. d PromO

Ich versichere hiermit, dass zu einem vorherigen Zeitpunkt noch keine Promotion versucht wurde. In diesem Fall sind nähere Angaben über Zeitpunkt, Hochschule, Dissertationsthema und Ergebnis dieses Versuchs mitzuteilen.

§9 Abs. 1 PromO

Ich versichere hiermit, dass die vorliegende Dissertation selbstständig und nur unter Verwendung der angegebenen Quellen verfasst wurde.

§9 Abs. 2 PromO

Die Arbeit hat bisher noch nicht zu Prüfungszwecken gedient.

Darmstadt, 16. November 2021

T. Wolz

Zusammenfassung

Antiwasserstoffatome werden durch Ladungsaustausch oder Drei-Körper-Rekombination für CPT-Symmetrietests und Gravitationsmessungen mit Antimaterie am Antiprotonen-Entschleuniger des CERN synthetisiert. Während die Atome in einer Verteilung hochangeregter Rydberg-Zustände erzeugt werden, sind Experimente auf Antiwasserstoff im Grundzustand angewiesen. Dieser wird derzeit lediglich durch spontane Emission bevölkert. Aufgrund der Lebensdauer der Zustände in der Größenordnung von Millisekunden ist der Zerfall in den Grundzustand langsam.

Magnetische Fallen ermöglichen es, den produzierten Antiwasserstoff einzuschließen. Hier zerfallen Atome durch spontane Emission entlang des Fallenpotentials in den Grundzustand und Spektroskopiemessungen können innerhalb der Falle durchgeführt werden. Für Atome im Grundzustand liegen typische Fallentiefen bei Temperaturen von etwa 500 mK. Die Temperaturen nach der Antiwasserstoff-Synthese betragen aktuell jedoch etwa 40 K. Aufgrund dieser Diskrepanz liegt die derzeitige Effizienz mit der Antiwasserstoffatome in Fallen eingeschlossen werden können bei lediglich 10^{-4}.

Alternativ besteht die Möglichkeit die synthetisierten Atome in einem Strahl aus der Produktionsfalle zu extrahieren, was nahezu feldfreie Messungen ermöglicht. Bei den gegebenen Geschwindigkeiten ist der Zerfall der Rydbergzustände in den Grundzustand jedoch so langsam, dass durch spontane Emission selbst entlang eines mehrere Meter langen Strahlwegs keine signifikante Population des Grundzustands möglich ist. Darüber hinaus würde eine effiziente Strahlherstellung Antiwasserstoff im Grundzustand nahe der Produktionsfallen erfordern.

Diese Arbeit befasst sich folglich mit der kontrollierten Manipulation von Rydberg-Atomen, um ihren Zerfall in den Grundzustand gezielt zu stimulieren. Die anfängliche Verteilung von Rydberg-Niveaus wird durch gepulste elektrische Felder, die

zusätzlich zu dem bereits vorhandenen magnetischen Feld in der Produktionsfalle eingebracht werden, gemischt. Eine Alternative besteht darin, Zustandsmischung mit Licht im THz- und Mikrowellen-Frequenzbereich zu erreichen. In beiden Fällen können Laser eingesetzt werden, um sehr effizient Übergänge zu stark gebundenen Atomniveaus zu stimulieren, die innerhalb von wenigen Nanosekunden in den Grundzustand zerfallen.

Während einer Drei-Körper-Rekombination erlaubt der Einsatz von Lasern den Übergang von Positronen in einen gebundenen Zustand von Antiprotonen durch stimulierte Rekombination zu verstärken. Dieser Ansatz ist mit den entwickelten Techniken zur Abregung gebundener Niveaus kombinierbar. In Fallenexperimenten ermöglicht die Abregung innerhalb eines Feldgradienten außerdem Antiwasserstoff zu kühlen, um folglich den Anteil einfangbarer Atome zu erhöhen.

Der zweite Teil der Arbeit befasst sich mit der experimentellen Umsetzung der zuvor theoretisch untersuchten Methoden. Es werden Abregungslichtquellen getestet und ein angeregter Wasserstoff-Strahl für eine Machbarkeitsstudie konzeptioniert, aufgebaut und in Betrieb genommen. Verschiedene Verfahren zur Erzeugung von Rydberg-Zuständen werden diskutiert und experimentell ergründet. Die Bildung von hoch angeregten Zuständen in einem Wasserstoffplasma wird untersucht. Zur optischen Anregung von Rydberg-Niveaus in Wasserstoff wird ein Laser entwickelt.

Abstract

Antihydrogen atoms are synthesized via charge-exchange or three-body-recombination processes for stringent CPT symmetry and gravity tests on antimatter at CERN's Antiproton Decelerator. While the atoms are produced in a wide range of highly excited Rydberg states, experiments rely on ground state antihydrogen which are currently obtained only via spontaneous emission. Due to radiative lifetimes of the order of milliseconds, the decay toward ground state is slow.

Magnetic neutral-atom traps allow to hold onto the initially formed antihydrogen. Here, ground state atoms are obtained via spontaneous decay along the trapping potential and spectroscopy measurements can be performed inside the trap. Typical traps capture maximum temperatures (for ground state atoms) of roughly 500 mK. State-of-the-art formation temperatures, however, lie around 40 K. Due to the large difference between formation and trappable temperature, currently best achieved trapping fractions of antihydrogen amount to only 10^{-4}.

As an alternative, the formed anti-atoms can be extracted out of their formation region into a beam allowing for close to field-free measurements. At the given velocities, the Rydberg radiative decay toward ground state is too slow to establish a significant population of the ground state through spontaneous emission even within a few meter long beam path. In addition, an efficient beam formation would require antihydrogen in ground state close to the formation region.

This work thus deals with the controlled manipulation of Rydberg atoms to stimulate their decay toward ground state. In order to address the initial distribution of Rydberg levels with deexcitation lasers, state-mixing can be achieved through pulsed electric fields that are added to the already present magnetic one in state-of-the-art formation traps. Another possibility lies in mixing the states with light in the THz and microwave frequency range. In both cases, visible lasers allow to very

efficiently transfer the mixed population toward the ground state via intermediate strongly bound states that decay on a few nanosecond timescales.

In a three-body-recombination reaction the capture of positrons into a bound state of antiprotons can be enhanced relying on stimulated radiative recombination. This approach can be combined with the developed techniques to deexcite bound levels. In trap experiments use-cases of deexcitation for cooling within a magnetic field gradient to enhance the trapping fraction of antihydrogen atoms exist.

The second part of the thesis deals with the experimental implementation of the methods theoretically identified in part one. Deexcitation light sources are tested and a hydrogen Rydberg beamline for a proof-of-principle experiment is designed, built and commissioned. Different Rydberg beam production schemes are discussed and experimentally assessed. Rydberg state formation is observed within a microwave discharge plasma and a hydrogen 2s to Rydberg excitation laser is commissioned.

Acknowledgements

I would like to express my deepest gratitude to my supervisor C. Malbrunot for the relentless support and great mentoring throughout my PhD. Similarly, I would like to thank N. Pietralla for offering me the opportunity to pursue my studies at CERN linked to his group at Technische Universität Darmstadt.

A particular thank you goes to D. Comparat for countless very interesting discussions on this work's theory part and for contributing experimental equipment, most importantly the Rydberg excitation laser, through Laboratoire Aimé Cotton. A special word of thanks is also due to M. Simon from Stefan Meyer Institute for Subatomic Physics (SMI) for the great guidance and help throughout the project as well as the extensive design work on the experimental part.

I would like to acknowledge the simulation work done by C. Killian from SMI and the useful input from P. Chabert and C. Drag from Laboratoire de Physique des Plasmas at Ecole Polytechnique concerning radio-frequency plasma sources.

Thank you to the entire AEGIS and ASACUSA collaboration. I really enjoyed working with the students S. Lahs and P. Kulkarni.

I want to thank S. Auerbach, M. Farre, M. Munoz Codoceo, E. Dho, C. Decosse and S. Detraz for their support with the construction of the laser laboratory and the installation of the required safety equipment.

I am indebted to the "Bundesministerium für Bildung und Forschung" and the CERN responsible, M. Hauschild, for financing my PhD position through a Wolfgang Gentner scholarship. Further, I would like to express my gratitude to the "Studienstiftung des Deutschen Volkes" for supporting me as a doctoral scholar.

Thank you to my friends and housemates at CERN – I will keep many happy memories. A particular thank you goes to my office mates L. Nowak and E. Oswald

for the much appreciated mutual support. Similarly, I will be forever grateful to everybody back home for always welcoming me back as if I had never been away!

Most importantly, I would like to finally thank my parents and family for their incredible and unconditional support in simply everything I do.

Preface

As a member of the AEGIS and ASACUSA collaboration at CERN's Antiproton Decelerator complex my PhD work focuses on the controlled manipulation of Rydberg antihydrogen atoms.

Our group at CERN works on studies toward stimulated deexcitation of antihydrogen atoms. The theory has been investigated in collaboration with D. Comparat's group from Laboratoire Aimé Cotton (LAC) in Paris. For experimental work we additionally collaborated with the Stefan Meyer Institute for Subatomic Physics in Vienna.

I was in charge of studying the theory of light induced mixing and deexcitation of antihydrogen atoms. The results, including a first detailed study of stimulated radiative recombination in a magnetic field combined with deexcitation, are published in Physical Review A. I am the first author of this publication [1]. This work led to the group's realization of an error in a prior paper by D. Comparat and C. Malbrunot dealing with pulsed laser deexcitation via state mixing in crossed electric and magnetic fields [2]. I performed simulations which were published in the erratum [3].

I was a main contributor to studies dealing with stimulated deexcitation in the magnetic potential of neutral atom traps. The techniques investigated can lead to enhanced antihydrogen trapping fractions and lower temperatures critical for trap experiments at CERN's AD. The ideas are applicable in similar ways to other trapped species that can be efficiently deexcited. The studies will be submitted for publication soon [4].

Within ASACUSA, I performed detailed calculations of the field ionization process of antihydrogen in an electric field. The study was an essential part to understand

the quantum state distribution of the antihydrogen beam reported in [5]. The results clearly point out the need for stimulated deexcitation.

I was the main responsible of the group's efforts toward an experimental demonstration of stimulated deexcitation. I took the initiative to analyze data obtained by D. Comparat et al. in a proof-of-principle technology demonstration of suitable light sources for antihydrogen deexcitation on a Rydberg cesium beam. The results, put in the context of my prior theoretical work, have been published in European Physics Journal D. I am corresponding author of this paper [6]. Working toward a hydrogen proof-of-principle, I was responsible for setting up a new state-of-the-art laser laboratory from scratch. I designed and commissioned an atomic hydrogen beamline employing a microwave discharge plasma source to test deexcitation light sources. This included setting up the experimental control and data acquisition. Rydberg state formation has been observed, via electric field ionization, out of the discharge plasma. In addition, I commissioned an excitation laser at CERN to excite the meta-stable 2*s* beam toward Rydberg states.

Within ASACUSA I provided extensive technical and troubleshooting support to the team working on an atomic ground-state hydrogen beam for precision measurements of the ground state hyperfine splitting to constrain Standard Model Extension coefficients with matter.

I co-supervised two bachelor students (both DAAD scholars) working on atomic hydrogen sources (experiment) and Rydberg laser excitation (theory), respectively.

Contents

1 Introduction

The baryon asymmetry observed in our Universe is one of the most tantalizing mysteries that physics aims at solving. Despite the fact that antimatter and matter should have been created to equal amounts at the Big Bang, astronomical observations reveal the lack of large quantities of antimatter in the cosmos. Within the Standard Model (SM) of Particle Physics this dominance of matter remains a profound unanswered question on the way to ultimately explain the world we live in.

1.1 CPT and gravity tests with antimatter

The SM has a great history of predicting physical phenomena and so-far withstood experimental tests to exquisite precision. One of its key features is the use of symmetries to describe natural forces (except from gravity which can not yet be included in a quantum field theory approach) and particles. Among the most important discrete symmetry operators are the $\hat{P}$ transformation (inversion of space with respect to the origin), the charge conjugation $\hat{C}$ (sign flip of the charge) and time reversal $\hat{T}$. Whereas these symmetries were believed to be individually conserved by the laws of physics up to the 1950s, Wu et al. measured a P violation in beta-decays in 1957 [7]. While Wu's experiment still conserved the combined CP symmetry, Cronin and Fitch evidenced CP violation in 1964 when discovering that the possibility of K-mesons to transform into their antiparticle counterparts is not exactly the same as for the inverse process i.e. the antiparticle transforming into its particle counterpart [8]. CP violation was proposed to be part of a possible explanation of the absence of primordial antimatter in the Universe by Sakharov in 1976 [9]. Even though since then other sources of CP violation have been

discovered, the so far measured effects are too small to explain astronomical observations.

Another possibility lies in the violation of the combined CPT symmetry [10] which can be probed by directly comparing matter and antimatter properties. In this quest a completely new field of physics, the precision study of anti-atom properties, has emerged at the European Organisation for Nuclear Research (CERN). Following major milestones in antimatter research like the discovery of the positron [11], the production of antiprotons [12] and antineutrons [13] as well as the first synthesis of relativistic antihydrogen ($\overline{\mathrm{H}}$) atoms in 1996 [14], experiments at the Antiproton Decelerator (AD) complex [15] at CERN nowadays regularly produce $\overline{\mathrm{H}}$ atoms for precision measurements. First observations of atomic transitions in $\overline{\mathrm{H}}$ atoms ($1s \rightarrow 2s$ [16] and $1s \rightarrow 2p$ [17]) have been published. Measurements of the fine and hyperfine structure as well as the Lamb shift in $\overline{\mathrm{H}}$ are reported in [18, 19].

In addition to stringent CPT tests, the coupling of antimatter to Earth's gravitational field remains hitherto unprobed. Indeed, the universality of free fall is a cornerstone in our understanding of gravitation that was first observed by Galileo and later promoted by Einstein to a fundamental axiom around which he developed the theory of general relativity. Collaborations at the AD aim for a precise measurement of Earth's acceleration of $\overline{\mathrm{H}}$ atoms. In this context, an electrically neutral atomic system is favorable over charged particles that are sensitive to electric and magnetic stray fields. Compared to other neutral antimatter systems like positronium (Ps), a bound state of an electron and a positron, $\overline{\mathrm{H}}$ atoms are stable as well as comparatively massive ($m_{\overline{\mathrm{H}}} \approx 2000 \times m_{\mathrm{Ps}}$) and thus less sensitive to residual field gradients in the measurement region. Most importantly, $\overline{\mathrm{H}}$ is the simplest atom made up entirely of antimatter. Although first rough bounds have been put onto the acceleration of $\overline{\mathrm{H}}$ atoms in Earth's gravitational field [20], to date no precise direct measurement exists.

1.2 State-of-the-art in antihydrogen experiments at CERN

Precision measurements require ground state $\overline{\mathrm{H}}$ atoms. The anti-atoms, however, are produced at CERN in a wide range of highly excited Rydberg states. The

lifetime of such initially populated $\overline{\mathrm{H}}$ levels can be approximated by [21]

$$\tau_{n,l} \approx \left(\frac{n}{30}\right)^3 \left(\frac{l+1/2}{30}\right)^2 \times 2.4\,\mathrm{ms}, \tag{1.1}$$

where n and l are the principal and angular quantum numbers, respectively. Thus, especially high angular momentum Rydberg states exhibit long lifetimes of several milliseconds (for $n \sim 30$).

Experiments relying on neutral atom traps can hold onto the formed $\overline{\mathrm{H}}$ and therefore acquire ground-state atoms through spontaneous emission along the trapping field gradient. Currently, best achieved formation temperatures lie around $\sim 40\,\mathrm{K}$ [22] which corresponds to a mean velocity of $\sim 1000\,\mathrm{m\,s^{-1}}$. State-of-the-art ground state trap depths, however, are typically of the order of 500 mK resulting in trapping fractions of only $\sim 0.04\,\%$ [22].

Another possibility lies in the formation of an atomic beam to extract the $\overline{\mathrm{H}}$, away from the formation trap, into a close to field free region for measurements. Antihydrogen atoms have been readily detected several meters away from the electric and magnetic fields of their formation region, but in highly excited states and at very low rates (at best a few atoms per trial) [23]. Due to the combination of high formation temperatures and long radiative lifetimes, spontaneous emission does not allow for a significant population of the ground state – even after a few meter long beam path. Beam formation through techniques like, for example, magnetic focusing is a complex interplay of atomic temperature, quantum state distribution and many additional parameters. The latter depend on spontaneous emission, the atoms' exact trajectories through the apparatus and parasitic background when detecting $\overline{\mathrm{H}}$ outside the formation region. A theoretical study of the processes at play as well as simulations of the signal to noise ratio for different initial quantum state distributions and velocities are provided in [24]. The formation of a beam through inhomogeneous electric fields, so-called Stark acceleration as proposed in [25], suffers from similar problems resulting, for a broad initial distribution of states, in an inefficient beam formation that can not be afforded in view of the currently achieved $\overline{\mathrm{H}}$ production rates [26].

1.2.1 Pulsed antihydrogen production via resonant CE

$\overline{\mathrm{H}}$ atoms can be synthesized relying on a single or double charge-exchange (CE) reaction as reported by the AEGIS [26] and ATRAP [27] collaboration, respectively. Both $\overline{\mathrm{H}}$ production schemes are illustrated in Fig. 1.1.

Making use of a single CE reaction, an excited positronium (Ps^*) atom, a bound state of an electron (e^-) and a positron (e^+), releases its positive charge to an antiproton ($\overline{\mathrm{p}}$) to form antihydrogen

$$\overline{\mathrm{p}} + \mathrm{Ps}^* \rightarrow \overline{\mathrm{H}}^* + \mathrm{e}^-. \tag{1.2}$$

Ps can be produced by accelerating positrons that are emitted from a radioactive ^{22}Na source toward a nano-channeled silica target. The impinging positrons enter the target via pores that permeate its surface and eventually fall into a meta-stable bound state with electrons. The formed Ps is then liberated into the vacuum via the same nano-channels the positrons entered through. Lasers are used to excite the formed Ps atoms to boost the $\overline{\mathrm{H}}$ formation cross section. Indeed, the $\overline{\mathrm{H}}$ production rate for ground-state Ps is too small to be detected and the formation cross section $\sigma_{\overline{\mathrm{H}}}$ scales as n_{Ps}^4, where n_{Ps} is the Ps main quantum number. Antiprotons made available by the AD complex at CERN are confined in a Penning-Malmberg trap. The two species are brought together in a $\overline{\mathrm{H}}$ formation region where magnetic fields of typical values around 1 T are present.

In a double CE reaction Ps^* is formed via an intermediate resonant collision of a positron with an alkaline atom (e.g. cesium)

$$\mathrm{Cs}^* + \mathrm{e}^+ \rightarrow \mathrm{Ps}^* + \mathrm{Cs}^+. \tag{1.3}$$

The Cs atoms can be produced out of an effusive oven and guided through a cloud of trapped positrons. Lasers are used, this time to excite Cs, to boost the reaction cross section to form Ps^*. The Ps^* then releases its positron which in turn bounds with an antiproton as described in Eq. 1.2 to form $\overline{\mathrm{H}}^*$. The main advantage of the double CE is the use of stable Cs atoms that are, compared to Ps synthesis using a porous target, relatively easy to produce and manipulate.

In both cases, either single or double CE, the excitation lasers provide a time stamp allowing for a pulsed $\overline{\mathrm{H}}$ production. Further, a CE reaction offers the possibility to control the $\overline{\mathrm{H}}$ binding energy through the Ps quantum state targeted by the

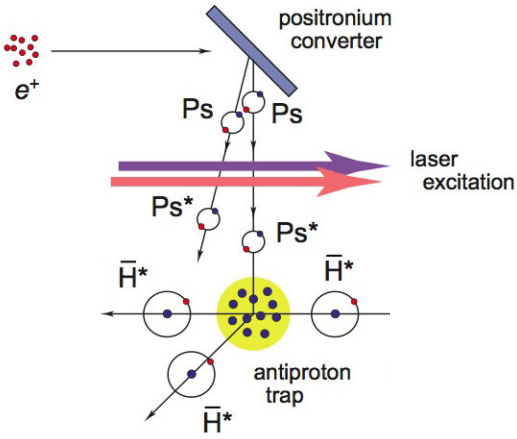

(a)

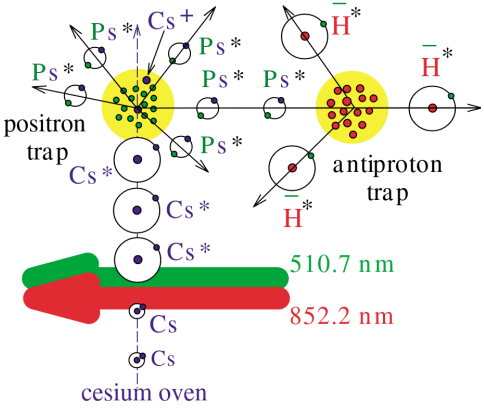

(b)

Figure 1.1: Schematics of $\overline{\mathrm{H}}$ formation via single (a) and double (b) CE reaction. Reprinted from [28] and [27] respectively.

excitation lasers. Due to energy conservation, the $\overline{\mathrm{H}}$ principal quantum number follows the relation $n_{\overline{\mathrm{H}}} = \sqrt{2} n_{\mathrm{Ps}}$ (cf. Fig. 4.4 in [25]). Typically targeted values[1] lie around $n_{\mathrm{Ps}} \sim 20$ and result in $n_{\overline{\mathrm{H}}} \sim 30$. The spread of the produced $\overline{\mathrm{H}}$ in n mainly depends on the velocity and the velocity distribution of the Ps [29–31]. Classical trajectory Monte Carlo (CTMC) simulations have been performed to investigate the $\overline{\mathrm{H}}$ quantum state distribution as a function of the Ps level. Whereas the latter is usually well defined due to laser excitation (at least when relying on a single CE), the distribution of angular momentum in $\overline{\mathrm{H}}$ is generally very large (cf. Fig. 4.5 and 4.6 in [25]).

In addition to the main advantage of having a pulsed production scheme, the formation of $\overline{\mathrm{H}}$ via CE can in principle lead to very cold atomic samples. Indeed, the formed atoms can be expected to be roughly as cold as the $\overline{\mathrm{p}}$ because the Ps^* only transfers little kinetic energy (at maximum a few tens of $\mathrm{m\,s^{-1}}$ in terms of $\overline{\mathrm{H}}$ velocity in typical experimental conditions) throughout the formation process. Sympathetic cooling schemes for $\overline{\mathrm{p}}$ [32] with e^- that cool via cyclotron radiation are commonly employed in state-of-the-art experiments and can lead, if required also in combination with adiabatic cooling, to $\overline{\mathrm{p}}$ temperatures of a few K. Much lower temperatures are still an experimental challenge. Novel techniques for sympathetic cooling involving laser-cooled molecular or atomic anions are current topic of research [33, 34].

1.2.2 Continuous antihydrogen production via 3BR

An alternative $\overline{\mathrm{H}}$ production scheme is the so-called three-body-recombination (3BR). Here, a positron and an antiproton plasma are kept in interaction for a duration of typically several hundreds of milliseconds [23]. Within the plasma, the $\overline{\mathrm{H}}$ production process requires two positrons, one of which carries away the binding energy that is released when the other one falls into a bound state with an antiproton to form antihydrogen

$$\mathrm{e}^+ + \mathrm{e}^+ + \overline{\mathrm{p}} \rightarrow \bar{\mathrm{H}}^* + \mathrm{e}^+. \tag{1.4}$$

[1] In the AEGIS [25] experiment, other limitations that are mainly due to motional Stark ionization led to the choice of $n_{\mathrm{Ps}} = 17$ and thus $n_{\overline{\mathrm{H}}} \sim 24$.

The $\overline{\mathrm{H}}$ formation and evolution process is a complex interplay of various radiative and collisional inter-particle and photon-particle interactions. Particle collisions occur inside the formation plasma until the formed atoms have traveled out of the formation region of a few millimeter size. Radiative processes are stimulated by either a finite temperature blackbody radiation field emitted from the surrounding experimental apparatus or external light sources that can be installed for targeted quantum state manipulation of the formed $\overline{\mathrm{H}}$ atoms as proposed in this work. Table 1.1 summarizes the main mechanisms at play.

Theoretical considerations [35–37] indicate that the formed $\overline{\mathrm{H}}$ atoms cover a broad range of n-manifolds up to $n \sim 100$. Despite the current experimental conditions which do not allow to precisely study the distribution of levels, some in-situ [38] and beam [5, 39] measurements confirmed the presence of highly excited states in large quantities. Levels with $n \geq 50$ are expected to be ionized by the electric field present at the edge of the formation plasma [23, 40, 41]. Thus, a broad distribution of states up to $n = 50$ (with all sublevels populated) can be assumed to exit the formation plasma.

$\overline{\mathrm{H}}$ can be produced by confining a cold positron and antiproton plasma inside, for example, a nested Penning-Malmberg trap. Antiprotons provided by the AD are, in a first step, sympathetically cooled by electrons that efficiently emit cyclotron radiation due to their comparatively small mass. Evaporative cooling [42] then allows to obtain, in the case of the ALPHA experiment [22], $\sim 10^5$ antiprotons at $\sim 40\,\mathrm{K}$. In parallel, some 10^6 positrons emitted from a radioactive source are trapped. Techniques to control the density and spatial extension of the plasma are applied before the particles are left to thermalize with their surroundings to temperatures between 15 to 20 K. Antihydrogen atoms are formed as soon as the species are brought into contact. In early experiments, the trapped $\overline{\mathrm{p}}$ were transferred into the e^+ cloud with kinetic energies of many eV (cf. [43] or the so-called direct injection employed in ASACUSA [44]). An improved adiabatic beam transport in ASACUSA is reported in [45]. The ALPHA collaboration developed a technique to either merge $\overline{\mathrm{p}}$ and e^+ by carefully manipulating the respective trapping potentials or by autoresonant excitation of the longitudinal $\overline{\mathrm{p}}$ motion inside the trap [46] such that they can transfer into the positron cloud. In both cases and in contrast to the mentioned prior experiments, positrons and antiprotons can here be expected to thermalize throughout the recombination process [47, 48]. Consequently, the $\overline{\mathrm{H}}$ mainly carries over the positron velocity and a colder positron

Mechanism	Detailed process
Three-body recombination	$\overline{\mathrm{p}} + \mathrm{e}^+ + \mathrm{e}^+ \rightarrow \overline{\mathrm{H}}^* + \mathrm{e}^+$
Collisional (de-)excitation and mixing	$\overline{\mathrm{H}}^* + \mathrm{e}^+ \rightarrow \overline{\mathrm{H}}^{**} + \mathrm{e}^+$
Collisional ionization	$\overline{\mathrm{H}}^* + \mathrm{e}^+ \rightarrow \overline{\mathrm{p}} + \mathrm{e}^+ + \mathrm{e}^+$
Radiative recombination	$\overline{\mathrm{p}} + \mathrm{e}^+ \rightarrow \overline{\mathrm{H}}^* + h\nu$
Stimulated radiative recombination	$\overline{\mathrm{p}} + \mathrm{e}^+ + h\nu \rightarrow \overline{\mathrm{H}}^* + 2\,(h\nu)$
Photoionization	$\overline{\mathrm{H}}^* + h\nu \rightarrow \overline{\mathrm{p}} + \mathrm{e}^+$
Spontaneous radiative decay	$\overline{\mathrm{H}}^* \rightarrow \overline{\mathrm{H}}^{**} + h\nu$
Stimulated radiative (de-)excitation and mixing	$\overline{\mathrm{H}}^* + h\nu \rightarrow \overline{\mathrm{H}}^{**} + 2\,(h\nu)$

Table 1.1: Mechanisms involved in the 3BR antihydrogen formation process. Excited quantum states are indicated by a * superscript. The ** superscript indicates an excited quantum state different from the initial * one.

plasma would result in slower and thus more trappable $\overline{\mathrm{H}}$. So far best achieved temperatures, that are determined via the fraction of trapped and formed $\overline{\mathrm{H}}$ atoms, amount to $\sim 40\,\mathrm{K}$ [22]. In the quest toward the production of colder antihydrogen, an experimental demonstration of sympathetic cooling of positrons relying on laser cooled Be^+ ions has just been recently published [49]. Temperatures of 7 K have been achieved at rather high $\mathrm{e}^+/\mathrm{Be}^+$ ratios of 10 which is crucial to minimize antiproton capture of Be^+.

A quite general and comprehensive review on the production of antihydrogen atoms as well as the physics investigated is available in, for example, [15, 50].

1.3 Thesis outline

The previous sections laid down the current state-of-the-art in antihydrogen experiments at CERN. In summary, $\overline{\mathrm{H}}$ atoms are formed at best formation temperatures of $\sim 40\,\mathrm{K}$ corresponding to mean velocities of $1000\,\mathrm{m\,s^{-1}}$ and in a broad range of long-lived Rydberg states whereas precision experiments require atoms in ground

state. In order to ensure an efficient beam formation, the atomic temperature and quantum state distribution has to be controlled. For trap experiments, cold $\overline{\mathrm{H}}$ is of particular importance in view of spectroscopy measurements where the atomic spectra experience a shift due to the varying magnetic field strength.

Techniques to stimulate the decay of the formed Rydberg levels toward ground state to enhance the number of atoms available for measurements have been a long standing issue. Past studies relying on the sole use of deexcitation lasers [51] were found to be inefficient since high angular momentum states, that are incidentally the most populated ones, can not be addressed. Making use of half-cycle pulses resulted in roughly 10 % of the $n = 50$ population in ^{85}Rb to be deexcited to $n < 40$ [52]. The transfer was slow ($\sim$ 150 µs) due to the lack of powerful light. On the other side, addressing the temperature problem, first laser cooling of ground state antihydrogen via the 1s $\rightarrow$ 2p transition has been reported in [17, 53]. Despite difficulties such as the lack of powerful light sources and spectral transition shifts within the trap potential, the median transverse atomic kinetic energy could be reduced by more than an order of magnitude to submicroelectronvolts. While cooling was only one-dimensional, the trap coupled the longitudinal and transverse motion resulting in a cooling of all three dimensions. It is, however, important to again emphasize that 1s $\rightarrow$ 2p laser cooling only addresses ground state atoms. Thus, the currently achievable trapping fraction of only $\sim$0.04 % [22] remains unchanged. Further, the cooling procedure is quite lengthy lasting several hours.

New ideas to provide larger samples of cold $\overline{\mathrm{H}}$ in ground state are needed. Chapter 2 lays down the theoretical framework required to simulate and assess the efficiency of enhancing the population of the ground state with a (visible) deexcitation laser right after formation in the presence of electric and/or magnetic fields or other light. The obtained simulation results are presented in chapter 3 including both pulsed and continuous deexcitation methods. Initially populated Rydberg states can be mixed either via crossed electric and magnetic fields or relying on THz and microwave light. In a 3BR scheme, deexcitation of bound levels can be combined with stimulated radiative recombination (srr) which was first proposed in [54] to directly form anti-atoms in ground state. In this work, combined srr and deexcitation schemes are presented. Detailed simulations of latter ideas are laid down, for the first time in a magnetic field environment, in section 3.4. Further, the stimulated deexcitation techniques developed have the potential to enhance, within a trap magnetic field gradient, the number of finally trapped atoms. A dedicated

discussion can be found in subsection 3.5.3. Chapter 4 treats experimental efforts toward a hydrogen proof-of-principle experiment. A discussion on the suitability of different light sources for Rydberg state mixing and deexcitation is followed by the report on a proof-of-principle using cesium atoms. Building upon this, atomic hydrogen and Rydberg beam production is investigated both in theory and experiment. The conclusions drawn in chapter 5 put the presented research into context evaluating its impact on the field and establishing connections to other disciplines and applications.

2 Theoretical background of antihydrogen deexcitation

This chapter establishes a common basis required for further considerations when modeling and simulating the atomic processes at hand. In particular, the interaction of atoms with light in external fields is treated. Section 2.1 lays down the derivation of energy levels and transition dipoles for the following two cases:

1. Crossed electric and magnetic fields are of interest in the context of $\overline{\mathrm{H}}$ formation relying on CE production. This case is developed in subsection 2.1.1.
2. $\overline{\mathrm{H}}$ atoms in pure magnetic fields are treated in subsection 2.1.2 within the context of 3BR. Here, the full (anti-)hydrogenic Hamiltonian is diagonalized to obtain energy levels and transition dipoles.

Rate equations are derived and their use, in the framework considered throughout this thesis, is justified in section 2.2.

2.1 Rydberg antihydrogen atoms in external fields

Atomic properties of (anti-)hydrogen can be calculated by solving the time independent three-dimensional Schrödinger equation

$$E\psi = -\frac{\hbar^2}{2m}\nabla^2\psi + V\psi, \tag{2.1}$$

where ψ_n are the spatial wavefunctions that define the complete set of stationary states by $\Psi_n(\boldsymbol{r},t) = \psi_n(\boldsymbol{r})\, e^{-iE_n t/\hbar}$ and $V(\boldsymbol{r}) = -\frac{e^2}{4\pi\epsilon_0}\frac{1}{r}$ is the hydrogenic

Coulomb potential. The complete derivation of the solution is, for example, available in [55]. Here, only the main results will be recapitulated to establish common ground for the following considerations.

The potential $V(\boldsymbol{r})$ varies as a function of the distance from the point of origin. Using spherical coordinates (r, Θ, Φ), a separation of variable allows to isolate an angular and radial part of Eq. 2.1. Solving the angular dependent part leads to spherical harmonics $Y_{lm}(\Theta, \Phi)$, where $l = 0, 1, 2, \ldots$ and $m = -l, -l+1, \ldots, -1, 0, 1, \ldots, l-1, l$. This angular dependent part $Y(\Theta, \Phi)$ of the solution is the same for all radially symmetric potentials. Thus, the actual shape of the potential V is only taken into account solving the radially dependent part of the Schrödinger equation that leads to the allowed energy levels given by Bohr's famous formula

$$E_n = -\left(\frac{m}{2\hbar}\left(\frac{e^2}{4\pi\epsilon_0}\right)^2\right)\frac{1}{n^2} = \frac{E_1}{n^2}, \qquad n = 1, 2, 3, \ldots \tag{2.2}$$

where $E_1 = -13.6\,\mathrm{eV}$. The radially dependent part of the wavefunction $R_{n,l}(r)$ that now allows to assemble the solution of the original Schrödinger equation can be written as $\psi_{nlm}(r, \Theta, \Phi) = R_{nl}(r)\, Y_{lm}(\Theta, \Phi)$ with the commonly used principal, angular and magnetic quantum numbers n, l and m. The R_{nl} term of the hydrogenic wavefunction is given, using calligraphic notation ($\mathcal{R}_{nl}$ or $\mathcal{R}_{El}$) for SI units and usual typography (R_{nl} or R_{El}) for atomic units, by

$$\begin{aligned} R_{nl}(\rho) &= \frac{2}{n^2} e^{-\frac{\rho}{n}} \sqrt{\frac{(n-l-1)!}{(l+n)!}} \left(\frac{2\rho}{n}\right)^l L_{n-l-1}^{2l+1}\left(\frac{2\rho}{n}\right) \\ &= \frac{2}{n^2(2l+1)!} e^{-\frac{\rho}{n}} \sqrt{\frac{(l+n)!}{(n-l-1)!}} \left(\frac{2\rho}{n}\right)^l \times \\ &\qquad \times {}_1F_1\left(l-n+1; 2l+2; \frac{2\rho}{n}\right), \end{aligned} \tag{2.3}$$

where the Bohr radius $a_0 = \frac{4\pi\epsilon_0\hbar^2}{m_e e^2}$, $\mathcal{R}_{nl}(r) = \frac{1}{a_0^{3/2}} R_{nl}(r/a_0)$ and $\rho = r/a_0$. F denotes the hypergeometric function and L the associated Laguerre polynomials. The functions are normalized : $1 = \int_0^\infty R_{nl}(r)^2 r^2 dr = \int_0^\infty \mathcal{R}_{nl}(\rho)^2 \rho^2 d\rho$.

The Wigner-Eckart theorem indicates that dipole $\boldsymbol{d} = e\boldsymbol{r}$ matrix elements between $|nlm\rangle$ and $|n'l'm'\rangle$ states are given, with commonly used Clebsch-Gordan coefficients, by [2, 3]

$$\begin{aligned}\langle n'l'm'|r^{(q)}/a_0|nlm\rangle &= C^{l'm'}_{lm,1q}\frac{\langle n'l'\|r/a_0\|nl\rangle}{\sqrt{2l'+1}} \\ &= C^{l'm'}_{lm,1q}C^{l'0}_{l0,10}\frac{\sqrt{2l+1}}{\sqrt{2l'+1}}R^{n'l'}_{nl}.\end{aligned} \tag{2.4}$$

The radial overlap $R^{n'l'}_{nl} = \int_0^\infty R_{nl}(\rho)\rho R_{n'l'}(\rho)\rho^2 d\rho = \mathcal{R}^{n'l'}_{nl}/a_0$ is given by [56]

$$\begin{aligned}R^{n'l-1}_{nl} &= \frac{(-1)^{n'-l}}{4(2l-1)!}\sqrt{\frac{(l+n)!\,(l+n'-1)!}{(-l+n-1)!\,(n'-l)!}}\frac{(4nn')^{l+1}(n-n')^{n+n'-2l-2}}{(n+n')^{n+n'}}\times \\ &\quad\times\left({}_2F_1\left(a_1,a_2,a_3,a_4\right) - \frac{(n-n')^2}{(n'+n)^2}\,{}_2F_1\left(a_5,a_2,a_3,a_4\right)\right) \quad \forall n \neq n' \\ R^{n'l-1}_{nl} &= \frac{3}{2}n\sqrt{n^2-l^2} \quad \forall n = n'\end{aligned} \tag{2.5}$$

with the hypergeometric function arguments

$$\begin{aligned}a_1 &= l-n+1 \\ a_2 &= l-n' \\ a_3 &= 2l \\ a_4 &= -\frac{4nn'}{(n-n')^2} \\ a_5 &= l-n-1.\end{aligned} \tag{2.6}$$

From Eq. 2.2 one can directly derive the atomic transition photon energy from an initial state i toward a target state j. Since the photon energy $E_\gamma = h\nu$ and $\lambda = c/\nu$ one finds Rydberg's formula

$$\frac{1}{\lambda} = \frac{Ry}{hc}\left(\frac{1}{n_{\mathrm{j}}^2} - \frac{1}{n_{\mathrm{i}}^2}\right), \tag{2.7}$$

with $R_\infty \sim 1.097 \times 10^7 \mathrm{m}^{-1}$ and the Rydberg constant $Ry = hcR_\infty \sim 13.6\,\mathrm{eV}$. It is noteworthy to mention that this formula was already empirically derived in the 19th century to explain hydrogen spectroscopy measurements. Bohr only succeeded in the early 1900s to relate Rydberg's fitting parameter to natural constants $R_\infty = \frac{m}{4\pi c\hbar^3}\left(\frac{e^2}{4\pi\epsilon_0}\right)^2$. The Rydberg formula describes atomic states with high principal quantum number n where the electron is, on average, far from the nucleus. For such so-called Rydberg states the electron can be treated as a classical particle. Applying Newton's second law and balancing the forces experienced by an electron in circular orbit (speed v) around an infinitely heavy nucleus leads to $\frac{mv^2}{r^2} = \frac{ke^2}{r^2}$, with $k = 1/4\pi\epsilon_0$. Adding the angular momentum quantization $mvr = n\hbar$ gives $r = \frac{n^2\hbar^2}{e^2 mk}$. Thus, the atom's radius scales with n^2 and the geometrical cross section[1] with n^4. Due to their extreme size, Rydberg atoms exhibit high electric dipole moments $d \propto a_0 n^2$ allowing for their acceleration in inhomogeneous electric fields [57], the Stark acceleration referred to in section 1.2. Similarly, high n Rydberg states with large magnetic quantum number m (most prominently circular states with $l = |m| = n - 1$) have an increased magnetic dipole moment $\mu \propto m$ (and $-n + 1 \leq m \leq n + 1$). Thus, they interact more strongly with external magnetic fields.

2.1.1 Antihydrogen in crossed E and B fields

As later detailed in section 3.2, a pulsed laser deexcitation of $\overline{\mathrm{H}}$ atoms formed via CE can be realized via state mixing of Rydberg states through an additional pulsed electric field [2, 3]. This field is added to the already present magnetic one which exhibits typical strengths of 1 T. Here, the calculation of the energy levels and required transition dipoles in such a field configuration is laid down in view of the simulation results presented in chapter 3.

Following the field value perturbation theory approach developed in [58], the

[1] For CE $\overline{\mathrm{H}}$ production schemes, the geometrical cross section is boosted via excitation to high n states to assure high atomic interaction probabilities, cf. section 1.2.

Hamiltonian can be written for a given n manifold, in atomic units, as

$$H_n = -\frac{1}{2n^2} + \underbrace{\boldsymbol{r}\cdot\boldsymbol{F}}_{\text{lin. Stark}} + \underbrace{(\boldsymbol{r}\cdot\boldsymbol{F})\,G_n\,(\boldsymbol{r}\cdot\boldsymbol{F})}_{\text{quadr. Stark}} + \underbrace{\frac{1}{2}\boldsymbol{B}\cdot\boldsymbol{L}}_{\text{paramagnetic}} - \underbrace{\frac{1}{8}(\boldsymbol{r}\times\boldsymbol{B})^2}_{\text{diamagnetic}}, \qquad (2.8)$$

where $\boldsymbol{F}$ and $\boldsymbol{B}$ are the electric and magnetic field vectors, G_n the Green operator of the field free hydrogen atom H_0 and $\boldsymbol{L} = \boldsymbol{r}\times\boldsymbol{p}$ the angular momentum. The first and second order Stark and Zeeman terms are of the order of $(B+3nF)n/2$ and $n^6F^2 + n^4B^2/4$ respectively [58–60]. Thus, for the presently treated case where $n \leq 35$ and $B \sim 1\,\mathrm{T}$, the second order reaches values that are by an order of magnitude smaller than the first order terms for $F \sim 500\,\mathrm{V\,cm^{-1}}$. In the following, the second order terms will be consequently neglected and the Hamiltonian simplifies to $H_n = -\frac{1}{2n^2} + \boldsymbol{r}\cdot\boldsymbol{F} + \frac{1}{2}\boldsymbol{B}\cdot\boldsymbol{L}$.

Hydrogen in crossed E and B fields was already studied by Pauli in 1926 [61]. He identified, for a given n manifold, two vector matrices $\boldsymbol{I}_1 = \frac{\boldsymbol{L}+\boldsymbol{A}}{2}$ and $\boldsymbol{I}_2 = \frac{\boldsymbol{L}-\boldsymbol{A}}{2}$, with $\boldsymbol{A} = \frac{1}{\sqrt{-2H_0}}\left[\frac{1}{2}(\boldsymbol{p}\times\boldsymbol{L} - \boldsymbol{L}\times\boldsymbol{p}) - \frac{\boldsymbol{r}}{r}\right]$ being the Runge-Lenz vector, that commute and obey the commutation relations for angular momentum operators. Their norm $|\boldsymbol{I}_1| = |\boldsymbol{I}_2| = \frac{1}{2}\sqrt{n^2-1}$. In the new basis $|I_1 m_1\rangle \otimes |I_2 m_2\rangle$ the eigenvalues m_1 and m_2 range from $-\frac{n-1}{2}, -\frac{n-3}{2}, \cdots$ to $\cdots \frac{n-3}{2}, \frac{n-1}{2}$. Taking $\boldsymbol{\omega}_1 = \frac{\boldsymbol{B}-3n\boldsymbol{F}}{2}$ and $\boldsymbol{\omega}_2 = \frac{\boldsymbol{B}+3n\boldsymbol{F}}{2}$ the linear terms from Eq. 2.8 can be written as $\boldsymbol{r}\cdot\boldsymbol{F} + \frac{1}{2}\boldsymbol{B}\cdot\boldsymbol{L} = \boldsymbol{\omega}_1\cdot\boldsymbol{I}_1 + \boldsymbol{\omega}_2\cdot\boldsymbol{I}_2$. This can easily be diagonalized and leads to the first order energy correction

$$\Delta E^{(1)}_{m_1 m_2} = \omega_1 m_1 + \omega_2 m_2, \qquad (2.9)$$

where $\omega_i = \|\boldsymbol{\omega}_i\|$ and m_1 (m_2) is the projection of $\boldsymbol{I}_1$ ($\boldsymbol{I}_2$) on $\boldsymbol{\omega}_1$ ($\boldsymbol{\omega}_2$). Fig. 2.1 illustrates the definition of the $\boldsymbol{\omega}_1$, $\boldsymbol{\omega}_2$, $\boldsymbol{I}_1$ and $\boldsymbol{I}_2$ vectors. In addition, α_1 and α_2, the angles between the magnetic field axis and $\boldsymbol{\omega}_1$ (and $\boldsymbol{\omega}_2$ respectively), are shown.

In pure electric fields the linear Stark effect is restored $\Delta E^{(1)}_{m_1 m 2} = \frac{3}{2}nF(m_1+m_2)$. In the parabolic basis $|n,k,m\rangle$ (that is linked to $\hat{H}, \hat{A}_z, \hat{L}_z$), $k = -(m_1+m_2)$ and $m = m_2 - m_1$ [2, 3]. Similarly, in the case of a pure magnetic field, the linear Zeeman shift $\Delta E^{(1)}_{m_1 m 2} = \frac{1}{2}B(m_1+m_2)$ is restored where $m_1 + m_2 = m$ because $\boldsymbol{I}_1 + \boldsymbol{I}_2 = \boldsymbol{L}$. It is important to note that, when using such a (m_1, m_2) formalism, the states will always be given in a parabolic basis. This is different from the

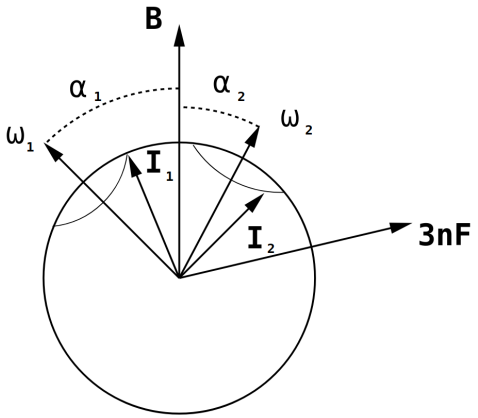

Figure 2.1: Illustration of the vectors $\boldsymbol{\omega}_1$, $\boldsymbol{\omega}_2$, α_1, α_2, $\boldsymbol{I}_1$ and $\boldsymbol{I}_2$ that are used in perturbation theory. Reprinted from [58].

spherical $|nlm\rangle$ one, so even in a pure magnetic field the eigenstates $|nm_1m_2\rangle$ will not correspond to the $|nlm\rangle$ ones: l is mixed in the $|nm_1m_2\rangle$ basis [2, 3].

Fig. 2.2 shows ΔE that has been derived in Eq. 2.9 for some selected sublevels of the $n = 20$, $n = 25$ and $n = 30$ manifolds. The simulations in section 3.2 are performed using the field configuration that was identified in [2, 3] to optimally mix the states in the $n = 30$ manifold that are typically targeted in a CE $\overline{\text{H}}$ formation process. It is therefore meaningful to anticipate this result (electric field of 280 V cm^{-1} with a crossing angle of 160° with respect to the already present 1 T magnetic one) and plot energy levels that will be of interest in the following. In Fig. 2.2, the electric field is fixed to 280 V cm^{-1} and the energy shift is shown as a function of the strength of the crossed magnetic field. For readability reasons the diagrams' symmetry (Fig. 2.2a, 2.2b, 2.2c) with respect to $\Delta E = 0$ is exploited and only states with $\Delta E > 0$ are plotted. To again avoid plotting too many levels, only uneven or even (chosen in such a way that the maximum energy shift is visible) $m_1 + m_2$ states are shown.

In Fig. 2.3 the magnetic field is now fixed as well to 1 T and not only the energy correction resulting from the perturbation theory outlined above, but the total

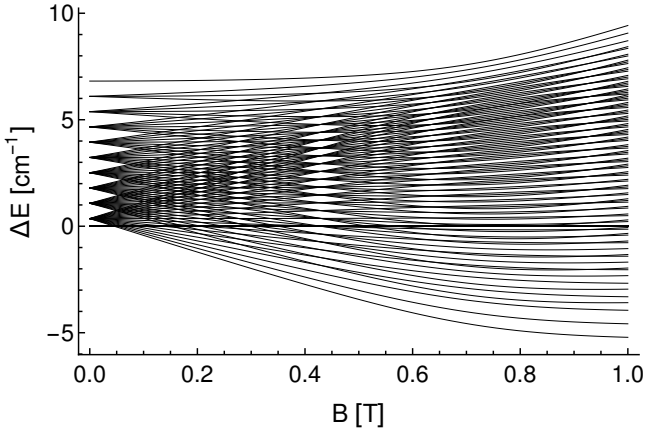

(a) Energy shift for the sublevels (even m) of the $n = 20$ manifold

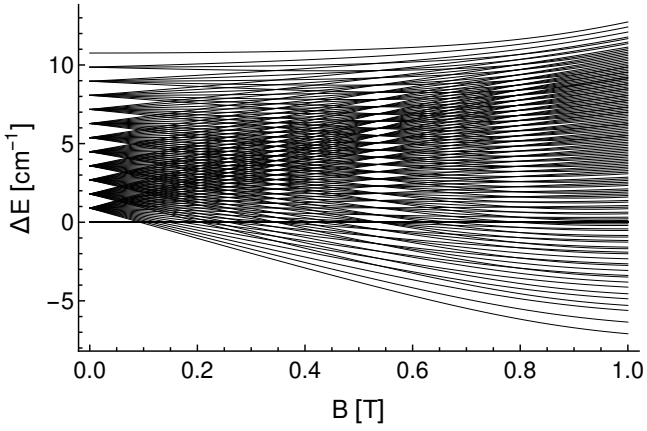

(b) Energy shift for the sublevels (uneven $m_1 + m_2$) of the $n = 25$ manifold

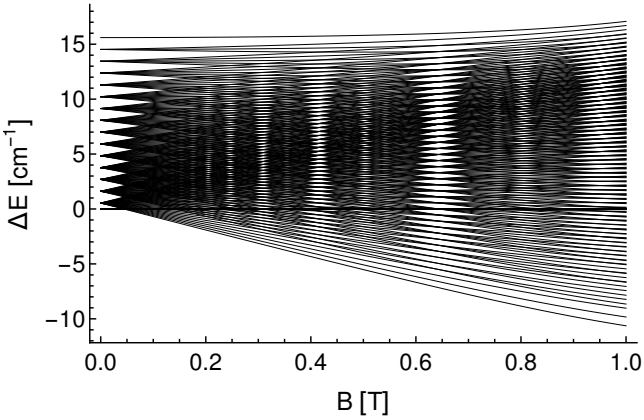

(c) Energy shift for the sublevels (uneven $m_1 + m_2$) of the $n = 30$ manifold

Figure 2.2: First order energy shift as a function of the magnetic field strength in a crossed electric field of 280 V cm^{-1}. The angle between the electric and magnetic field vectors is 160°. For readability reasons only levels with $m_1 + m_2 \geq 0$ are plotted.

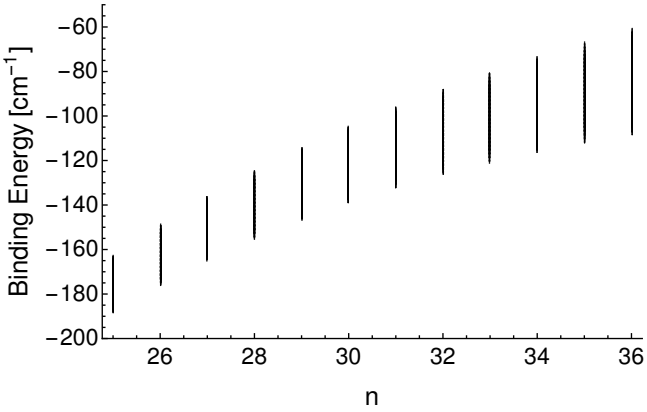

Figure 2.3: Range of binding energies from all (m_1, m_2) substates as a function of n in a 1 T magnetic and 280 V cm^{-1} electric field. The angle between the electric and magnetic field vectors is 160°.

binding energy of the states is shown. Here, all (m_1, m_2) sublevels are plotted to identify the energy overlap of the n manifolds. This will be crucial when investigating the transition frequencies of the Rydberg levels toward low lying n' manifolds that will be addressed by a deexcitation laser in section 3.2.1.

Using the Wigner D rotation matrix (Eq. 1.4 (35) [62]), one can express

$$|I_1 m_1\rangle_{\boldsymbol{\omega}_1} = \sum_{m_1'=-I_1}^{m_1'=I_1} D^{I_1}_{m_1,m_1'}(0,\alpha_1,0)|I_1 m_1'\rangle_{\boldsymbol{B}}$$

and similarly

$$|I_2 m_2\rangle_{\boldsymbol{\omega}_2} = \sum_{m_2'=-I_2}^{m_2'=I_2} D^{I_2}_{m_2,m_2'}(0,\alpha_2,0)|I_2 m_2'\rangle_{\boldsymbol{B}},$$

where the $\boldsymbol{\omega}_1$ ($\boldsymbol{\omega}_2$) subscript indicates that, again, m_1 (m_2) is the projection of I_1 (I_2) onto the $\boldsymbol{\omega}_1$ ($\boldsymbol{\omega}_2$) axis. The subscript $\boldsymbol{B}$ indicates that the quantization axis z is along $\boldsymbol{B}$.

With real Clebsch-Gordan coefficients and using the real small Wigner d-matrix:

$$d^{I_2}_{m_2,m'_2}(\alpha_2) = D^{I_2}_{m_2,m'_2}(0,\alpha_2,0)$$

and $d^{I_1}_{m_1,m'_1}(\alpha_1) = D^{I_1}_{m_1,m'_1}(0,\alpha_1,0)$ results in

$$\begin{aligned}
|nm_1m_2\rangle_{\boldsymbol{\omega}_1,\boldsymbol{\omega}_2} \equiv |I_1m_1\rangle_{\boldsymbol{\omega}_1}|I_2m_2\rangle_{\boldsymbol{\omega}_2} &= \sum_{l=0}^{n-1}\sum_{m=-l}^{l}\langle nlm|nm_1m_2\rangle|nlm\rangle_{\boldsymbol{B}} \\
\langle nlm|nm_1m_2\rangle \equiv \sum_{m'_1=-I_1}^{m'_1=I_1=\frac{n-1}{2}} &\sum_{m'_2=-I_2}^{m'_2=I_2=\frac{n-1}{2}} d^{I_1}_{m_1,m'_1}\left(\alpha_1^{(n)}\right) d^{I_2}_{m_2,m'_2}\left(\alpha_2^{(n)}\right)\times \\
&\times C^{lm}_{I_1m'_1,I_2m'_2},
\end{aligned} \tag{2.10}$$

where $|I_1m_1\rangle_{\boldsymbol{B}}|I_2m_2\rangle_{\boldsymbol{B}} = \sum_{ml} C^{lm}_{I_1m_1,I_2m_2}|nlm\rangle_{\boldsymbol{B}}$ is used. The subscript in $\alpha_1^{(n)}$ stresses that the angles depend on n and not only on the field values. Finally, one can now write the transition dipole from a given (n,m_1,m_2) level toward a (n',l',m') level as

$$d_{nm_1m_2\to n'l'm'} = \langle n'l'm'|r^{(q)}|nlm\rangle\langle nlm|nm_1m_2\rangle e, \tag{2.11}$$

where $\langle n'l'm'|r^{(q)}|nlm\rangle$ is the field free transition dipole from unperturbed levels (n,l,m) toward (n',l',m') ones. It is, in the framework of the simulations performed in section 3.2, sufficient to calculate the new dipoles in the crossed field configuration toward levels in the unperturbed (n',l',m') basis because the target levels will be strongly bound (for example $n'=3$) and thus their diamagnetic spread will be negligible.

2.1.2 Antihydrogen in pure magnetic fields

Formation of $\overline{\mathrm{H}}$ atoms via 3BR involves plasma mixing with delicate electric field manipulations within, for example, a Penning trap over several hundreds of milliseconds. Thus, state mixing relying on additional pulsed electric fields with modest strengths as identified in section 3.2 cannot be applied. Mixing of the

initially populated Rydberg levels via microwave and THz radiation, however, is possible and simulation results are laid down in section 3.3. The involved energy levels and transition dipoles are derived in the following. As pointed out before, it is important to note that within the trap additional small electric fields are required, but the high plasma conductivity and the resulting efficient redistribution of space charge prevent the penetration of such fields through the $\overline{\mathrm{H}}$ formation region. Further, the field strengths are comparatively small. The derivations below consequently consider only the present magnetic field.

In the presently treated regime ($B \sim 1\,\mathrm{T}$ and $n \sim 30$) spin-orbit effects can be neglected because $\frac{B}{1\,\mathrm{T}} n^3 > 24$ [63] and m can be considered a good quantum number. In the given configuration, the energy spacing between consecutive n manifolds is smaller than the intra-manifold energy spread introduced by the diamagnetic Zeeman shift. Thus, n can be considered an approximately good quantum number as long as $\left(\frac{n}{40}\right)^7 < \left(\frac{B}{1\,\mathrm{T}}\right)^{-2}$. For such an inter-$l$ mixing regime, the (anti-)hydrogenic Hamiltonian is given, again in atomic units, by [64]

$$H_{\mathrm{i,j}} = \left(-\frac{1}{2n_{\mathrm{i}}^2} + \underbrace{\frac{m_e a_0^2}{\hbar^2}\mu_B m B}_{\text{paramagnetic}} \right) \delta_{\mathrm{i,j}} + \underbrace{\frac{1}{8}\beta^2 H_{\mathrm{i,j}}^Q}_{\text{diamagnetic (Q for “quadratic”)}} , \tag{2.12}$$

where $\beta = \frac{B}{B_0}$ with $B_0 = \frac{2\alpha^2 m_e^2 c^2}{e\hbar} \sim 4.7\,\mathrm{T}$. Here, the explicit matrix notation was employed where the entries $H_{\mathrm{i,j}} = \langle \mathrm{i}|r^2 \sin^2\vartheta|\mathrm{j}\rangle = \langle nm|r^2\sin^2\vartheta|n'm'\rangle$ are given in polar coordinates r and ϑ by

$$\begin{aligned}
H_{\mathrm{i,j}}^Q &= \frac{1}{8}\beta^2 \frac{2}{3}\left(1 + \frac{3m - l\,(l+1)}{(2l+3)\,(2l-1)}\right)\langle nl|r|n'l'\rangle \\
&\qquad\qquad \forall l' = l \wedge m' = m \wedge n' = n \\
H_{\mathrm{i,j}}^Q &= \left[\frac{(l_< + m + 2)\,(l_< + m + 1)\,(l_< - m + 2)\,(l_< - m + 1)}{(2l_< + 5)\,(2l_< + 3)^2\,(2l_< + 1)}\right]^{\frac{1}{2}} \langle nl|r|n'l'\rangle \\
&\qquad\qquad \forall l' = l - 2m \wedge m' = m \\
H_{\mathrm{i,j}}^Q &= 0 \quad \text{otherwise.}
\end{aligned} \tag{2.13}$$

The symbol $l_<$ denotes the lesser of l and l' and the radial overlap $\langle nl|r^t|n'l'\rangle$ (here

with $t = 1$) of the wavefunctions is given by [65, 66]

$$\langle nl|r^t|n'l'\rangle = 2^{l+l'+2}\sqrt{\frac{(n'-l'-1)!\,(n'+l')!\,(n+l)!}{(n-l-1)!}}\,\frac{n^{1+t+l'}n'^{1+t+l}}{(n+n')^{3+t+l+l'}}\times$$
$$\times\sum_{p=0}^{n'-l'-1}\frac{(1+t-l+l'+p)!}{p!\,(n'-l'-1-p)!\,(2l'+1+p)!}\left(\frac{-2n}{n+n'}\right)^p\times$$
$$\times\frac{1}{(1+t-l+l'+p)!}\sum_{q=0}^{n-l-1}\binom{n-l-1}{q}\times$$
$$\times\frac{(2+t+l+l'+p+q)!}{(2l+1+q)!}\left(\frac{-2n'}{n+n'}\right)^q. \tag{2.14}$$

Since n and m are considered to be good quantum numbers, the Hamiltonian matrix can be diagnoalized independently for each set of (n, m) states. The resulting new levels are then labeled by an index k (with $|m| \leq k < n$) according to the magnitude of the state's diamagnetic interaction. It is however noteworthy to point out that k is just a label and does not describe a physical property. In Fig. 2.4 the resulting binding energies of antihydrogen Rydberg levels are plotted as a function of m. The energy shift resulting from the para- and diamagnetic term in Eq. 2.12 are clearly visible. The paramagnetic contribution results in an energy shift linearly proportional to m ($\mu_B B m$, where μ_B is the Bohr magneton), corresponding, in a 1 T field, to ~ 14 GHz. Further, the diamagnetic term shifts the energy of the states within a given n manifold. The effect is comparatively small (a few tens of GHz within the treated regime), but will be crucial for the considerations laid down in section 3.3. The diamagnetic contribution increases with n and is primarily visible for low m states. Intra-n manifold atomic transitions in the microwave region and inter-n manifold transitions in the THz region are indicated with curly and continuous arrows respectively. Some examples of spontaneous emission are illustrated by dashed arrows. The bottom right box in Fig. 2.4 points out that, due to the electric dipole selection rules $\Delta m = 0, \pm 1$, for circular states only a single $\Delta n = \pm 1$ is possible. Thus, when accelerating the decay of a Rydberg state distribution to ground state one can already conclude here that all $\Delta n = \pm 1$ transitions have to be addressed. This is especially crucial because these are the states with the longest lifetimes (cf. Eq. 1.1).

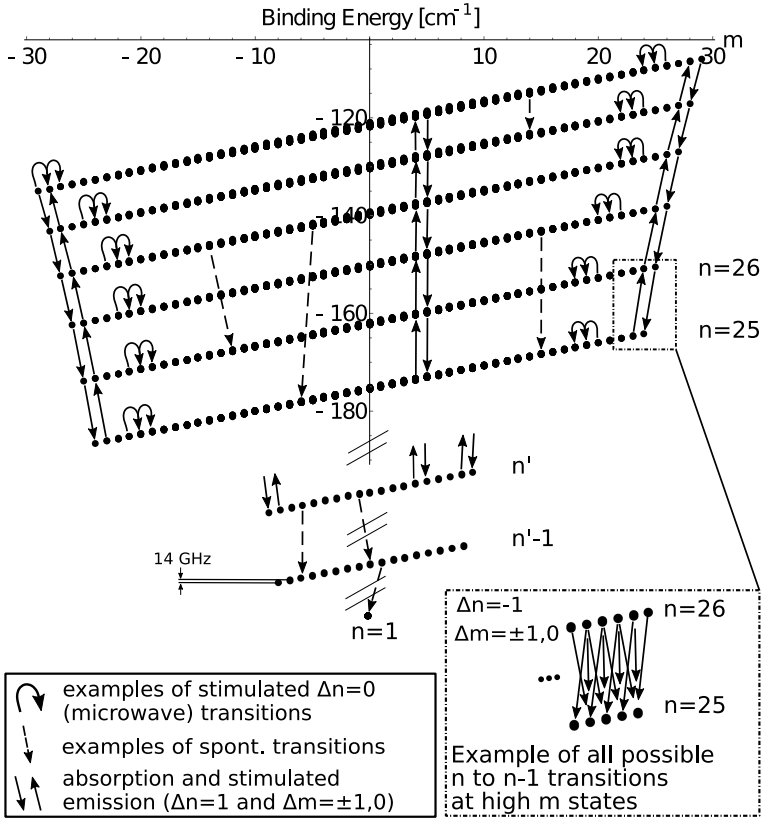

Figure 2.4: Transitions and binding energy diagram of hydrogen levels as a function of the magnetic quantum number m in a 1 T magnetic field. The stimulated $\Delta m = 0, \pm 1$ transitions are represented by continuous arrows. Microwave transitions with $\Delta n = 0$ are indicated by curly arrows. Some examples of spontaneous decays are indicated by dashed arrows. Reprinted from [1].

For the crossed electric and magnetic field configuration it was sufficient to calculate dipoles from the mixed Rydberg states toward a low lying ($n = 2$ or $n = 3$) unperturbed manifold which are the transitions that can directly be addressed with a deexcitation laser. Here, in contrast, all field free dipoles (especially from the high n (n, l, m) states to $(n'l'm')$ ones, where the effect of the field is the largest) need to be transferred to the new basis to simulate light stimulated Rydberg state mixing in section 3.3. In the zero field basis $|n\rangle^0$ a transition dipole $d^0_{1,2}$ between a state $|n_1\rangle^0$ and a state $|n_2\rangle^0$ is given by $\langle n_1|\hat{d}|n_2\rangle^0$. The transition dipole $d_{1,2}$ between a state $|n_1\rangle$ and a state $|n_2\rangle$ in the new basis $|n\rangle = \sum_{n,n_0} c_{n,n_0}|n\rangle^0$ can then be expressed by

$$\langle n_1|\hat{d}|n_2\rangle = \sum_{l,l'} c_{n_1,n_1^0} \sum_{l,l'} c_{n_2,n_2^0} \times d^0_{1,2} \tag{2.15}$$

where $c_{n_1,n_1^0} = \langle nkm|nlm\rangle$ and $c_{n_2,n_2^0} = \langle n'k'm'|n'l'm'\rangle$ with the introduced quantum numbers and level labels. This finally leads, in the new (n, k, m) basis, to transition dipoles in the presence of a pure magnetic field

$$d_{nkm\to n'k'm'} = \langle nkm|\hat{d}|n'k'm'\rangle = \sum_{l,l'} \langle nkm|nlm\rangle\langle nlm|\hat{d}|n'l'm'\rangle\langle n'l'm'|n'k'm'\rangle. \tag{2.16}$$

Fig. 2.5 shows the sole diamagnetic energy spread of all (k, m) sublevels of the $n = 20$ manifold. In contrast to Fig. 2.4, where both linear ($\Delta E \approx 0.5\,\mathrm{THz}$ for $n = 30$) and quadratic ($\Delta E \approx 30\,\mathrm{GHz}$ for $n = 30$) Zeeman shift are illustrated, this plot allows to depict intra-manifold transitions between the states which are shown as lines connecting the levels. The thickness of these lines scales with the strength of the transition dipole squared. Since in a magnetic field l is not a good quantum number anymore, the only selection rule is $\Delta m = 0, \pm 1$ which results in a mixing of angular momenta primarily visible for low m states.

2.2 Stimulated and spontaneous atomic transitions

The interaction of atoms with light can be treated in a semi-classical approach outlined, for example, in [67]. The impinging light will be treated as a classical electric field whereas quantum mechanics will be used to describe the atom.

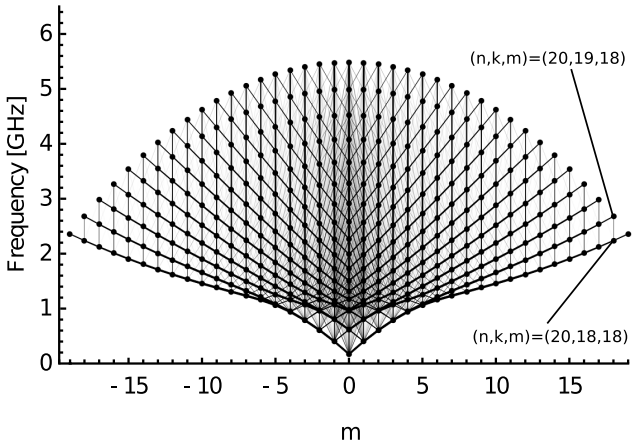

Figure 2.5: Shift of energy levels of all (k, m) sublevels (with respect to the $(k, m) = (0, 0)$ state) of the $n = 20$ manifold due to the sole diamagnetic term in a 1 T magnetic field. The thickness of the lines between states scales with the strength of the corresponding transition dipoles squared. Reprinted from [1].

Referring back to the Schrödinger equation (cf. Eq. 2.1), the wavefunction of an atomic two-level system (with levels $|\mathrm{i}\rangle$ and $|\mathrm{j}\rangle$) can be expressed as a superposition of $\psi_\mathrm{i}(\boldsymbol{r})\, e^{-iE_\mathrm{i}t/\hbar}$ and $\psi_\mathrm{j}(\boldsymbol{r})\, e^{-iE_\mathrm{j}t/\hbar}$

$$\Psi(\boldsymbol{r},t) = c_\mathrm{i}(t)\,\psi_\mathrm{i}(\boldsymbol{r})\, e^{-iE_\mathrm{i}t/\hbar} + c_\mathrm{j}(t)\,\psi_\mathrm{j}(\boldsymbol{r})\, e^{-iE_\mathrm{j}t/\hbar}, \tag{2.17}$$

where, for normalization reasons, $|c_\mathrm{i}(t)|^2 + |c_\mathrm{j}(t)|^2 = 1$. The light oscillating electric field $\boldsymbol{E} = \boldsymbol{E}_0 \cos(\omega t)$ introduces a perturbation H' to the field free Hamiltonian H_0 so that $H = H_0 + H'$, where $H' = e\boldsymbol{r} \cdot \boldsymbol{E}_0 \cos(\omega t)$. The coefficients c_i and c_j or, in other words, the mixing of the states due to the electric field are determined by the differential equations (Eq. 7.9 and 7.10 of [67])

$$\begin{aligned} i\dot{c}_\mathrm{i} &= \Omega \cos(\omega t)\, e^{-i\omega_0 t} c_\mathrm{j} \\ i\dot{c}_\mathrm{j} &= \Omega^* \cos(\omega t)\, e^{i\omega_0 t} c_\mathrm{i}, \end{aligned} \tag{2.18}$$

where $\omega_0 = (E_\mathrm{j} - E_\mathrm{i})/\hbar$ and the Rabi frequency $\Omega = \frac{e}{\hbar}\int \psi^*(r)\boldsymbol{r} \cdot \boldsymbol{E_0}\psi_2(r)\mathrm{d}^3 r$. Solving the system of equations under the assumption that at $t = 0$ one of the two levels is fully populated whereas the other one is completely vacant leads to a solution that contains a $1/(\omega_0 - \omega)$ and $1/(\omega_0 + \omega)$ term the latter of which can be neglected since the detuning of the impinging radiation from the atomic transition frequency is assumed to be small (rotating wave approximation). In order to study the case of broadband light one considers radiation of density $\rho(\omega)$ in an interval $\omega + \mathrm{d}\omega$ which is a narrow, almost monochromatic, slice of the entire distribution. The exact calculations are laid down from Eq. 7.17 to 7.20 in [67] and lead to a transition rate

$$\Gamma_{\mathrm{i}\to\mathrm{j}} = \frac{|c_2(t)|^2}{t} = \frac{\pi e^2 |X_{\mathrm{i}\to\mathrm{j}}|^2}{\epsilon_0 \hbar^2}\rho(\omega_0), \tag{2.19}$$

where $X_{\mathrm{i}\to\mathrm{j}} = \langle \mathrm{i}|x|\mathrm{j}\rangle$. The results found via this quantum mechanical approach can be compared to the $B_{\mathrm{i}\to\mathrm{j}}$ (upward stimulated) and $B_{\mathrm{j}\to\mathrm{i}}$ (downward stimulated) coefficients Einstein already found in 1917 relying on classical arguments in the radiative equilibrium of a two level system [68]. This leads to the transition rates $\Gamma_{\mathrm{i}\to\mathrm{j}} = \rho(\omega_0) B_{\mathrm{i}\to\mathrm{j}}$ and $\Gamma_{\mathrm{j}\to\mathrm{i}} = \rho(\omega_0) B_{\mathrm{j}\to\mathrm{i}}$ with

$$B_{\mathrm{i}\to\mathrm{j}} = \frac{g_\mathrm{j}}{g_\mathrm{i}} B_{\mathrm{j}\to\mathrm{i}} = \frac{\pi e^2 |D_{\mathrm{i}\to\mathrm{j}}|^2}{3\epsilon_0 \hbar^2}, \tag{2.20}$$

where g_i and g_j denote the level degeneracies. The factor $\frac{1}{3}$ difference between $|D_{\mathrm{i}\to\mathrm{j}}| = \langle 1|\boldsymbol{r}|2\rangle$ and $|X_{\mathrm{i}\to\mathrm{j}}|$ originates from an averaging over the three spatial coordinates.

The interaction of light with atoms can be accurately described using rate equations where population transfer is determined by the coefficients derived above under the following conditions: first, the light must be broadband and thus incoherent such that the spectral width exceeds the stimulated atomic transition line [69]. Another condition is low saturation as derived in [70] so that the saturation parameter

$$s = \frac{2|\Omega_{\mathrm{i}\to\mathrm{j}}|^2}{4\left(\omega_{\mathrm{i}\to\mathrm{j}} - \omega_\mathrm{L}\right)^2 - \Gamma_\mathrm{L}^2} \ll 1,$$

with the Rabi frequency $\Omega_{\mathrm{i}\to\mathrm{j}}$, transition frequency $\omega_{\mathrm{i}\to\mathrm{j}}$, laser frequency ω_L and laser bandwidth Γ_L. The simulations throughout this thesis are performed within this framework. This simplification enables the simulation of atomic processes involving a large number (up to ten thousands) of Rydberg states as performed in this work (specifically in chapter 3). For reasons of computing effort, solving the temporal evolution of the full density matrix ρ including the off-diagonal coherences ρ_{12} and ρ_{21} for such a large number of states is very hard.

A common issue to be considered when deriving rate equations to describe atom-light interaction is the possible formation of dark states that cannot absorb or emit photons. Dark states can result from quantum interference processes (so-called coherent population trapping) [71] that are generally not taken into account when dealing with atomic transition rates. A second mechanism, that is in general correctly described by the theory laid down earlier, is linked to the impinging light polarization. Indeed, photons that interact with electrons in the atomic shell, obey rules of total angular momentum conservation. Thus, for an initial and final atomic total angular momentum vector $\vec{J}_i$ and $\vec{J}_f$, $\vec{J}_f = \vec{J}_i + \vec{J}_\mathrm{photon}$, where $\vec{J}_\mathrm{photon}$ denotes the photon angular momentum. This is often referred to as the triangular rule. As a consequence, light of different polarization (linear π or left/right circular polarized $\sigma^\pm$) exclusively drives atomic transitions with $\Delta m = 0$ and $\Delta m = \pm 1$[2] which can lead to dark states that cannot absorb photons due to the triangular selection rules.

[2] In fact, Eq. 2.19 was derived under the assumption of π polarized light.

Population trapping is of particular importance in the context of this work, where a large distribution of states is deexcited to ground state. However, there are a variety of arguments, why the formation of dark states is, in the setting of the work presented throughout this thesis, at worst a minor effect:

- The formation of dark states through spontaneous emission [72] toward a level that is decoupled from the light sent to deexcite or mix the population is negligible due to the long lifetimes of the addressed states. The process under investigation takes place on the µs timescale whereas the initial Rydberg levels exhibit lifetimes of the order of ms. As the level population is driven toward lower lying states (the average lifetime scales as n^5), such an effect might become more relevant. However, possibly formed dark states (and the population trapped therein) would rapidly decay to ground state which is what one seeks to achieve.

- From an experimental point of view, amplified spontaneous emission (ASE) sources (that might be used for the generation of the THz radiation required to mix and/or deexcite Rydberg states) can very effectively prevent the generation of dark states due to the incoherent and unpolarized nature of the produced light. [73].

- Population trapping in dark states that are formed due to light polarization is unlikely to occur in arbitrary atomic systems and in general one can assume that transitions toward other states exist (cf. Table 1 in [74]). Concerning the experimental implementation, the light polarization will at best be local due to the use of multiple light sources, reflections within the apparatus, etc. Additionally, this work mainly treats isotropic ($\frac{1}{3}\sigma^+, \frac{1}{3}\sigma^-, \frac{1}{3}\pi$) light polarization. To strengthen the results and conclusions drawn, the isotropic case was compared to the use of linear and circular light polarization which is a case that necessarily leads to dark states formation. It was found that the results on stimulated deexcitation presented in the following varied by $\sim 5\,\%$ when using only circular polarized light. Further, the simulation outcomes obtained when only relying on linear polarized radiation varied by less than $\sim 10\,\%$.

2.2.1 Spontaneous emission rates

Spontaneous emission does not occur in the semi-classical approach outlined above to derive transition rates stimulated by light. However, referring back to the mentioned Einstein coefficients and considering a two level system in thermal equilibrium, the probability of up and downward transitions must balance out. With Eq. 2.20, this argument leads to the following relation for the $A_{\mathrm{j}\to\mathrm{i}}$ spontaneous emission coefficient [68]

$$A_{\mathrm{j}\to\mathrm{i}} = \frac{\hbar\omega_{\mathrm{j}\to\mathrm{i}}^3}{\pi^2 c^3} B_{\mathrm{j}\to\mathrm{i}}. \tag{2.21}$$

Consequently, the spontaneous emission rate from an excited state i toward a lower lying state j with an emission photon angular frequency ω and polarization q can be written as

$$\Gamma_{\mathrm{i}\to\mathrm{j}}^{\mathrm{sp}} = \frac{\omega^3 e^2 a_0^2}{3\pi\varepsilon_0 \hbar c^3} |\langle \mathrm{j}| r^{(q=m'-m)}/a_0 |\mathrm{i}\rangle|^2. \tag{2.22}$$

The considerations above incorporate the electric dipole approximation which states that the photon wavelengths involved in the treated quantum state transitions are large compared to atomic scales. Thus, the light electric field does not resolve the exact matter distribution within the atom and the assumption that photons are absorbed or emitted from the nucleus' (instead of the electron's) position is justified. This is indeed closely linked to Fermi's Golden Rule which is the approximation that, for long enough times, only the electric field modes at resonance with the atomic spectrum contribute to the described processes. An instructive study of Fermi's Golden Rule and its limits within the hydrogen atom is provided in [75]. As demonstrated, a perturbation theory approach leads, in first-order approximation, to a constant transition probability per unit of time. The indicated spontaneous emission rates will be extensively used throughout the work presented in this thesis.

2.2.2 Stimulated transition rates

For a laser with spectral irradiance $I(\omega)$ (in the following called laser intensity) and the considered transition's Lorentzian spontaneous emission spectrum $L(\omega) =$

$\frac{1}{\pi}\frac{\Gamma/2}{(\omega-\omega_{\mathrm{i}\to\mathrm{j}})^2+(\Gamma/2)^2}$, the stimulated transition rate from level i to j is expressed by

$$\Gamma^{\mathrm{stim}}_{\mathrm{i}\to\mathrm{j}} = \frac{\int L(\omega)I(\omega)\mathrm{d}\omega\pi|\boldsymbol{d}_{\mathrm{i}\to\mathrm{j}}.\boldsymbol{\epsilon}|^2}{\hbar^2\epsilon_0 c}. \tag{2.23}$$

The transition dipole is given by $d_{\mathrm{i}\to\mathrm{j}} = ea_0\langle\mathrm{j}|r^{(q=m-m')}/a_0|\mathrm{i}\rangle$ and $\boldsymbol{\epsilon}$ denotes the light polarization vector. The emission or absorption photon angular frequency is given by $\omega_{\mathrm{i}\to\mathrm{j}}$.

Considering a light source with FWHM Γ_{L} and a Lorentzian spectrum leads to $I(\omega) = \frac{I}{\pi}\frac{\Gamma_{\mathrm{L}}/2}{(\omega-\omega_0)^2+(\Gamma_{\mathrm{L}}/2)^2}$. The full laser irradiance is given by $I = \int I\,(\omega)\,\mathrm{d}\omega$ and the laser electric field is $E = \sqrt{2I/\epsilon_0 c}$. Now,

$$\Gamma^{\mathrm{stim}}_{\mathrm{i}\to\mathrm{j}} = \frac{\Omega^2/2}{(\omega_0-\omega_{\mathrm{i}\to\mathrm{j}})^2+((\Gamma_{\mathrm{L}}+\Gamma)/2)^2}\frac{\Gamma_{\mathrm{L}}+\Gamma}{2}, \tag{2.24}$$

where $\Omega = \mathbf{d}_{\mathrm{i}\to\mathrm{j}}.\mathbf{E}/\hbar$ is the Rabi frequency. For a broadband light source, where $\Gamma_{\mathrm{L}} \gg \Gamma$, the final rate at resonance is found to be [76]

$$\Gamma^{\mathrm{stim}}_{\mathrm{i}\to\mathrm{j}} = \frac{\Omega^2}{\Gamma_{\mathrm{L}}} = \frac{2I|d_{\mathrm{i}\to\mathrm{j}}\epsilon_q|^2}{\hbar^2\epsilon_0 c\Gamma_{\mathrm{L}}}. \tag{2.25}$$

2.2.3 Photoionization rates

To evaluate the effect of photoionization, the corresponding photoionization cross sections are calculated, for a given n-manifold, using the extra photon energy $E = \kappa^2 Ry = \hbar\omega - Ry/n^2$ above the ionization threshold, where Ry is the Rydberg energy. The use of field-free wavefunctions for the continuum can be justified by the fact that, for fields around 1 T, the thermal spread $\sim k_B T$ is larger than the energy of the cyclotron frequency $\hbar eB/m$. Thus, this tends to smear out the Landau quantization of the cyclotron frequency in the continuum (the bottleneck arises at a temperature below 1.3 $\mathrm{K\,T^{-1}}$) [35]. Furthermore, assuming unpolarized light, an averaged cross-section can be defined by

$$\sigma^{\kappa}_{n,m} = \sum_{l=|m|}^{n-1}\frac{\sigma^{\kappa,l+1}_{n,l}+\sigma^{\kappa,l-1}_{n,l}}{2l+1} \tag{2.26}$$

from each (n, m) level toward the continuum. This is similar to the assumption of a full k (or l) mixing (as done in the section 3.4 and the therein referenced Fig. 11 in [1]).

The cross sections $\sigma_{n,l}^{\kappa,l'}$ are calculated using $R_{nl}^{\kappa l'} = \int_0^\infty R_{nl}(\rho)\rho R_{\kappa l'}(\rho)\rho^2 d\rho$ which leads to [2, 3]

$$\begin{aligned}\sigma_{n,l}^{\kappa,l+1} &= \frac{4}{3}\pi^2\alpha a_0^2 \frac{l+1}{2l+1}\frac{1+n^2\kappa^2}{n^2}R_{nl}^{\kappa l+1}\\ \sigma_{n,l}^{\kappa,l-1} &= \frac{4}{3}\pi^2\alpha a_0^2 \frac{l}{2l+1}\frac{1+n^2\kappa^2}{n^2}R_{nl}^{\kappa l-1},\end{aligned} \tag{2.27}$$

where $R_{nl}^{\kappa l'}$ is given, for $l' = l+1$ and $l' = l-1$, by

$$R_{nl}^{\kappa l+1} = \frac{-i}{4\kappa(2l+1)!}\sqrt{\frac{1}{2}\frac{(n+l)!\prod_{s=1}^{l+1}(1+s^2\kappa^2)}{(n-l-1)!(1-e^{-\frac{2\pi}{\kappa}})}}\left(\frac{4n}{1+n^2\kappa^2}\right)^{l+2}\times$$
$$\times e^{-\frac{2}{\kappa}\arctan(n\kappa)}\left(\frac{n-i/\kappa}{n+i/\kappa}\right)^{n-l-2}\times$$
$$\times\left({}_2F_1\left(l+2-i/\kappa, l+1-n; 2l+2; -\frac{4n\,i/\kappa}{(n-i/\kappa)^2}\right) - \left(\frac{n-i/\kappa}{n+i/\kappa}\right)^2\times\right.$$
$$\left.\times\,{}_2F_1\left(l-i/\kappa, l+1-n; 2l+2; -\frac{4ni/\kappa}{(n-i/\kappa)^2}\right)\right)$$

$$R_{nl}^{\kappa l-1} = \frac{-1}{4(2l+1)!}\sqrt{\frac{1}{2}\frac{(n+l)!\prod_{s=1}^{l-1}(1+s^2\kappa^2)}{(n-l-1)!(1-e^{-\frac{2\pi}{\kappa}})}}\left(\frac{4n}{1+n^2\kappa^2}\right)^{l+1}\times$$
$$\times e^{-\frac{2}{\kappa}\arctan(n\kappa)}\left(\frac{n-i/\kappa}{n+i/\kappa}\right)^{n-l-1}\times$$
$$\times\left({}_2F_1\left(l-i/\kappa, l+1-n; 2l; -\frac{4n\,i/\kappa}{(n-i/\kappa)^2}\right) - \left(\frac{n-i/\kappa}{n+i/\kappa}\right)^2\times\right.$$
$$\left.\times\,{}_2F_1\left(l-i/\kappa, l-1-n; 2l; -\frac{4ni/\kappa}{(n-i/\kappa)^2}\right)\right). \tag{2.28}$$

3 Simulation of antihydrogen deexcitation and formation mechanisms

Building upon the theory outlined in chapter 2, simulation results are laid down in the following. In section 3.1, the discussion of a generic model outlines a variety of key points relevant in the context of the deexcitation of a large number of levels toward ground state. The efficiency of a pulsed deexcitation method (applicable to CE) making use of a visible laser and state mixing through an electric field that is added to the magnetic field already present in the $\overline{\mathrm{H}}$ formation region is assessed in section 3.2. Continuous deexcitation methods in pure B fields are treated in section 3.3. Here, the Rydberg states are mixed making use of THz and microwave radiation. The combination of the continuous deexcitation methods with a stimulated radiative recombination laser is studied in section 3.4.

3.1 Generic deexcitation model

$\overline{\mathrm{H}}$ atoms are formed at CERN in a large number of highly excited Rydberg states (cf. chapter 1). The decay of this population toward ground state can be accelerated by coupling the initially populated levels to states that rapidly decay via spontaneous emission toward the ground state. When addressing a large number of long lived states (between $n = 20$ and $n = 30$ there are $\sim$7000 levels), it is important to transfer the population toward the short lived target states at rates that are faster than spontaneous decay. Additionally, it is crucial to establish equal rates between individual levels since comparatively slow transition rates will always

constitute a bottleneck, potentially trap parts of the addressed population and consequently slow down the deexcitation process. In the following, the objective will always be to achieve an equipopulated state distribution as fast as possible that can then be depopulated through the targeted short lived states toward ground state.

To grasp the mechanisms at play and to point out some inherent limitations of such a deexcitation process, a generic model can be an instructive first approach (cf. [1]). Assuming an initial distribution of N Rydberg states that have lifetimes τ_N of the order of ms and are coupled to a number of target levels N' that exhibit an average deexcitation time to ground state of $t_{N'}^{\mathrm{GS}} \ll \tau_N$ leads to a total deexcitation time t_{deex} of

$$t_{\mathrm{deex}} = \frac{N}{N'} \times t_{N'}^{\mathrm{GS}}. \tag{3.1}$$

Even though spontaneous emission from the initially populated Rydberg levels is neglected, Eq. 3.1 gives helpful insights into the timescales involved in the deexcitation process. For the sake of simplicity, the decay time of the target levels toward ground state $t_{N'}^{\mathrm{GS}}$ will here be approximated by the average lifetime $\tau_{n'}$ of the target manifold n', which is, in particular for fast decaying low n', a valid approximation. Still, the determination of such an average lifetime is not straight forward. Summing the exponential decay of all n' sublevels leads to different behaviors at short and long time scales. The overall decay is thus slightly non-exponential and will here be approximated under two different assumptions departing, in both cases, from Eq. 1.1.

- Averaging the decay times as done in [1] results in

$$\tau_{n'} = \frac{1}{n'^2} \sum_{l'=0}^{n'-1} (2l'+1)\, \tau_{\mathrm{n',l'}} \approx 5\,\mu\mathrm{s} \times (n'/10)^5. \tag{3.2}$$

  Here the lifetime is slightly over-estimated due to the dominance of long lived circular states.

- Under the assumption of fully mixed sublevels the decay rates can be averaged leading to a scaling of [2]

$$\tau_{n'} \approx 2\,\mu\mathrm{s} \times (n'/10)^{4.5}. \tag{3.3}$$

In the range of n values investigated in this thesis and in particular for low lying n' manifolds that are of interest in this section, both approaches yield similar results. Both scaling laws are in good agreement with the analytical solution found by Chang et al. [21] suggesting a $\tau_{n'} \propto n^5/\ln n$ scaling law.

In summary, approximating $t_{N'}^{\mathrm{GS}}$ by $\tau_{n'}$ and coupling, for example, $\sim$7000 levels ($n = 20$ to $n = 30$) to the $n' = 3$ manifold that lives on average 10 ns, results in a deexcitation time t_{deex} of $\sim$8 µs. This is well in line with the timescales available to bring antihydrogen to ground state in typical experimental conditions.

3.2 Pulsed deexcitation via E and B field mixing

The main idea in this section is to mix the Rydberg states initially populated after the $\overline{\mathrm{H}}$ formation via CE with an electric field that is added to the magnetic one already present in the atoms' formation region. The long lived mixed initial population can then be coupled to a deexcitation laser that drives the population to a low lying, fast decaying n' manifold. Such a scheme has been proposed by Comparat and Malbrunot in [2, 3] and is illustrated in Fig. 3.1.

Under the assumption of fully mixed states (i.e. in other words one assumes that the additional $\boldsymbol{E}$ field couples all Rydberg states equally strongly to the n' manifold), the system can be reduced to a simple set of rate equations by defining average $n \rightarrow n'$ transition dipoles $d_{n\rightarrow n'} = \frac{1}{n^2+n'^2}\sum_{m_1,m_2,l,m} d_{n,m_1,m_2\rightarrow n'l'm'}$, where m_1 and m_2 denote the quantum numbers of the Rydberg state that is perturbed by the $\boldsymbol{E}\times\boldsymbol{B}$ field. The low lying target manifold n' can be assumed to be flat and consequently the field-free quantum numbers l' and m' can be used in approximation (cf. subsection 2.1.1). As a result, the complex system of ten thousands of states reduces to a very efficient set of three rate equations. For an initial Rydberg state population N_1 with a level degeneracy of n_1 (that is simply the number of mixed states that are addressed by the deexcitation laser), a population N_2 of the low lying n' target manifold with a degeneracy $n_2 = n'^2$ and the ground

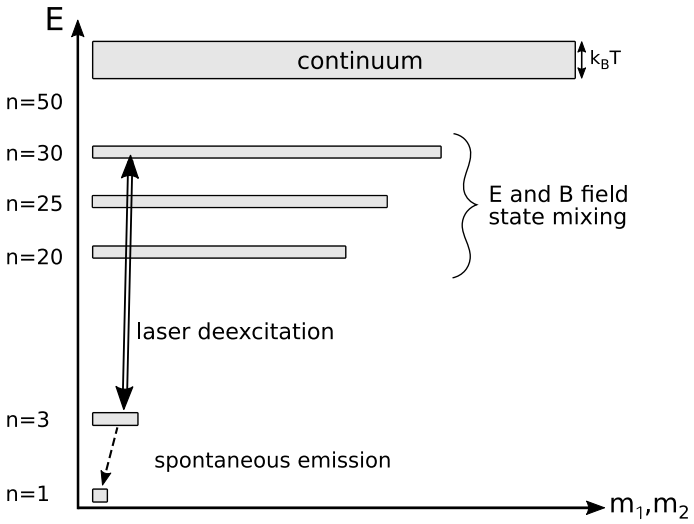

Figure 3.1: Illustration of the pulsed deexcitation mechanism.

state population N_3, the rate equations are [2, 3]

$$\begin{aligned} n_1 \frac{\mathrm{d}N_1}{\mathrm{d}t} &= -n_2 \Gamma_{\mathrm{stim}}(N_1 - N_2) - n_1 \Gamma_{\mathrm{pi}} N_1 \\ n_2 \frac{\mathrm{d}N_2}{\mathrm{d}t} &= n_1 \Gamma_{\mathrm{stim}}(N_1 - N_2) - n_2 \Gamma_{\mathrm{spon}} N_2 \\ \frac{\mathrm{d}N_3}{\mathrm{d}t} &= n_2 \Gamma_{\mathrm{spon}} N_2 . \end{aligned} \tag{3.4}$$

The averaged photoionization rate from the Rydberg states toward the continuum is written as Γ_{pi}, the average laser stimulated rate as Γ_{stim} and the average spontaneous emission rate from the n' manifold toward ground state as Γ_{spon}. It is noteworthy to mention the relation of such rate equations to the discussion of the general deexcitation principles with a generic model above in section 3.1. The included degeneracy parameters take into account the considerations therein.

As pointed out in section 1.2, $n = 30$ is a typical initially targeted manifold when producing $\overline{\mathrm{H}}$ atoms via CE. Thus, a key interest of this work is to assess the

efficiency of the deexcitation targeting these atomic levels. The ratio $\Gamma_{\mathrm{stim}}/\Gamma_{\mathrm{pi}}$ was calculated, for $n = 30$, to be 26.3 ($n' = 3$) and 84.6 ($n' = 2$) (cf. Table 1 in [2, 3]). For lower lying addressed n states this ratio is even higher. Thus, in the rest of this section the coupling of the Rydberg population to the continuum will be neglected. The rate equations (Eq. 3.4) can be used to evaluate different electric field strengths and respective orientations to the magnetic field. Indeed, this simplified system can easily be parameterized (e.g. as a function of the field strengths and angles) and solved numerically. The optimal field configuration to mix the $n = 30$ manifold has been identified, for $n = 30$, to be 280 V cm^{-1} at a crossing angle of 160° with respect to the 1 T magnetic field (cf. Fig. 3 in [2, 3]). These field values will be used for the simulations and results presented in the following.

3.2.1 Transition bandwidths, excitation and ionization

The energy levels in the given crossed $\boldsymbol{E}$ and $\boldsymbol{B}$ field configuration have been calculated using perturbation theory in section 2.1.1. In particular, Fig. 2.3 shows the energy shift of all (m_1, m_2) sublevels for given n manifolds. From this plot the laser bandwidths required for the deexcitation can be derived by evaluating the frequency spread given by the sublevels' maximum and minimum energy. Coupling all sublevels of the $n = 30$ ($n = 25$ and $n = 20$) manifold to a low lying n' one (that will assumed to be "flat" – the frequency spread of the $n' = 3$ manifold is 56 GHz) requires a laser bandwidth of 34.2 cm^{-1} (25.5 cm^{-1} and 18.8 cm^{-1}) corresponding to 1024 GHz (764 GHz and 565 GHz).

In addition to the laser spectral bandwidths, the effect of undesired excitation to higher n manifolds can be discussed making use of Fig. 2.3. The plot shows that for $n \sim 25$ and higher, the binding energies of the sublevels increasingly overlap. Consequently, coupling initially populated Rydberg states of a given n manifold with a laser to low lying n' levels can result in a re-excitation of parts of the population to levels in the vicinity of the initially targeted n Rydberg states. This leads to excitation processes. Such an undesired effect becomes increasingly significant when addressing high n states because the inter-n-manifold energy spacing rapidly decreases and the number of states the population is coupled to increases with n^2 and thus slows down the deexcitation process (cf. generic model, section 3.1). From Fig. 2.3 one can extract that addressing all (m_1, m_2) sublevels

of the $n = 30$ manifold with a laser couples the population to states up to $n \sim 35$. For $n = 25$ the coupling to higher lying n levels is already limited to $n = 26$ only and for $n = 20$ the effect can be safely neglected.

3.2.2 Pulsed laser stimulated deexcitation

Reducing the atomic processes to a fully mixed three level system has proven very helpful to efficiently identify the optimal mixing field configuration. However, the approximations made are quite rough and in reality the coupling of each individual (n, m_1, m_2) level to the n' manifold is different. This becomes particularly important when the population is optically pumped from the target n' manifold back to the addressed Rydberg states. In order to fully account for all of these complex processes, the efficiency of the proposed methods in populating the ground state is investigated by solving the complete set of rate equations.

The rate equations can be written as $\frac{\mathrm{d}\mathbf{P}}{\mathrm{d}t} = \mathbf{MP}$. The matrix system is solved taking into account all (m_1, m_2) sublevels with $1 \leq n \leq 35$. The vector $\mathbf{P}$ is of length $N = \sum_{\tilde{n}=1}^{n=35} \tilde{n}^2 = 14910$ and its elements N_i represent the population of each given state. The matrix elements $M_{\mathrm{i,j}}$ ($\dim(\mathbf{M}) = 14910 \times 14910$) are calculated as the sum of stimulated and spontaneous rates between all individual levels i and j:

$$\mathbf{M} = \begin{array}{c|c|c|c|c} & \mathrm{j}=1 & \cdots & \cdots & \mathrm{j}=N \\ \mathrm{i}=1 & -\sum_{\mathrm{j}^*=1}^{N}\Gamma^{\mathrm{sp}}_{\mathrm{i}\to\mathrm{j}^*} - \sum_{\mathrm{j}^*=1}^{N}\Gamma^{\mathrm{stim}}_{\mathrm{i}\to\mathrm{j}^*} & \Gamma^{\mathrm{sp}}_{\mathrm{i}\to\mathrm{j}} + \Gamma^{\mathrm{stim}}_{\mathrm{i}\to\mathrm{j}} & \cdots & \Gamma^{\mathrm{sp}}_{\mathrm{i}\to\mathrm{j}} + \Gamma^{\mathrm{stim}}_{\mathrm{i}\to\mathrm{j}} \\ \vdots & \Gamma^{\mathrm{sp}}_{\mathrm{i}\to\mathrm{j}} + \Gamma^{\mathrm{stim}}_{\mathrm{i}\to\mathrm{j}} & \ddots & \ddots & \vdots \\ \vdots & \vdots & \ddots & \ddots & \Gamma^{\mathrm{sp}}_{\mathrm{i}\to\mathrm{j}} + \Gamma^{\mathrm{stim}}_{\mathrm{i}\to\mathrm{j}} \\ \mathrm{i}=N & \Gamma^{\mathrm{sp}}_{\mathrm{i}\to\mathrm{j}} + \Gamma^{\mathrm{stim}}_{\mathrm{i}\to\mathrm{j}} & \cdots & \Gamma^{\mathrm{sp}}_{\mathrm{i}\to\mathrm{j}} + \Gamma^{\mathrm{stim}}_{\mathrm{i}\to\mathrm{j}} & -\sum_{\mathrm{j}^*=1}^{N}\Gamma^{\mathrm{sp}}_{\mathrm{i}\to\mathrm{j}^*} - \sum_{\mathrm{j}^*=1}^{N}\Gamma^{\mathrm{stim}}_{\mathrm{i}\to\mathrm{j}^*} \end{array}.$$

The laser stimulated rates from a level i to j are denoted $\Gamma^{\mathrm{stim}}_{\mathrm{i}\to\mathrm{j}}$. Spontaneous rates $\Gamma^{\mathrm{sp}}_{\mathrm{i}\to\mathrm{j}}$ are set to zero for $n > n'$. This can be justified pointing out the average lifetime of the Rydberg states that is on the few millisecond timescale whereas the deexcitation process takes place three orders of magnitude faster (within a few microseconds).

Fig. 3.2 shows the simulated ground state fraction for different initially populated n manifolds and laser polarizations driving $n \rightarrow n'$ transitions. The low lying target manifold that is quickly depopulated via spontaneous emission is $n' = 3$. As mentioned, the employed field configuration (280 V cm^{-1}, 1 T, 160°) is optimized for mixing the $n = 30$ manifold [2]. This results in a maximum achievable, close to unity, ground state fraction which is highest for an initial population in the $n = 30$ manifold (first line). In order to assess the efficiency of the $\boldsymbol{E} \times \boldsymbol{B}$ mixing in the vicinity of $n = 30$, the scheme is also simulated for an initial population (and a $n \rightarrow n'$ laser) in $n = 25$ and $n = 20$. One finds that the substates in $n = 25$ (second line) can still be considered well mixed whereas the ground state fraction achievable for an initially populated $n = 20$ manifold (third line) is significantly decreased to roughly ~ 60 % due to sub-optimal mixing. The addressed fraction of the population is in all cases deexcited to ground state within a few microseconds. For $n = 30$ the population of the ground state flattens out shortly after 10 µs whereas for $n = 20$ the scheme is slightly more than twice as fast. This can primarily be explained by the number of states addressed. The level degeneracy increases with n^2 (in fact the scaling is even more extreme due to excitation to higher levels which becomes increasingly significant for high n) which results in a faster population of the ground state for lower lying addressed n manifolds. This observation is in good agreement with the generic model introduced in section 3.1 which yielded timescales of ~ 8 µs when addressing all levels with $20 \leq n \leq 30$. The laser intensity required to saturate the $n \rightarrow n'$ transitions decreases for lower n values because the radial overlap of the atomic orbits increases which leads to elevated transition dipoles. Additionally, the necessary spectral laser bandwidth is reduced because the energy shift of the addressed atomic levels decreases with n. Compared to the intensity required to drive the $n = 30 \rightarrow n' = 3$ transition, the saturation limit is reached, for $n = 25$ ($n = 20$), a factor 2 (20) earlier. Finally, the evaluation of different laser polarizations clearly shows that, as expected, for isotropic light (left column) the ground state populates most efficiently meaning that the saturation limit (i.e. a steady state population of all levels) is reached faster. The achievable ground state fraction for $\sigma^{\pm}$ polarized light is smaller. The result for $\sigma^{\pm}$ is only marginally better compared to simulations for π polarization (plots not shown) which holds true for all initial $\overline{\mathrm{H}}$ populations considered.

Earlier considerations showed that the lifetime of a fully mixed manifold scales as $\tau \propto n^{4.5}$ (cf. Eq. 3.3) whereas the number of states within the target manifold scales as n^2. Thus, recalling the generic model (cf. section 3.1), the benefit from the

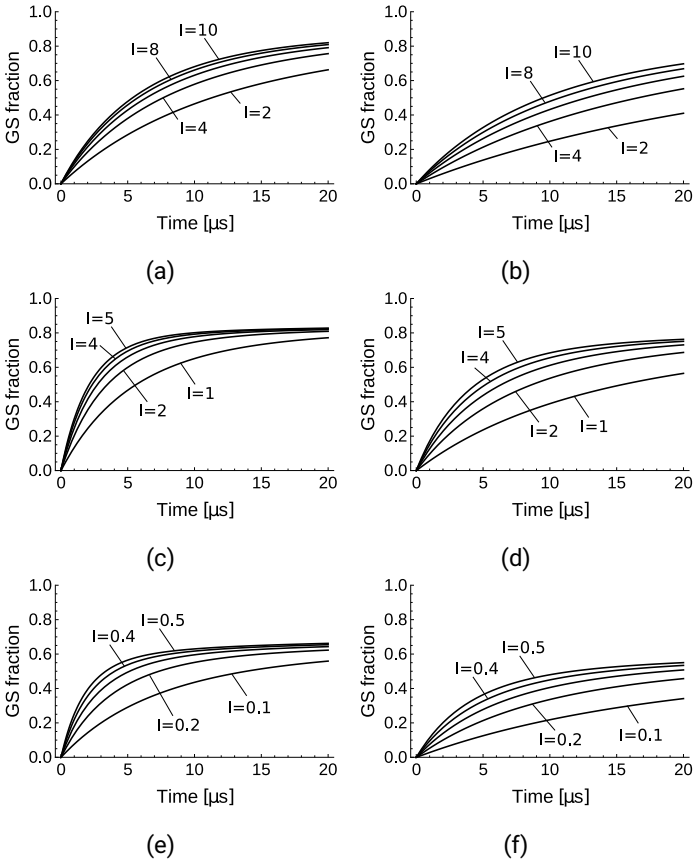

Figure 3.2: Ground state fraction over time for laser ($n \to n' = 3$ manifold) stimulated deexcitation. The laser intensities are given in units of GW m^{-2}. A statistical population is initiated in the $n = 30$ (first line), $n = 25$ (second line) or $n = 20$ (third line) manifold. The first column shows the results for an isotropic laser whereas the second one refers to circular ($\sigma^{\pm}$) polarized laser light. The laser bandwidths are (cf. section 2.3) 1024 GHz (first line), 764 GHz (second line) and 565 GHz (third line).

shorter lifetime of lower lying n' levels is higher than the drawback of addressing less substates. Consequently, one can expect a faster ground state population when stimulating transitions from n toward $n' = 2$ instead of $n' = 3$. This is confirmed by the simulation results presented in Fig. 3.3. The plots show, similar to Fig. 3.2, but for $n' = 2$, the ground state fraction as a function of time for different initially populated manifolds, light polarizations and intensities. The key conclusions drawn from Fig. 3.2 are, as expected, still valid for the $n = 2$ case. For isotropic light and $n = 30$ the ground state fraction after 5 µs can be improved to the prior result considering $n' = 3$ from $\sim 47\,\%$ to $\sim 64\,\%$. For $n = 25$ the GS fraction improves, again for isotropic light, after 2 µs from $\sim 40\,\%$ to $\sim 60\,\%$. This acceleration of the decay is however at the expense of an increased necessary laser intensity. Due to the decreased transition dipole compared to the $n' = 3$ case, the laser intensities increase by a factor 10. It is noteworthy to mention that the maximum achievable GS fraction for each configuration stays the same.

The laser intensities required to drive transitions toward $n' = 3$ are of the order of $10\,\mathrm{GW\,m^{-2}}$ for $n = 30$ and $n = 25$. For $n = 20$ some $1\,\mathrm{GW\,m^{-2}}$ seem sufficient. Assuming beam diameters of the order of mm^2, this corresponds to a pulse energy of $\sim 100\,\mathrm{mJ}$ for a pulse duration of $\sim 10\,\mu\mathrm{s}$. The wavelengths required are 828 nm, 832 nm and 839 nm. Some comments on the technical feasibility of such lasers can be found in subsection 4.1.3. The close to UV (368 nm) light required to stimulated, for example, the $n = 30 \to n' = 2$ transitions is somewhat hypothetical since laser intensities are, compared to $n' = 3$, further increased and powerful, broadband light at these wavelengths and pulse duration is notoriously hard to generate[1].

3.3 Continuous deexcitation via THz and/or microwave mixing

In contrast to CE formation, where additional E fields can be employed between the $\overline{\mathrm{H}}$ production pulses, in experiments relying on continuous 3BR additional electric fields would disturb the antiproton-positron plasma hindering the $\overline{\mathrm{H}}$ production.

[1] A narrowband laser for the opposite purpose, excitation from the 2s to the 30p Rydberg levels, is discussed in subsection 4.5.2.

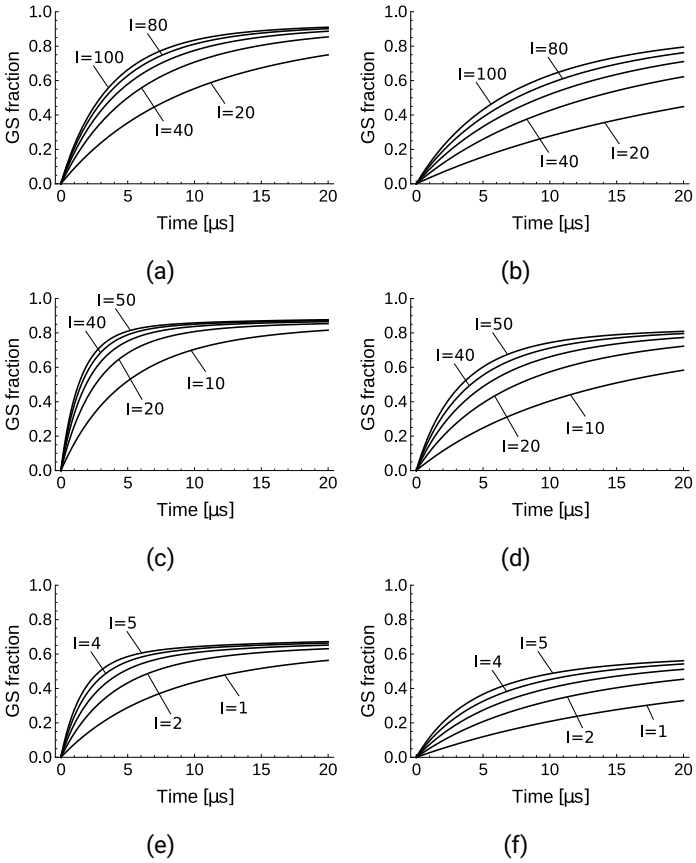

Figure 3.3: Ground state fraction over time for laser stimulated deexcitation. The population is initiated in the $n = 30$ (first line), $n = 25$ (second line) or $n = 20$ (third line) levels. A laser stimulates the transitions from n down to the $n' = 2$ manifold. The first column shows results for an isotropic laser. The second column refers to circular ($\sigma^{\pm}$) polarized laser light. Laser intensities are given in units of GW m^{-2}. The corresponding laser bandwidths are (cf. section 2.3) 1024 GHz (first line), 764 GHz (second line) and 565 GHz (third line).

Thus, this section investigates $\overline{\mathrm{H}}$ deexcitation relying on state mixing via THz and/or microwave light. For this purpose, energy levels and transition dipoles have been calculated performing a full diagonalization of the Hamiltonian in the presence of a pure magnetic field as described in subsection 2.1.2. As pointed out earlier, one should note that in realistic experimental conditions an additional electric field is present to hold the charged particles in place. This small additional field which is typically of the order of $10\,\mathrm{V\,cm^{-1}}$ can lead to a perturbation of the states [58, 77, 78]. A study of the combined magnetic and electric field effects via full diagonalization is outside the scope of this work – in mixed $\boldsymbol{E}$ and $\boldsymbol{B}$ fields m is not a good quantum number anymore and consequently the Hamiltonian can not be diagonalized sequentially for all sets of (n, m) states which implies a drastically increased computing effort. In general, this small electric field will create an additional mixing (cf. perturbation theory approach for crossed $\boldsymbol{E}$ and $\boldsymbol{B}$ fields in subsection 2.1.1) which is favorable in view of the deexcitation goal. However, the electric field might also induce potential losses through new excitation channels. In this section the simulations are performed assuming that the formed atoms have escaped the antiproton-positron formation plasma and are therefore not subject to charged particle collisions. In contrast, the direct formation of ground state atoms within the formation plasma via stimulated radiative recombination is studied taking into account state mixing through collisional processes in section 3.4. The mixing schemes and deexcitation or formation mechanisms investigated are summarized in Fig. 3.4.

3.3.1 Transition bandwidths, excitation and ionization

The theory developed in subsection 2.1.2 allows to calculate all (n, k, m) energy levels in a pure $\boldsymbol{B}$ field to deduce intra- and inter-n-manifold transition frequencies and bandwidths that are required for the simulations presented below.

Fig. 3.5a shows inter-n-manifold transition frequencies and bandwidths. For linear light polarization the $\Delta n = -1$ transitions range from over 7.5 THz for the $n = 10 \rightarrow 9$ transition to 0.26 THz for $n = 30 \rightarrow 29$. The frequencies for circular polarized light are detuned from these values by roughly $\pm\,14$ GHz, the linear Zeeman shift in a 1 T magnetic field. Due to the scaling of the axis, this shift is however not visible. The energy broadening of the manifolds' substates leads to $\Delta n = -1$ transition bandwidths ranging from 0.5 GHz for $n = 10$ to 53.1 GHz

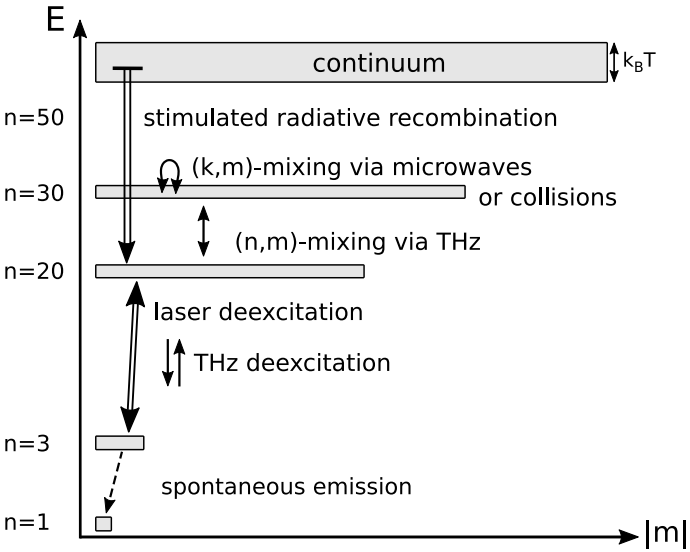

Figure 3.4: Illustrative summary of the continuous mixing and deexcitation or formation processes investigated. Reprinted from [1].

for $n = 30$. In a 1 T field this spectral width needs to be covered in order to address all k substates when stimulating transitions for a given light polarization. The plot in Fig. 3.5b shows the spectral spread of the intra-n-manifold $\Delta n = 0$ transitions. For $\Delta m = 0$ transitions (i.e. for π polarized light) the bandwidth is determined solely by the diamagnetic Zeeman effect of the (k, m) substates that interact strongest with the B field. Referring back to Fig. 2.5, this corresponds to the frequency spread of the $m = 0$ states that amounts, for $n = 20$, to 5.6 GHz. For $\sigma^{\pm}$ polarized light the $\Delta m = \pm 1$ paramagnetic shift of $\mu B = 14\,\mathrm{GHz}$ is added up to the linearly polarized case. This effect is visible for n manifolds above $n \sim 25$. For stronger bound levels the diamagnetic shift has not exceeded the 14 GHz yet and thus the bandwidths for linear and circular polarization lie closer to each other. The numerical values range from 0.31 GHz (0.62 GHz) for $n = 10$ to 28.4 GHz (42.4 GHz) for $n = 30$.

The inter-n-manifold energy spacing rapidly decreases for highly excited states. Thus, the light sent toward the atomic sample to stimulate $\Delta n = \pm 1$ transitions in highly excited Rydberg states has the potential to spread the population out to $n^* \gg n$ states which can culminate in ionization. Such excitation and ionization processes consequently set a limit to the wavelengths that can be employed as well as to the range of n-states that can be efficiently targeted. Fig. 3.5c illustrates the maximum and minimum $\Delta n = -1$ transition frequency as a function of n. For states with $n \sim 25$ and higher, the band of frequencies that needs to be addressed increasingly overlaps with the wavelengths of neighboring $n \to n \pm 1$ transitions. The light necessary to stimulate all $n = 30 \to 29$ transitions (~ 0.26 THz with ~ 50 GHz spectral linewidth) can excite[2] the population step wise (i.e. from $n = 30 \to 31 \to 32 \cdots$) up to $n = 35$. The same applies to the light sent toward $n = 29 \to 28$ transitions, but the effect rapidly decreases due to the $1/n^3$ inter-manifold spacing and the decrease in the bandwidth required to drive the $\Delta n = -1$ transitions (that scales as n^4). As a consequence, the $n = 30$ manifold lies close to an optimum value where the number of states addressed is maximized and, at the same time, excitation is kept at a reasonable level and, most importantly, does not culminate in a coupling of the population to the continuum. It is important to note the difference and increased complexity of excitation processes compared to the

[2]In a side note, the in principle undesired excitation effect can also be put differently: the frequencies sent toward the $n = 30 \to 29$ transitions also couple the mixed population to antihydrogen atoms that initially populate states with $30 < n \leq 35$. The total number of atoms deexcited is thus increased "for free".

pulsed laser deexcitation (cf. section 3.2) where no such culminating effects are possible. The simulations laid down in the following take into account excitation up to the $n = 35$ levels. It was found that such excitation mainly (and almost exclusively) slows down the deexcitation process since the scheme simply involves more levels (cf. section 3.1) – the maximum achievable ground state fraction remains unchanged.

Single-photon photoionization of high lying n manifolds can occur when stimulating $\Delta n = -1$ transitions toward low lying n' levels. The zero field ionization threshold for the $n = 30$ manifold lies around 3.7 THz which roughly corresponds to the transition frequencies from $n = 13 \to 12$. For $n = 40$, the frequency amounts to 2.1 THz (corresponding roughly to $n = 15 \to 14$) and for $n = 50$ to 1.3 THz (corresponding roughly to $n = 20 \to 19$). The simulations presented below include photoionization rates $\Gamma^{\kappa}_{n,m} = \frac{I}{\hbar\omega}\sigma^{\kappa}_{n,m}$ for all radiation frequencies ω and intensities I sent toward the antihydrogen atoms. The ionization cross sections are calculated under the assumption of a full k-mixing. Comparable photoionization studies were done for example by Seiler et al. [79]. This group investigated the coupling of trapped hydrogen atoms to the continuum when being irradiated with a 300 K blackbody emitter. Within 100 µs roughly 15 % of an initial population in the $n = 30$ and $0 \leq |m| \leq 15$ states was ionized. This result was confirmed in [76]. In this work, total light intensities up to 500 W mm^{-2} are used which roughly corresponds to the intensity emitted in the THz frequency range by a blackbody source at 300 K. The ionization fraction was, however, found to be even smaller than in the mentioned references mainly due to the following reasons:

- The timescales investigated are on the few tens of µs timescale minimizing the interaction time of the harmful radiation with the (anti-)hydrogen atoms.
- Throughout the deexcitation process the population is rapidly driven toward low lying n manifolds that become increasingly hard to ionize.
- In contrast to Seiler et al., who initiate their population in low $|m|$ states that exhibit the highest ionization cross sections (cf. the stimulated radiative recombination cross sections in [1]), this work assumes an initial equipopulation of all substates.

Microwave radiation used to stimulate $\Delta n = 0$ transitions can as well lead to ionization. However, such a process would necessarily involve multiple photons and is consequently unlikely to lead to a significant effect. Multi-photon processes

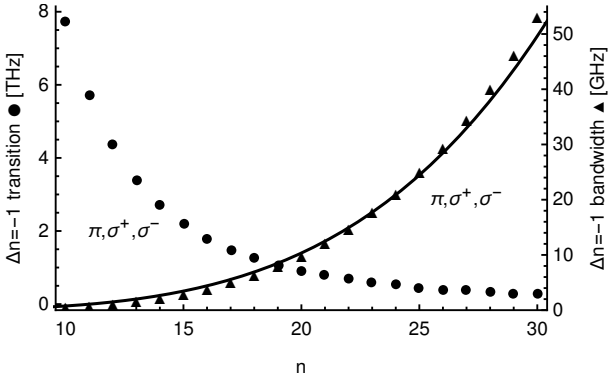

(a) Inter-manifold $\Delta n = -1$ transition frequencies and bandwidths

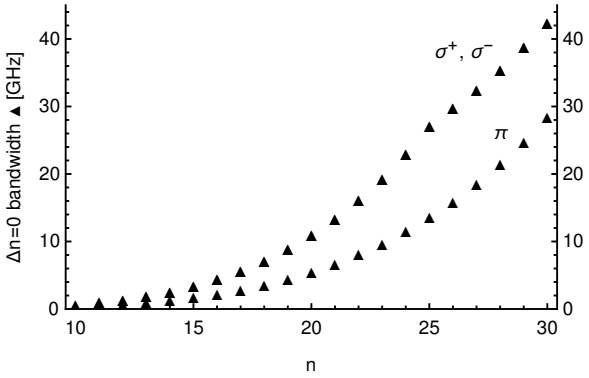

(b) Intra-manifold $\Delta n = 0$ transition bandwidths

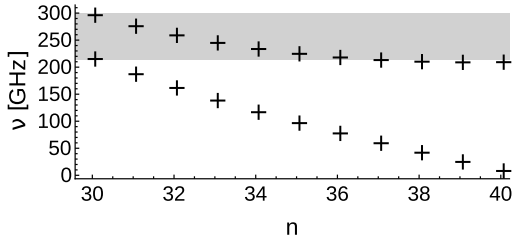

(c) Minimal and maximal $\Delta n = -1$ transition frequencies

Figure 3.5: (a) Hydrogen $\Delta n = -1$ transition frequencies as well as π, σ^+ and σ^- transition bandwidths (right axis) as a function of n in a 1 T magnetic field. The fit to the bandwidth is $\Gamma(n) = 6.5 \times 10^{-5}$ GHz $\times\, n^4$. The transition frequencies are indicated as being the central frequency of all present transitions for a given polarization. The axes' scales do not allow to distinguish the π and $\sigma^{\pm}$ curves from each other. (b) Hydrogen $\Delta n = 0$ transition bandwidths for all three polarizations. (c) Minimal and maximal transition frequencies for n to $n-1$ transitions from $n = 20$ to $n = 35$. The plot takes into account all polarizations, in a 1 T magnetic field (cf. section 2.1.2). The shaded area illustrates the bandwidth of the $n = 30$ to $n = 29$ transitions and its overlap with the bandwidth of transitions from $n > 30$. Reprinted from [1].

are quite complex to assess (involving multiple (non-)adiabatic crossings etc. [80, 81]) and are thus out of the scope of this work. Finally, a coupling to the continuum through Stark mixing [82] can be excluded for the presently treated case. Coupling a n manifold to the above-lying $n+1$ levels requires a field near the Inglis-Teller one $(n/30)^{-5} \times 7\,\mathrm{kV\,cm^{-1}}$ [1] that corresponds to microwave powers several orders of magnitude higher than what is used in the simulations presented in the upcoming section. Even though this reasoning is done in zero-field (in general a $\boldsymbol{B}$ field will mix the states and facilitate Stark coupling of consecutive manifolds), the effect will be, similarly to the multi-photon processes mentioned above, neglected.

3.3.2 Stimulated deexcitation and mixing

The efficiency of different deexcitation schemes as well as the required light intensities are extracted in a way that is similar to what has been done when assessing the effectiveness of a pulsed deexcitation reyling on $\boldsymbol{E} \times \boldsymbol{B}$ state mixing for $\overline{\mathrm{H}}$ production via CE.

The atomic processes are again simulated implementing a system of rate equations $\frac{\mathrm{d}\mathbf{P}}{\mathrm{d}t} = \mathbf{MP}$ that is solved taking into account all (k, m) sublevels with $1 \leq n \leq 35$. The population of each sublevel is again represented by $\mathbf{P}$ and the system is of size $N \times N$ with $N = \sum_{\tilde{n}=1}^{n=35} \tilde{n}^2 = 14910$. In contrast to the matrix $\boldsymbol{M}$ treating pulsed deexcitation (cf. section 3.2), where only laser driven transitions from the Rydberg states toward the n' manifold (and back) were implemented, here all rates stimulated by external THz (targeting $\Delta n = \pm 1$ transitions), microwave (targeting $\Delta n = 0$ transitions) and/or laser light (to couple a distribution of states to low lying n' levels) are calculated. If multiple radiation types are present, all possible rates are simultaneously implemented. Whereas the state mixing in the pulsed case was intrinsic to the dipoles calculated beforehand in crossed $\boldsymbol{E}$ and $\boldsymbol{B}$ fields, the coupling of Rydberg states through light interaction is now explicitly simulated relying on $\Delta n = 0, \pm 1$ (and possibly, if the frequencies sent toward the atoms match, $|\Delta n| > 1$) transition rates. Spreading the population toward low n' levels including all intermediate manifolds (it was shown that their average lifetimes scale as $n^{4.5}$) calls for the implementation of spontaneous rates from all (k, m) sublevels toward all other possible states. As pointed out in the previous

section single-photon ionization rates are included. The matrix elements $M_{\mathrm{i,j}}$ are consequently calculated as

$$\mathbf{M} = \begin{array}{c} \\ \mathrm{i}=1 \\ \vdots \\ \vdots \\ \mathrm{i}=N \end{array} \begin{array}{c} \mathrm{j}=1 \\ \left[\begin{array}{c|c|c} -\sum_{\mathrm{j}^*=1}^{N}\Gamma^{\mathrm{sp}}_{\mathrm{i}\to\mathrm{j}^*} - \sum_{\mathrm{j}^*=1}^{N}\Gamma^{\mathrm{stim}}_{\mathrm{i}\to\mathrm{j}^*} - \Gamma^{\mathrm{pi}}_{\mathrm{i}} & \cdots & \cdots \\ \hline \Gamma^{\mathrm{sp}}_{\mathrm{i}\to\mathrm{j}} + \Gamma^{\mathrm{stim}}_{\mathrm{i}\to\mathrm{j}} & \ddots & \ddots \\ \hline \vdots & \ddots & \ddots \\ \hline \Gamma^{\mathrm{sp}}_{\mathrm{i}\to\mathrm{j}} + \Gamma^{\mathrm{stim}}_{\mathrm{i}\to\mathrm{j}} & \cdots & \Gamma^{\mathrm{sp}}_{\mathrm{i}\to\mathrm{j}} + \Gamma^{\mathrm{stim}}_{\mathrm{i}\to\mathrm{j}} \end{array}\right. \\ \cdots \\ \hline \Gamma^{\mathrm{sp}}_{\mathrm{i}\to\mathrm{j}} + \Gamma^{\mathrm{stim}}_{\mathrm{i}\to\mathrm{j}} \\ \hline \vdots \\ \hline \Gamma^{\mathrm{sp}}_{\mathrm{i}\to\mathrm{j}} + \Gamma^{\mathrm{stim}}_{\mathrm{i}\to\mathrm{j}} \end{array} \begin{array}{c} \\ \mathrm{j}=N \\ \left[\begin{array}{c} \Gamma^{\mathrm{sp}}_{\mathrm{i}\to\mathrm{j}} + \Gamma^{\mathrm{stim}}_{\mathrm{i}\to\mathrm{j}} \\ \hline \vdots \\ \hline \Gamma^{\mathrm{sp}}_{\mathrm{i}\to\mathrm{j}} + \Gamma^{\mathrm{stim}}_{\mathrm{i}\to\mathrm{j}} \\ \hline -\sum_{\mathrm{j}^*=1}^{N}\Gamma^{\mathrm{sp}}_{\mathrm{i}\to\mathrm{j}^*} - \sum_{\mathrm{j}^*=1}^{N}\Gamma^{\mathrm{stim}}_{\mathrm{i}\to\mathrm{j}^*} - \Gamma^{\mathrm{pi}}_{\mathrm{i}} \end{array}\right. \end{array},$$

where $\Gamma^{\mathrm{stim}}_{\mathrm{i}\to\mathrm{j}}$ and $\Gamma^{\mathrm{sp}}_{\mathrm{i}\to\mathrm{j}}$ denote stimulated and spontaneous transitions from a level i toward a level j respectively. The coupling of the population to the continuum is implemented by depopulating each substate i with a specific rate $\Gamma^{\mathrm{pi}}_{\mathrm{i}}$.

THz stimulated deexcitation and mixing

As suggested earlier, THz light can be used to stimulate $\Delta n = -1$ transitions. Targeting initially populated $\overline{\mathrm{H}}$ states from a manifold n, multiple light sources of appropriate bandwidth can be implemented to drive all downward $\Delta n = -1$ transitions toward a n' manifold that is efficiently depopulated via spontaneous emission to the ground state. This allows to address all possible substates among which the high m ones are particularly important since they exhibit the longest lifetimes and are thus the most critical when deexciting the entire distribution of initially populated states. It is important to note here that all transitions have to be driven simultaneously (and not sequentially). The goal is to populate the n' levels with the highest possible probability that is, for a total number of N states and N' target levels, simply N'/N. Such an equipopulation of the states is different from sequentially driving $\Delta n = -1$ transitions where the population fraction of the N' levels after each cycle would be $0.5^{n-n'}$ (assuming here for simplicity, for each step, equal number of substates in the n and $n-1$ levels; the real fraction would be even smaller).

The exact initial population of states present after the $\overline{\mathrm{H}}$ formation via 3BR is experimentally not well known [5, 38, 39]. Earlier considerations showed that $n = 30$ can be considered close to the maximum manifold that can be efficiently addressed with THz light because targeting higher $\Delta n = -1$ transitions results in

excitation to manifolds $n > 35$ which increasingly slows down the deexcitation and leads to losses toward the continuum. In view of this upper limit, the population at $t = 0$ will be in the following initiated as an equipopulation of the $n = 30$ manifold. This is preferable over an equipopulation of a range of n states – which might be closer to the experimental conditions (cf. section 1.2) – to highlight the dynamics of the state mixing and deexcitation that the simulations seek to investigate. It is quite obvious that the performance of the deexcitation will increase if the experimental initial distribution of states happens to cover more n manifolds than for now assumed. In such a case the system is at $t = 0$ already in or close to a steady state equipopulation and does not have to be spread out over all $n' \leq n \leq 35$ (taking into account excitation) states in the first place.

The considered light is unpolarized ($\frac{1}{3}\sigma^+$, $\frac{1}{3}\sigma^-$ and $\frac{1}{3}\pi$) which is valid for all results provided in this section. This is a key characteristic since, for example, circular states with maximal $|m|$ can not be deexcited through linearly polarized light (cf. bottom right box in Fig. 2.4).

Fig. 3.6 shows the ground state fraction obtained for THz stimulated $\Delta n = -1$ transitions from $n = 30 \rightarrow 29$ down toward the $n' = 5$ (left column) and $n' = 10$ (right column) manifold as a function of time. The plots show, in agreement with earlier considerations, that the population of the ground-state can be accelerated when spreading the initial distribution of states out toward lower lying n' manifolds. Compared to the choice of $n' = 10$, the ground state fraction after 50 µs is increased by roughly a factor two when stimulating $\Delta n = -1$ transitions toward $n' = 5$. However, driving, in this case, five more transitions requires an order of magnitude higher total light intensity. The dynamic of the ground state population does not only depend on n' and the total THz light intensity, but also on the distribution of the overall light intensity toward each individual $\Delta n = -1$ transition. It was shown earlier that a steady state equipopulation can be achieved fastest when establishing equal rates between all involved levels. Thus, the simulations in Fig. 3.6 lay down the results for different THz intensity scalings:

- The *flat scaling* (first line) assigns equal THz intensities toward all stimulated $\Delta n = -1$ transitions. Given the argumentation below, this was thought to be the most natural choice when trying to establish equal $n \rightarrow n - 1$ rates.

Indeed, the transition rate between two n manifolds scales as

$$\Gamma \propto \frac{I d_{\mathrm{eff}}^2}{\Gamma_{\mathrm{L}}}, \tag{3.5}$$

where Γ_{L} is the spectral bandwidth of the THz source targeting the transition and d_{eff}^2 the squared effective dipole of all (k, m) sublevels of the n manifold toward all (k', m') sublevels of the $n' = n - 1$ manifold. The effective dipole can be calculated by $d_{\mathrm{eff}}^2 = \frac{1}{n^2} \sum_{k=0}^{n-1} \sum_{m=-k}^{k} d_{n,k,m \to n-1,k',m'}^2$. This average transition strength is not a unique choice, but it was found that also other definitions scale roughly as n^4.

- The *increase scaling* (second line) allocates the highest fraction of the total available THz intensity toward the $n' + 1 \to n'$ transition. The power is linearly distributed in such a way that the $n' + 1 \to n'$ transitions are stimulated with 100 times higher intensity than the $n = 30 \to 29$ transitions.
- The *decrease scaling* (third line) is the inverted *increase scaling* and allocates 100 times more power to the first $n = 30 \to 29$ transitions than to the $n' + 1 \to n'$ ones.

A comparison of the first and second line plots in Fig. 3.6 indicates that a *flat* and *increase* scaling provide sensibly the same result. The *decrease* scaling, however, is less efficient in populating the ground state. This observation is independent from the choice of n'. Consequently, the main depopulation channel toward the ground state are low n' levels. It is thus crucial to allocate sufficient power to the low $\Delta n = -1$ transitions. A sheer mixing of high n states by shining an increased fraction of the total light intensity on the high inter-n-manifold transitions and relying on short lifetimes of low m states is not sufficient to effectively deexcite. A part of an explanation for this can be the tendency of that scheme to excite the population to $n > 30$ states.

It was shown that $\sim 80\,\%$ of the initial population in the $n = 30$ states can be brought to ground state within a few tens of microseconds. The total light intensities required were found to be of the order of $200\,\mathrm{W\,m^{-2}}$. It is noteworthy to again point out that the scheme addresses, in principle, all $\overline{\mathrm{H}}$ atoms formed in states below $n \leq 35$. The total number of atoms consequently heavily depends on the initial state distribution of the atoms right after formation, which is, due to the lack of experimental data, impossible to incorporate into the simulations at

this point. In any case the scheme is very versatile and can thus be easily adapted to experimental results (that will of course depend on the exact experimental conditions varying for different experiments) once available.

The generation of 25 powerful and sharp transitions that range far into the THz region is an experimentally challenging task. A potential solution can be photomixing (further treated in subsection 4.1.2) – the generation of THz radiation from the input of two lasers. In detail, two continuous-wave polarized lasers of frequency ν_i and ν_j illuminate an ultra fast semi-conductor. Within the semi-conductor the impinging radiation creates free charge carriers with a THz beatnote at exactly the difference frequency $\nu_\mathrm{i} - \nu_\mathrm{j}$. Thanks to the short charge-carrier lifetime within the material, these free charges can be converted into a current that oscillates at the beatnote by applying an electric field. The current is converted into THz radiation by a pair of antennas. For the generation of multiple frequencies [83] the photomixer can be illuminated by a pulse-shaped single broadband laser [84–87] which is especially attractive because of the simple experimental implementation compared to multiple input lasers. Photomixers were successfully used to stimulate Rydberg population transfer in alkaline atoms at frequencies of a few tenths of THz that roughly correspond to the $n = 30 \rightarrow 29$ transition in antihydrogen [6, 76]. However, the maximum achievable output power drastically decreases toward the few THz region [88] rendering the devices unfit to stimulate $\Delta n = -1$ transitions in antihydrogen down to for example $n' = 5$. More detail on photomixing is provided in subsection 4.1.2. Simulations performed in the framework of this thesis however showed that photomixers can be, despite their low power output at high THz frequencies, an attractive solution in beam experiments where the measurement and $\overline{\mathrm{H}}$ formation region are separated by a flight path (here a length of $\sim 1\,\mathrm{m}$ and a $\overline{\mathrm{H}}$ formation temperature of $\sim 40\,\mathrm{K}$ was assumed). Simulating the effect of currently available off-the-shelf photomixers, it was found that the ground state fraction can be increased right at the formation region, compared to spontaneous decay, by roughly a factor two within a few tens of microseconds. Additionally, the initial $n = 30$ population is spread out down to manifolds $n \sim 15$. Adding up the effect of spontaneous emission on an equidistribution of states with $15 \leq n \leq 30$ along the atomic flight path amounts to a very significant gain in the ground state fraction at the measurement region.

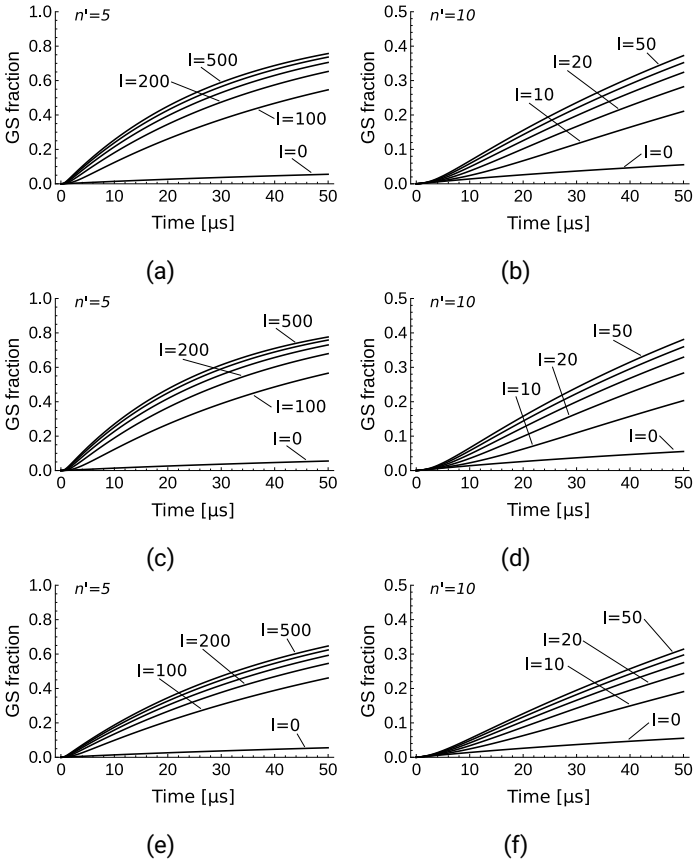

Figure 3.6: Population of the ground state as a function of time for different n' (left column: $n' = 5$, right column: $n' = 10$). The population is initiated as an equipopulation of all (k, m) substates with $n = 30$. The THz light is unpolarized and covers the para- and diamagnetic broadening of the levels (cf. Fig. 3.5a). In the first line a *flat* intensity scaling is implemented. The second and third lines show the results for a linear *increase* and *decrease* intensity scaling respectively. Total light intensities are indicated in units of W m^{-2}. Reprinted from [1].

Microwave stimulated mixing

It was shown that THz light can drive $\Delta n = -1$ transitions toward low lying n' manifolds resulting in a significant population of the ground state within a few microseconds. However, the required light intensities amount to several hundred $\mathrm{W\,m^{-2}}$. Especially in the low THz region this is hard to achieve experimentally. It is thus worth investigating, if microwave radiation can be used to decrease the required THz light intensity by stimulating $\Delta n = 0$ intra-manifold transitions. The implementation of (k, m) state mixing via microwaves would have two key advantages. Microwave sources are, compared to THz ones, easily available off-the-shelf. Further, mixing the states relying on $\Delta n = 0$ transitions and thus decreasing the THz intensity stimulating $\Delta n = -1$ transitions minimizes excitation and ionization effects.

Referring back to Fig. 2.5 it is apparent that, similar to the $n \rightarrow n - 1$ THz power scaling, an optimal microwave intensity distribution can be calculated to assure equal (or at least similar) $\Delta n = 0$ transition rates for maximum efficiency. However, for the sake of simplicity and given the fact that microwave power is readily available, here a flat microwave intensity distribution was investigated. The light is broadband (the radiation has to cover the entire spectral distribution of the addressed n-manifold) and unpolarized. The simulations point out that the stimulation of $\Delta n = 0$ transitions only marginally improves the population of the ground state (both concerning the dynamic as well as the maximum achievable ground state fraction). The sub-5 % improvement shows that the (k, m) substates are already well mixed by the THz light and that the bottleneck remains the deexcitation toward low n'. Indeed, the $\Delta n = 0$ transition dipoles $d_{n,k,m\rightarrow n,k',m'} \propto n^2$ [56] are comparatively large so that, relying solely on THz, a steady state population within the addressed manifolds is reached prior to a sufficient inter-manifold mixing to populate the ground state. This has already been suggested in the previous section when comparing the *flat* and *decrease* THz scaling.

Laser stimulated deexcitation

The results showed that THz (and potentially microwave) radiation can efficiently couple a large number of states to each other. Driving transitions toward low n' levels that rapidly decay allows to accelerate the population of the ground

state compared to spontaneous emission. However, such a scheme couples, in the presently treated case, the initial Rydberg distribution in the $n = 30$ levels to all substates with $n' \leq n \leq 35$ (taking into account excitation). This, on one hand, maximizes the number of atoms addressed, but slows down the deexcitation on the other hand because quickly a very large number of states is addressed (cf. section 3.1). From an experimental point of view, the generation of powerful light at ~ 20 frequencies that reach, for low $n \rightarrow n-1$ transitions, well into the few THz region remains a challenging task [88].

In this section the implementation of a deexcitation laser is discussed. The n' manifold can be chosen rather high when the purpose of the THz and microwave light is to mix a fraction of the initially formed $\overline{\text{H}}$ population and retain the levels equipopulated. A visible laser can then drive transitions from some n' levels down to $n'' = 3$, where states decay on the order of ten nanoseconds. Targeting the 2p state seems interesting because of the 1.6 ns lifetime, however large power from the Rydberg n' levels toward $n'' = 2$ is challenging to achieve. The 840 nm transition from $n' = 20 \rightarrow n'' = 3$ is, from an experimental point of view, preferable over the UV 368 nm $n' = 20 \rightarrow n'' = 2$ transitions.

The scheme is again simulated by solving the set of rate equations including all levels with $n \leq 35$ in a pure magnetic field of 1 T. As before, all spontaneous as well as stimulated inter- and intra-manifold rates are implemented. The population is initiated as an equipopulation in the $n = 30$ sublevels. Fig. 3.7 presents the simulation results for two different n' values (left and right column). It is important to again note that the initial state distribution of $\overline{\text{H}}$ atoms in experimental conditions is unknown and that consequently the variation of n' results in different fractions of the initially formed atoms that are addressed by the respective deexcitation scheme. Whereas the effect is negligible for the previously presented results where $n' = 5$ or $n' = 10$ (although the distribution is not well known, the fraction of atoms formed at states $5 \leq n \leq 10$ can be considered negligible), the indicated ground state fractions in Fig. 3.7 might significantly differ for the different choices of n'.

The first line investigates different deexcitation laser intensities for $n' = 20$ and $n' = 25$. In both cases, the THz intensity implemented to stimulate $n \rightarrow n - 1$ transitions is $200\,\text{W}\,\text{m}^{-2}$. This value is high enough to make sure that the repopulation of the sublevels that are coupled to the laser does not constitute a bottleneck. Consequently, the deexcitation laser saturation intensities lie around

$10 \times 10^5\,\mathrm{W\,m^{-2}}$ for $n' = 20$ and $100 \times 10^5\,\mathrm{W\,m^{-2}}$ for $n' = 25$. The simulation deals with a broadband laser (500 MHz FWHM for a Lorentzian spectrum) that couples all states in the $n'' = 3$ manifold to at least one sublevel of the mixed Rydberg distribution. This is a sufficient condition to be in optimal conditions – indeed coupling the $n'' = 3$ sublevels to multiple states in the n' manifold does neither improve the achievable ground state fraction nor the deexcitation dynamic. Since the $n' \to n''$ transitions in questions have similar dipoles, the laser intensities are indicated per 500 MHz to provide as generic plots as possible. The powers found are in the range of kW assuming a typical cm^2 spot and could be realized by cavity-enhanced or pulsed lasers. Photoionization at those wavelengths is a small effect [2, 3].

The second line in Fig. 3.7 shows the ground state fractions as a function of time for different THz intensities. Here, the laser intensities are fixed to values that are close to the saturation limit identified in Fig. 3.7a and 3.7b. The plots indicate that – as anticipated in the paragraph above – a THz intensity of $200\,\mathrm{W\,m^{-2}}$ is close to the saturation limit. Intensities around $100\,\mathrm{W\,m^{-2}}$ still aim for comparatively good results whereas the graph for $50\,\mathrm{W\,m^{-2}}$ already indicates a significant slow-down of the deexcitation process. These observations are valid for both n' values investigated.

The simulation results in Fig. 3.7e and 3.7f show how microwaves can be used to decrease the THz power necessary to efficiently populate the ground state. The rather high THz intensities found in Fig. 3.7c and 3.7d are due to the fact that the saturation limit is only reached when levels that are depopulated by the laser can be repopulated from within the mixed Rydberg state distribution at an equally high rate. To assure such optimal conditions, microwaves can be used to efficiently drive $\Delta n = 0$ transitions instead of relying solely on THz light. The results in Fig. 3.7 indicate that 60 % of the atoms can be deexcited to ground state with a THz intensity of $10\,\mathrm{W\,m^{-2}}$ – that is a decrease of more than an order of magnitude when compared to the prior plots – when adding microwaves with intensities of $20\,\mathrm{W\,m^{-2}}$. As already pointed out, powerful microwave sources exist and are thus readily available to experiments. Consequently, for the sake of simplicity, here as well a *flat* microwave scaling has been implemented.

In conclusion, the use of a deexcitation laser allows for an even faster close to unity ground state population when comparing to the previously investigated THz and microwave schemes. Especially the choice of $n' = 25$, $n'' = 3$, THz ($10\,\mathrm{W\,m^{-2}}$)

and microwave ($20\,\mathrm{W\,m^{-2}}$) mixing as well as a visible laser ($1 \times 10^7\,\mathrm{W\,m^{-2}}$) seems experimentally promising (cf. Fig. 3.7f). The achieved ground state fraction amounts to $\sim 60\,\%$ within 50 µs. Again, for more technical comments on the laser feasibility the reader is pointed toward subsection 4.1.3.

3.4 Stimulated radiative recombination

The deexcitation studies presented in section 3.2 and 3.3 investigated how to couple a large number of states to ones that decay fast via spontaneous emission toward ground state. The case of stimulated radiative recombination (srr) within an antiproton-positron plasma, where a laser couples the continuum to a bound $\overline{\mathrm{H}}$ state, is a very similar process to efficiently obtain atoms in ground state.

As will be detailed in subsection 3.4.1, the effectiveness of srr can be investigated relying on rate equations. Considering the coupling of several continuum levels to a single bound level with a srr laser, the srr rate competes with photoionization back to the continuum as well as the decay of the bound level to lower lying manifolds that can be due to collisions, spontaneous emission, ejection out of the laser zone, etc. Here the analogy to the deexcitation of bound levels is apparent. Dealing with bound states, the population of a single level was simply $1/N$ with N being the number of levels dealt with. Within the continuum a plasma degeneracy parameter $n_{e^+}Q_T^{-1}$ can be defined where n_{e^+} is the positron plasma density and $Q_T = \left(\frac{2\pi m k_B T}{h^2}\right)^{3/2}$ the translational partition function. The population of a single continuum level is expressed, using the Boltzmann factor, by $N_1 = n_{e^+}Q_T^{-1}e^{-E/k_BT}$. Now, referring back to the generic model developed in section 3.1, it is obvious that the plasma degeneracy parameter is the ultimate limitation to how fast population can be accumulated in the bound levels. Assuming a 10 K and $1 \times 10^8\,\mathrm{cm^{-3}}$ positron plasma leads to a degeneracy parameter $n_{e^+}Q_T^{-1} \sim 1.3 \times 10^{-9}$. Comparing srr to the deexcitation of, for example, the $\sim 10^4$ levels with $20 \leq n \leq 30$ to a given target state the process is slower by a factor 10^5. However, considering cascades that end up at levels decaying on a few ns timescale (i.e. $n = 2$ or $n = 3$, such as previously suggested in view of deexcitation of bound levels) leads to ground state formation rates of

$$n_{e^+}Q_T^{-1}\Gamma^{\mathrm{d}} \approx 1\,\mathrm{s^{-1}}. \tag{3.6}$$

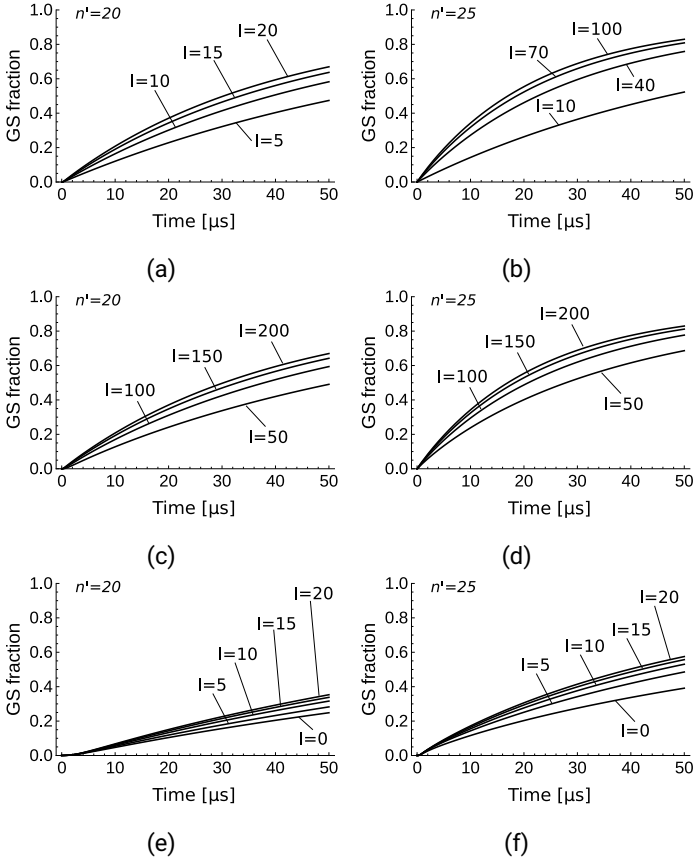

Figure 3.7: Ground state fraction as a function of time. State mixing occurs from $n = 30 \rightarrow n' = 20$ (left column) and $n' = 25$ (right column). A laser stimulates $n' \rightarrow n'' = 3$ transitions (intensities in $10^5\,\mathrm{W\,m^{-2}}$ per 500 MHz bandwidth). First line: Different laser intensities and a given total THz intensity of $200\,\mathrm{W\,m^{-2}}$. Second line: Different total THz intensities and a fixed laser intensity of $20 \times 10^5\,\mathrm{W\,m^{-2}}$ (left) and $100 \times 10^5\,\mathrm{W\,m^{-2}}$ (right). Third line: Fixed THz ($10\,\mathrm{W\,m^{-2}}$) and laser intensity ($20 \times 10^5\,\mathrm{W\,m^{-2}}$ (left) and $100 \times 10^5\,\mathrm{W\,m^{-2}}$ (right)) and different total microwave intensities. Reprinted from [1].

Laser stimulated 3BR antihydrogen formation via srr has been proposed in [54, 89–92] and was demonstrated on hydrogen in [93, 94]. However, the realization of a laser-induced $\overline{\mathrm{H}}$ formation making use of a CO_2 laser that couples the continuum to the $n = 11$ manifold failed [95]. Part of the explanation given was the competing 3BR rate that populates, for a non-correlated plasma [96], a multitude of levels at a rate [35]

$$\Gamma^{3\mathrm{BR}} \sim 160\,\mathrm{s}^{-1} \left(\frac{n_{e^+}}{10^8\,\mathrm{cm}^{-3}}\right)^2 \left(\frac{10\,\mathrm{K}}{T}\right)^{4.5}. \tag{3.7}$$

It is however noteworthy to mention that different 3BR rates have been experimentally measured [97].

3.4.1 Theory of stimulated radiative recombination

The srr process can be theoretically studied using a) standard srr theory, b) rate equations or c) an analogy with the photoassociation process. This section demonstrates the consistency of the aforementioned approaches which is under any circumstance very useful to understand the physics at play.

Milne relations with photoionization

In a typical stimulated radiative recombination process the srr rate at which a positron can be associated to an antiproton is given, per antiproton, by [98]

$$\Gamma^{\mathrm{srr}}_{\mathrm{j}\to\mathrm{i}} = n_{e^+} \int_0^\infty \frac{I(\nu)}{h\nu} \sigma^{\mathrm{srr}}_{\mathrm{j}\to\mathrm{i}} v f(v) \mathrm{d}v, \tag{3.8}$$

where the label i denotes a single, non-degenerate antiproton state and j a bound one, respectively. The srr cross section is noted $\sigma^{\mathrm{srr}}_{\mathrm{j}\to\mathrm{i}}$, the positron plasma density n_{e^+}, the laser irradiance $I = \int I(\nu)\,\mathrm{d}\nu$ and the velocity distribution can be, in the given case, assumed to be Maxwellian $f(v) = 4\pi v^2 \left(\frac{m}{2\pi k_B T}\right)^{3/2} e^{-\frac{1}{2}mv^2/k_B T}$. Intra-continuum rates amount, compared to induced positron capture and for typical e^+ densities, to only $< 6\,\%$ and will consequently be neglected [90]. Thus, the summed srr rate toward a level i is given by $\Gamma^{\mathrm{srr}}_{\mathrm{i}} = \sum_{\mathrm{j}} \Gamma^{\mathrm{srr}}_{\mathrm{j}\to\mathrm{i}}$ that only competes

with spontaneous emission and the photoionization (pi) process. With $E_0 = \kappa^2 Ry = h\nu - Ry/n'^2 = \frac{1}{2}mv^2$ (or written in differential form $mv\mathrm{d}v = h\nu\mathrm{d}\nu$), the energy above the ionization threshold, a link between the laser frequency ν and the positron velocity v can be established. The photoionization rate from a level i can then be written as $\Gamma_{\mathrm{i}}^{\mathrm{pi}} = \sum_{\mathrm{j}} \Gamma_{\mathrm{i}\to\mathrm{j}}^{\mathrm{pi}}$, where

$$\Gamma_{\mathrm{i}\to\mathrm{j}}^{\mathrm{pi}} = \int \frac{I(\nu)}{h\nu} \sigma_{\mathrm{i}\to\mathrm{j}}^{\mathrm{pi}}(\nu)\mathrm{d}\nu. \tag{3.9}$$

The Milne relation links, based on the detailed balance or microscopic reversibility principle[3], the capture cross section (free $\to$ bound) toward a particular level to the absorption cross section (bound $\to$ free) from this level. Indeed, the sum $\Gamma_{\mathrm{j}\to\mathrm{i}}^{\mathrm{srr}} + \Gamma_{\mathrm{j}\to\mathrm{i}}^{\mathrm{rr}}$ of stimulated (srr) and radiative recombination (rr) of positrons with velocities between v and $v + \mathrm{d}v$ is balanced by the photoionization $\Gamma_{\mathrm{i}\to\mathrm{j}}^{\mathrm{pi}}$ by photons of frequencies between ν and $\nu + \mathrm{d}\nu$. The induced downward transitions in thermodynamic equilibrium differ from the photoionization rates only by a factor $e^{-h\nu/kT}$ which can be rewritten as [100]

$$\Gamma_{\mathrm{j}\to\mathrm{i}}^{\mathrm{rr}} = \left(1 - e^{-h\nu/kT}\right) \Gamma_{\mathrm{i}\to\mathrm{j}}^{\mathrm{pi}}. \tag{3.10}$$

Assuming a Saha-Boltzmann thermal equilibrium ($n_{e^+}\Lambda_T^3 n'^2 e^{R_y/n'^2 k_B T}$) and under Planck irradiance (where spontaneous emission is a factor $\bar{n} = \frac{1}{e^{h\nu/k_B T}-1}$ smaller than the stimulated transitions) one then finds the Milne relation

$$\sigma_{\mathrm{j}\to\mathrm{i}}^{\mathrm{rr}}(v) = \left(\frac{h\nu}{mvc}\right)^2 \frac{g_i}{g_j} \sigma_{\mathrm{i}\to\mathrm{j}}^{\mathrm{pi}}(\nu) \tag{3.11}$$

where, to be more general, degeneracy parameters g_{i} and g_{j} have been added. For instance the (n', l') level is degenerated $2(2l'+1)$ times. It is worth noting that the Milne relation is temperature-independent although throughout its derivation a thermal equilibrium was assumed. Going back to non degenerate levels and consequently using notation that accounts for the electron spin such as $\mathrm{i} = |n'k'm'm'_s\rangle$ and $\mathrm{j} = |Ekmm_s\rangle$ (obviously here $g_{\mathrm{i}} = g_{\mathrm{j}} = 1$), the previously found relations can

[3]Here, the terminology is not very consistent throughout literature. "Detailed balance" could be referred to as "microscopic reversibility" and vice versa; an overview is given in [99].

be combined to the fundamental relation [1]

$$\Gamma^{\mathrm{srr}}_{\mathrm{j}\to\mathrm{i}} = n_{e^+} Q_T^{-1} e^{-E_0/k_B T} \frac{1}{2} \Gamma^{\mathrm{pi}}_{\mathrm{i}\to\mathrm{j}} \tag{3.12}$$

with $Q_T = \Lambda_T^{-3}$, where $\Lambda_T = \frac{h}{\sqrt{2\pi m k_B T}}$ is the thermal de Broglie wavelength.

Rate equations

A level $\mathrm{i} = |n'k'm'm'_s\rangle$ is populated by srr from a continuum state j. As shown before, this level is photoionized at a rate $\Gamma^{\mathrm{pi}}_{\mathrm{i}\to\mathrm{j}}$ or decays at a rate $\Gamma^{\mathrm{d}}_{\mathrm{i}}$ toward ground state. Γ^{a} is the association rate at which the ground state is populated. The resulting set of rate equations is illustrated in Fig. 3.8.

Within the antiproton-positron plasma the particles encounter collisions. Subsection 3.4.2 lays down in detail the resulting mixing processes. For now it is sufficient to consider the continuum to be a steady state. Thus, the collisional rates are assumed to be higher than the laser stimulated srr rates toward bound levels i – this is commonly adopted in srr models, but important to be pointed out. The population of all individual continuum levels N_{j} is consequently constant and will, in the following, be simply labeled N_c. Since the bound level i is coupled to the continuum by the srr and photoionization rates, its population N_i is constant as well. Now, the rate toward ground state can be written as $\Gamma^{\mathrm{a}}_{\mathrm{i}} = \Gamma^{\mathrm{d}}_{\mathrm{i}} N_{\mathrm{i}} = \frac{\Gamma^{\mathrm{srr}}_{\mathrm{i}} \Gamma^{\mathrm{d}}_{\mathrm{i}}}{\Gamma^{\mathrm{pi}}_{\mathrm{i}} + \Gamma^{\mathrm{d}}_{\mathrm{i}}}$. Comparing to previous results one finds $N_c = n_{e^+} Q_T^{-1} e^{-E_0/k_B T}/2$ and $\Gamma^{\mathrm{srr}}_{\mathrm{j}\to\mathrm{i}} = N_c \Gamma^{\mathrm{pi}}_{\mathrm{i}\to\mathrm{j}}$. The total association rate can then be found by summing Γ^{a} over the degeneracy g_{i} of the bound states and replacing $\Gamma^{\mathrm{srr}}_{\mathrm{i}}$ by the relation found in the prior step:

$$\Gamma^{\mathrm{a}} = \sum_{i=1}^{g_{\mathrm{i}}} \Gamma^{\mathrm{a}}_{\mathrm{i}} = n_{e^+} Q_T^{-1} e^{-E_0/k_B T} \frac{1}{2} \sum_{\mathrm{i}=1}^{g_{\mathrm{i}}} \frac{\Gamma^{\mathrm{pi}}_{\mathrm{i}} \Gamma^{\mathrm{d}}_{\mathrm{i}}}{\Gamma^{\mathrm{pi}}_{\mathrm{i}} + \Gamma^{\mathrm{d}}_{\mathrm{i}}}. \tag{3.13}$$

Under the assumption of π polarized light (i.e. $\Delta m = 0$), switching from states $|Elmm_s\rangle$ to $|nlm\rangle$ ones simply introduces a factor 2 due to the electron spin so that $\Gamma^{\mathrm{srr}}_{Elm\to n'l'm'} = 2 \times \Gamma^{\mathrm{srr}}_{Elmm_s\to n'l'm'm_s}$. Then, for $|nlm\rangle$ states (the same obviously applies to the $|nkm\rangle$ basis that will later be used when simulating the srr process in

a magnetic field environment) that do not incorporate the spin quantum numbers, $N_1 = 2N_c = n_{e^+} Q_T^{-1} e^{-E_0/k_B T}$ and

$$\Gamma^{\mathrm{a}} = N_1 \sum_{\mathrm{i}} \frac{\Gamma_{\mathrm{i}}^{\mathrm{pi}} \Gamma_{\mathrm{i}}^{\mathrm{d}}}{\Gamma_{\mathrm{i}}^{\mathrm{pi}} + \Gamma_{\mathrm{i}}^{\mathrm{d}}} = n_{e^+} Q_T^{-1} e^{-E_0/k_B T} \frac{\Gamma_{\mathrm{i}}^{\mathrm{pi}} \Gamma_{\mathrm{i}}^{\mathrm{d}}}{\Gamma_{\mathrm{i}}^{\mathrm{pi}} + \Gamma_{\mathrm{i}}^{\mathrm{d}}}. \tag{3.14}$$

Photoassociation

The same result can be derived relying on photoassociation theory that has been developed to describe the formation of molecules throughout a scattering process of two atoms that absorb a photon [101–103]. Stimulating such a process with a narrow-band laser of frequency ν, the association rate $\Gamma^{\mathrm{a}}_{\rightarrow n'l'm'm'_s}$ can be expressed as [1]

$$n_{e^+} \frac{1}{h Q_T} \int e^{-E/k_B T} \frac{1}{2} \sum_{m_s} \sum_{lm} |S|^2 \mathrm{d}E. \tag{3.15}$$

$Q_T = \left(\frac{2\pi\mu k_B T}{h^2}\right)^{3/2}$ describes the center of mass (μ) movement and the S matrix element is defined, for a scattering energy E, by

$$|S|^2 = \frac{\hbar\Gamma^{\mathrm{b}} \hbar\Gamma^{\mathrm{d}}}{(E - E_0)^2 + (\hbar(\Gamma^{\mathrm{b}} + \Gamma^{\mathrm{d}})/2)^2},$$

where Γ^{b} and Γ^{d} denote the light stimulated rate toward a bound level $|n'l'm'm'_s\rangle$ and the decay rate due to spontaneous or collisional deexcitation. Γ^{b} can be determined by Fermi's Golden Rule (cf. subsection 2.2.1), but more importantly equals the photoionization rate Γ^{pi}. Assuming the positron continuum to be broader than any atomic linewidth broadening only the energy above threshold $E_0 = \kappa R_y$ matters and one recovers equation Eq. 3.14 showing that the approaches are equivalent.

3.4.2 Collisional mixing

State-of-the-art $\overline{\mathrm{H}}$ formation temperatures correspond to velocities of $\sim 1000\,\mathrm{m\,s^{-1}}$. For a plasma size of the order of mm the atoms consequently encounter positron

and antiproton collisions within the plasma for $\sim 1\,\mu s$. Such collisional processes are known to efficiently stimulate atomic transitions [35, 36, 104, 105]. Inside the plasma (in the antihydrogen reference frame), energetic antiprotons and positrons introduce electric fields that distort the $\overline{\mathrm{H}}$ atomic energy levels. Latter electric field can be approximated by $E \sim e^2/4\pi\epsilon_0 R^2$, where R denotes the distance between the atom and antiproton or positron. Mixing of atomic states occurs as soon as the electric field introduced by the charged particles amounts to the atomic levels' energy spacing. The atomic Stark shift can be expressed as $\sim n^2 E$ (in atomic units).

In the presently treated regime where $n \sim 30$, consecutive n-manifolds are still well separated in energy. As a consequence, the required electric field to achieve efficient mixing is high and dominates the effect on the quantum states compared to the $\sim 1\,\mathrm{T}$ magnetic field necessary to confine the plasma. The $n \to n'$ mixing rates can then be well approximated in a pure electric field and are, for a positron temperature T_{e^+} and density n_{e^+}, of the order of $10^{-6}\,\mathrm{cm^3\,s^{-1}} n_{e^+} \left(\frac{T_{e^+}}{10\,\mathrm{K}}\right)^{-0.17} n'^{6.66}/n^5$ [106–109]. For a 10 K plasma and $n \sim 30$ this leads to mixing timescales of several tens of µs. Despite the fact that very long or dense plasmas might exhibit enhanced mixing capabilities, the n-mixing will be in the following neglected.

The Zeeman energy spacing between m-states amounts in a 1 T magnetic field to $\sim 14\,\mathrm{GHz}$ (cf. Fig. 2.5). Using the aforementioned relations, this leads to an impact parameter of $R \sim 1\,\mu\mathrm{m}$.

The same considerations result in an impact parameter of $R \sim 13\,\mu\mathrm{m}$ for k-mixing where the energy spacing amounts to some 100 MHz.

A Landau-Zener model can be used to estimate the mixing efficiencies. Typical positron velocities $v = \sqrt{k_B T/m} \sim 10^4\,\mathrm{m\,s^{-1}}$ lead to collisional times R/v that are compatible with the frequency spacing at crossing (i.e. the Rabi frequency). The mixing rate can thus be approximated by $n_{e^+}\pi R^2 v$ which is a few per µs for m-mixing and almost one per ns for k-mixing. Thus, in the following the antihydrogen levels will be assumed to be only mixed in k. Mixing in m will at best be partial, whereas n mixing is a negligibly small effect [1].

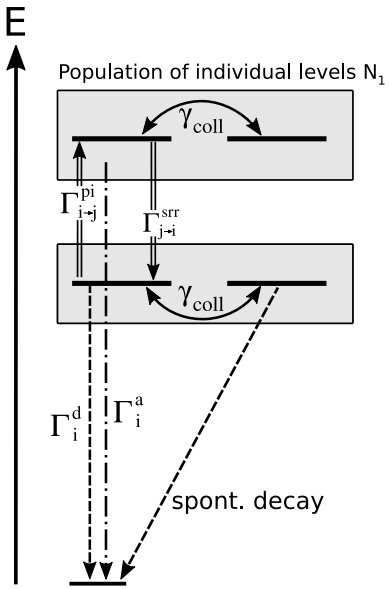

Figure 3.8: Illustration of the nomenclature used for the decay rates involved in the simple srr process. The collisional rates responsible for the k-mixing in the bound states and population reshuffling in the continuum are indicated by γ_{coll}. Slightly modified from [1].

3.4.3 Simple stimulated radiative recombination

Subsection 3.4.1 demonstrated the consistency of different theoretical srr approaches. In the following, the use of rate equations seems to be the most natural and instructive (in part because they were extensively used for the deexcitation of bound levels and a similar combined scheme will be investigated in subsection 3.4.4). Here, the simplest srr case is treated where a laser recombines positrons from the continuum into bound n' levels that then decay toward ground state without relying on light stimulated transitions (i.e. due to spontaneous emission, collisional deexcitation, etc.). The scheme is illustrated in Fig. 3.8.

It has been shown in section 3.4.2 that the considered levels can be assumed to

be mixed in k whereas m and in particular n should stay rather well defined. Referring back to Eq. 3.14, the averaged association rate for a set of (n', m') levels can be written as

$$\Gamma^{\mathrm{a}} = N_1 \sum_{m'=-(n'-1)}^{n'-1} (n' - |m'|) \frac{\Gamma^{\mathrm{pi}}_{m'} \Gamma^{\mathrm{d}}_{m'}}{\Gamma^{\mathrm{pi}}_{m'} + \Gamma^{\mathrm{d}}_{m'}}.$$

The association rate is maximized for $\Gamma^{\mathrm{pi}}_{m'} \gg \Gamma^{\mathrm{d}}_{m'}$ and, in this limit, becomes $\Gamma^{\mathrm{a}} = N_1 \sum_{m'=-(n'-1)}^{n'-1} (n' - |m'|) \Gamma^{\mathrm{d}}_{m'}$. Useful scaling laws of $\Gamma^{\mathrm{d}}_{m'}$ and the srr cross sections are derived in the appendix of [1], section 5 and 6. Fortunately, both the spontaneous emission rates as well as the srr cross sections (cf. in particular Fig. 11 in [1]) are maximal at low m reducing the spectral bandwidth required to drive the most efficient transitions when seeking to populate the ground state. This reduces the needed srr light intensity and laser power. Fig. 3.9 shows simulation results for $n' = 11$ (at this wavelength of 11 µm powerful CO_2 lasers exist) and $n' = 3$ (where Ti:Sa lasers are able to produce powerful light at 832 nm).

Targeting the $n' = 3$ states leads to srr laser saturation powers in the few kW mm^{-2} region. The laser power required can be reduced to some tenths of W mm^{-2} recombining positrons to the weaker bound $n' = 11$ levels that exhibit an elevated srr cross section. In this latter case however, the ground state formation rate drops to a few hundredths of ground state $\overline{\mathrm{H}}$ formed per antiproton and second. In both cases the $\overline{\mathrm{H}}$ srr combination rates can be boosted stimulating not just $\Delta m = 0$ transitions, but also employing $\sigma^{\pm}$ polarized light. Clearly, in all cases the srr rates are well below the 3BR rates of 160 s^{-1} (cf. Eq. 3.7).

3.4.4 Stimulated radiative recombination followed by stimulated deexcitation

The $\overline{\mathrm{H}}$ ground state formation rates achievable via simple srr can be further enhanced by stimulating the decay of the bound n' levels the laser recombines the positrons to. Such an idea has been conceptionally outlined in [54]. This section is, building upon the findings above, dedicated to a quantitative analysis of the achievable rates in an external magnetic field. Again, the fact that the ssr cross sections peak at low m plays in favor of the capabilities to quickly populate the

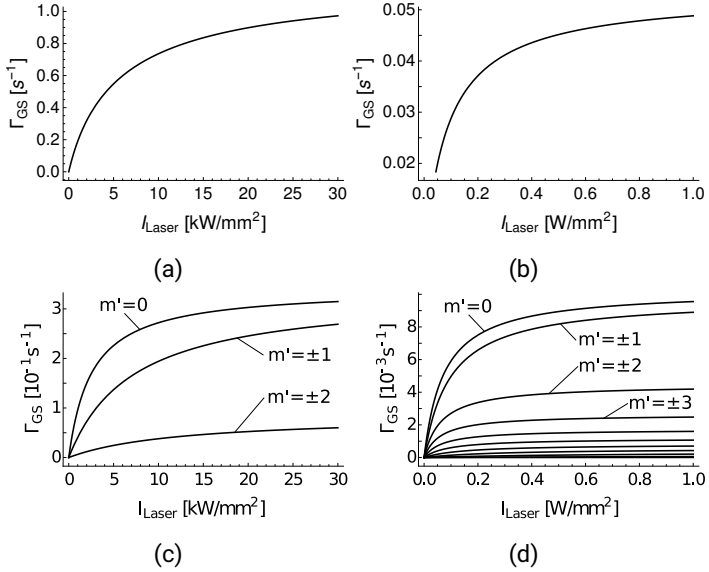

Figure 3.9: A π polarized srr laser (832 nm on the left and 11 µm on the right) drives transitions from the continuum to $n' = 3$ (left) and $n' = 11$ (right). The decay cascade $n' \to n = 1$ relies on spontaneous emission. The top line shows the ground state association rate per antiproton per second summed over all possible m' states while the bottom line indicates the rate for each $|m'|$ separately. The assumed positron plasma density is 1×10^8 cm^{-3} and the temperature 10 K. Reprinted from [1].

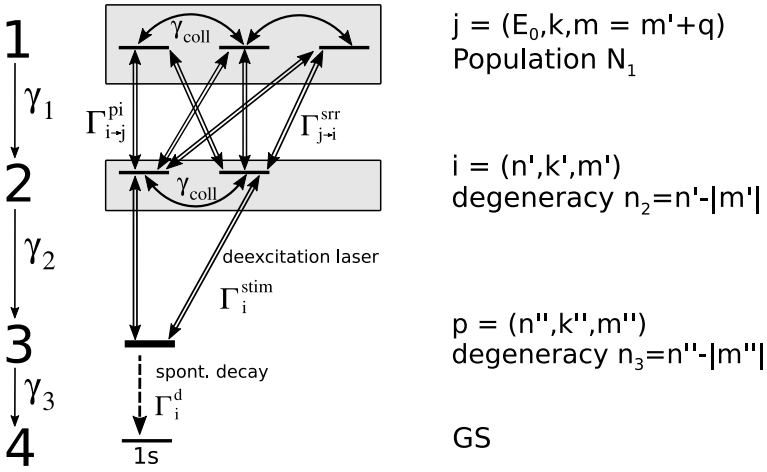

Figure 3.10: Level system as obtained when incorporating a full k mixing, a srr laser and a stimulated deexcitation ($2 \to 3$). Slightly modified from [1].

ground state. Indeed, as a consequence the srr predominantly populates low m states that are (a) the most numerous with a degeneracy of $n' - |m'|$ and (b) accessible through light stimulated transitions ($|\Delta m| \leq 1$). Thus, a large part of the recombined $\overline{\text{H}}$ population can be efficiently addressed with a deexcitation laser coupling the population toward the $n'' = 2$ or $n'' = 3$ manifold.

Fig. 3.10 illustrates the now considered system incorporating a srr laser (polarization q) coupling the continuum to bound (n', m') levels with $m' = m + q$. Additionally, a deexcitation laser (polarization q'') drives transitions $(n', m') \to (n'', m'')$ with $m'' = m' + q''$. The (n'', m'') levels decay spontaneously to ground state. This

leads to the following equations:

$$\begin{aligned}
N_{1,\mathrm{j}} &= n_{e^+} Q_T^{-1} e^{-E_0/k_B T} \\
\frac{\mathrm{d}N_{2,\mathrm{i}}}{\mathrm{d}t} &= \sum_{\mathrm{j}} \gamma_{1;\mathrm{i},\mathrm{j}} (N_{1,\mathrm{j}} - N_{2,\mathrm{i}}) - \sum_{\mathrm{p}} \gamma_{2;\mathrm{i},\mathrm{p}} (N_{2,\mathrm{i}} - N_{3,\mathrm{p}}) + \gamma_{\mathrm{coll}} \sum_{\mathrm{i}'} (N_{2,\mathrm{i}'} - N_{2,\mathrm{i}}) \\
\frac{\mathrm{d}N_{3,\mathrm{p}}}{\mathrm{d}t} &= \sum_{\mathrm{i}} \gamma_{2;\mathrm{i},\mathrm{p}} (N_{2,\mathrm{i}} - N_{3,\mathrm{p}}) - \gamma_{3;\mathrm{p}} N_{3,\mathrm{p}} + \gamma_{\mathrm{coll}} \sum_{\mathrm{p}'} (N_{3,\mathrm{p}'} - N_{3,\mathrm{p}}) \\
\frac{\mathrm{d}N_4}{\mathrm{d}t} &= \sum_{\mathrm{p}} \gamma_{3;\mathrm{p}} N_{3,\mathrm{p}}
\end{aligned} \tag{3.16}$$

The collisional rate γ_{coll} is assumed to be the same within the continuum and (n', m') levels which can be justified simply by the fact that it is acting on a ns timescale and thus much faster than all other rates.

Similar to what has been seen in the prior sections dealing with deexcitation of bound states, the stimulated rates quickly lead to an equipopulation and thus a steady-state where $N_{2,\mathrm{i}'} = N_{2,\mathrm{i}}$ and $N_{3,\mathrm{p}'} = N_{3,\mathrm{p}}$. Making use of this fact, it is possible to employ a simplified notation where $N_2 = N_{2,\mathrm{i}}$ and $N_3 = N_{3,\mathrm{i}}$ (the degeneracy of each level is indicated in Fig. 3.10). Summing over i and p leads to

$$\begin{aligned}
N_1 &= n_{e^+} Q_T^{-1} e^{-E_0/k_B T} \\
\frac{\mathrm{d}N_2}{\mathrm{d}t} &= -(n_3\gamma_2 + n_1\gamma_1) N_2 + \gamma_1 n_1 N_1 + n_3 \gamma_2 N_3 \\
\frac{\mathrm{d}N_3}{\mathrm{d}t} &= n_2\gamma_2 N_2 - n_2\gamma_2 N_3 - \gamma_3 N_3 \\
\frac{\mathrm{d}N_4}{\mathrm{d}t} &= n_3 \gamma_3 N_3
\end{aligned} \tag{3.17}$$

with the average rates $\gamma_1 = \frac{1}{n_1 n_2} \sum_{\mathrm{i,j}} \gamma_{1;\mathrm{i,j}}$, $\gamma_2 = \frac{1}{n_2 n_3} \sum_{\mathrm{i,p}} \gamma_{2;\mathrm{i,p}}$ and $\gamma_3 = \frac{1}{n_3} \sum_{\mathrm{p}} \gamma_{3;\mathrm{p}}$. This gives a steady state of $N_3 = N_1 \frac{1}{1+\gamma_3 \left(\frac{1}{n_2\gamma_2} + \frac{n_3}{n_1 n_2 \gamma_1} \right)}$ and consequently (cf. the derivation of Eq. A4 in [1])

$$\Gamma^{\mathrm{a}} = n_3\gamma_3 N_3 = n_3 \gamma_3 N_1 \frac{1}{1 + \frac{n_3\gamma_3}{n_2} \left(\frac{1}{n_3\gamma_2} + \frac{1}{n_1\gamma_1} \right)}. \tag{3.18}$$

Similar to the conclusions in section 3.1 relying on a generic deexcitation model, the derived equations again outline the following points:

- The achievable ground state population increases with a reduced lifetime toward ground state of the last levels to which transitions are stimulated.
- Throughout the deexcitation process the slowest involved rate limits the population of the ground state. Consequently it is desirable to have equal rates (cf. THz power scaling for stimulated deexcitation).
- The maximum achievable rate is given by the full transfer so that $N_3 = N_1$ so that $\Gamma^{\mathrm{a}}_{\mathrm{max}} = n_3 \gamma_3 N_1$.

These equations recover the simple srr case when N_2 is assumed to represent the continuum.

Fig. 3.11 shows simulation results for $n'' = 2$ and $n'' = 3$. The association rate (thus the $\overline{\mathrm{H}}$ ground state production rate) is plotted as a function of the laser powers required to stimulate the transitions from the continuum toward $n' = 11$ and $n' = 11 \rightarrow n''$ with $n'' = 3$ (top) and $n'' = 2$ (bottom). The deexcitation laser stimulating the $n' \rightarrow n''$ transitions has a spectral width of 500 MHz which is the bandwidth required to cover the 1 T diamagnetic broadening of the $n' = 11$ manifold (cf. Fig. 2.5 for $n = 20$). For simplicity, a uniform laser power over all addressed transitions is assumed (top-hat spectral profile).

The results plotted in Fig. 3.11a employing stimulated transitions from $n' = 11 \rightarrow n'' = 3$ lead to laser powers (for both the 11 µm srr and the 885 nm deexcitation laser) of the order of 10 W. This is within experimental reach. The maximal achievable ground state $\overline{\mathrm{H}}$ association rate is 0.85 s^{-1}. This is slightly below what is found in Fig. 3.11b showing a plot with $n'' = 2$. However, in the latter case the $n' = 11 \rightarrow n'' = 2$ laser powers at a wavelength of 377 nm required amount to $\sim 100\,\mathrm{W\,mm^{-2}}$ which is undoubtedly difficult to achieve. In summary, using two lasers of 10 W to drive transitions from the continuum to $n' = 11$ and subsequently to $n'' = 3$ allows to obtain just slightly below 1 $\overline{\mathrm{H}}$ per antiproton per second. For $\sim 10^6$ trapped antiprotons and plasma interaction times of the order of milliseconds this gives ~ 1000 $\overline{\mathrm{H}}$ in ground state per formation cycle which is a significant improvement over the currently observed rates.

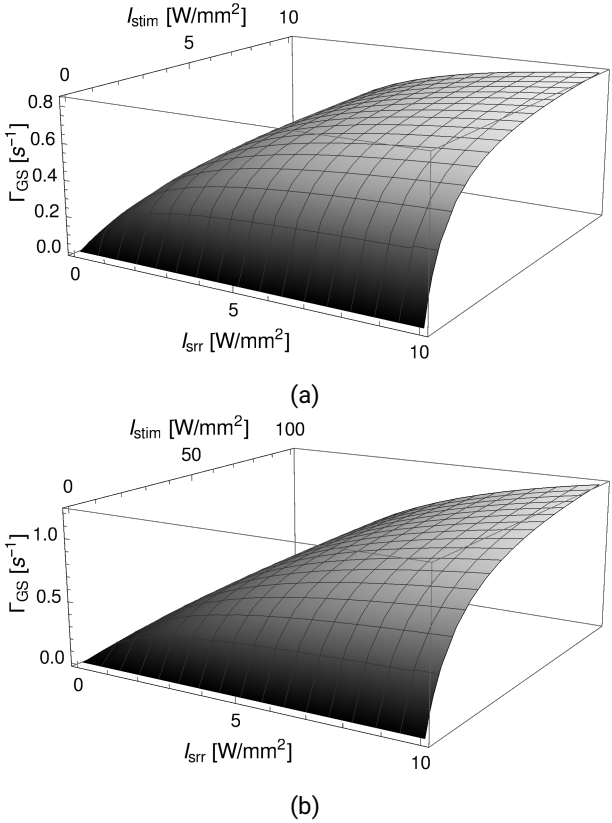

Figure 3.11: Ground state $\overline{\mathrm{H}}$ atoms formed per antiproton and second as a function of the srr and deexcitation laser intensities. The srr laser (π polarization) stimulates the transitions from the continuum to $n' = 11$ (srr step) whereas the deexcitation laser then (stimulated step) connects n' to $n'' = 3$ (a) or $n'' = 2$ (b). The deexcitation laser is π polarized with a FWHM bandwidth of 500 MHz. The assumed positron plasma density is 1×10^8 cm^{-3} and the temperature 10 K. Reprinted from [1].

3.5 Discussion

The simulation results discussed above are put into the context of beam experiments at the AD in subsection 3.5.1. The use-case of stimulated deexcitation along the magnetic field gradient within a neutral atom trap for enhanced trapping and cooling is discussed in subsection 3.5.3. The link of the presented studies to collisional deexcitation is established in subsection 3.5.2.

3.5.1 Use-case for in-beam experiments

It has been shown in section 3.2 that Rydberg $\overline{\mathrm{H}}$ produced via CE can be efficiently brought to ground state relying on a pulsed deexcitation scheme that employs an electric field to the already present magnetic one to mix the initially populated states. This mixing then allows to address the Rydberg population with a deexcitation laser. The studies presented in [2, 3] treat a broadband laser with a spectral width of 5000 GHz that covers all $n \rightarrow n' = 3$ transitions with $20 \leq n \leq 30$. This work complements the latter case treating a comparatively narrow laser stimulating only transitions from a single target manifold ($n' = 30$, 25 or 20) down to a low lying n' manifold ($n' = 3$ in Fig. 3.2 and $n' = 2$ in Fig. 3.3).

Concluding on an ideal field mixing and deexcitation scheme for CE depends on many parameters (including experimental constraints, etc.). In general, however, the simulations clearly indicate that the required laser power rapidly increases when targeting higher n manifolds due to the smaller average transition dipole and the increased necessary spectral laser bandwidth that is needed to cover the Stark and Zeeman broadening of the targeted levels. For the CE case, weighing the impact of some additional key parameters leads to the following considerations [110]:

In a CE reaction, the $\overline{\mathrm{H}}$ formation rate is proportional to the Ps atomic cross section $\propto n^4$ (cf. section 1.2). Relying on stimulated deexcitation, the time available to populate the ground state is determined by the duration that the $\overline{\mathrm{H}}$ atoms stay within the laser zone. In a CE, the $\overline{\mathrm{H}}$ temperature is mainly determined by the transferred antiproton kinetic energy. Thus, the time available for deexcitation scales as the inverse of the $\overline{\mathrm{H}}$ velocity $v_{\overline{\mathrm{H}}}^{-1} \propto \sqrt{T_{\overline{\mathrm{p}}}}^{-1}$. Referring back to the generic

model (cf. section 3.1), it was found to be possible to deexcite one state per nanosecond of a population that is coupled to 10 states that have lifetimes of the order of 10 ns (which is reasonable for $n' = 3$). Now, the number of initially populated levels within a given manifold scales, for degeneracy reasons, as n^2. Additionally, the number of initially populated manifolds depends, due to energy conservation, mainly on the Ps velocity. The Ps kinetic energy $\propto T_{\mathrm{Ps}}$ and the energy spacing of consecutive n manifolds in $\overline{\mathrm{H}} \propto n^{-3}$. Thus, the number of initially populated states $\propto n^2 n^3 T_{\mathrm{Ps}}$. Finally, the number of deexcited levels to ground state per time

$$N_{\mathrm{GS}} \propto \frac{n^4}{n^2 n^3 \times T_{\mathrm{Ps}} \times \sqrt{T_{\overline{\mathrm{p}}}}} = \left(n \times T_{\mathrm{Ps}} \sqrt{T_{\overline{\mathrm{p}}}} \right)^{-1} . \tag{3.19}$$

This result in fact suggests to go lower in n to optimize the number of ground state atoms available. It is worth mentioning again that this is also favorable in terms of laser feasibility.

The simulations laid down in section 3.3 deal with a continuous deexcitation scheme that is applicable to both CE and 3BR. It has been shown that, instead of a $E \times B$ field configuration, which would in the quasi-continuous 3BR case disturb the antiproton and positron plasmas, THz and/or microwave radiation can be used to mix the initially populated $\overline{\mathrm{H}}$ levels. The idea of connecting such a mixed population to low lying states that exhibit short spontaneous lifetimes with a laser is similar. It is worthwhile pointing out again the versatility of state mixing relying on light. In the 3BR case, it is desirable to mix, relying on inter-n manifold (THz) and intra-n manifold (microwave) transitions, the maximum number of levels thus spanning the widest possible range in n to address most initially formed $\overline{\mathrm{H}}$.

A first step toward $\overline{\mathrm{H}}$ deexcitation in beam experiments relying on 3BR might be an investigation of the actual initial quantum state distribution. Up-to-date measurements have been performed at the edge or even outside the formation region [5, 39] thus suffering from low $\overline{\mathrm{H}}$ rates. In order to improve this and in view of optimizing the deexcitation procedure one could, in the first place, restrict the THz and/or microwave light to few (and in the extreme case to a single) n-manifolds. Doing so would result in specific n whose (k, m) sublevels are much more efficiently coupled to the deexcitation laser compared to others which allows to probe the state distribution as present after the formation. For the sole mixing of individual n-manifolds, the required light frequencies lie in the microwave region

and are, compared to the few THz required when deexciting via $\Delta n = -1$ toward low n', much easier to generate. The requirements on the laser intensity can be expected to be similar to, for example, the pulsed $n = 30$ and $n' = 3$ case. The constraint on the spectral width of the light is, however, due to the light mixing, much more relaxed and $I \propto \Gamma_{\mathrm{L}}$.

Such a configuration might as well be the preferred one for a CE production scheme since, here, formation in specific n states can be targeted. Referring back to probing the initial distribution of states, light mixing might be the favored solution compared to crossed electric and magnetic fields. The simulations indicate that $E \times B$ fields, even if optimized for mixing in the presently treated case $n = 30$, still reasonable well mix the levels in neighboring manifolds equally connecting them to the laser. Thus, in such a configuration probing the initial state distribution is much more difficult.

As shown in section 3.4 the deexcitation of bound levels is very similar to the case of stimulated radiative recombination of a positron within a plasma into a bound state of an antiproton. First detailed simulations of such a process within a magnetic field, as detailed in this thesis and [1], suggest that when coupling the n' states populated from the continuum via srr to low lying states with a deexcitation laser considerable ground state $\overline{\mathrm{H}}$ production rates can be achieved. A typical 3BR $\overline{\mathrm{H}}$ formation cycle employing srr and deexcitation lasers with powers within experimental reach yields ground state atom formation rates of ~ 1000 per millisecond. Such association rates are still two orders of magnitude below the 3BR rates, with the key feature that the $\overline{\mathrm{H}}$ are in ground state and directly available for measurements and/or further manipulations to, for example, form a beam. A further advantage is the increased robustness of the srr process toward changes in the positron temperature, which is a parameter 3BR is comparatively sensitive to, thus facilitating experimental operation.

The proposed techniques to enhance the ground state population directly at the $\overline{\mathrm{H}}$ formation region for both CE and 3BR address a long standing issue within the community. Even though the quantum state distribution present after formation has not been measured experimentally yet, highest spontaneous rates toward circular states quickly populate the high (k, m) levels. This is the main reason why state mixing is such a crucial process rendering the distribution of states accessible through a deexcitation laser. The results found are of particular relevance for experiments relying on the formation of a beam. Increasing the number of $\overline{\mathrm{H}}$ in

ground state allows for an optimized and more efficient magnetic focusing of the beam at the exit of the formation trap. Similarly, techniques like Stark acceleration can be tailored to the properties of the atoms in ground state resulting in a smaller velocity spread and thus a more homogeneous beam available for e.g. atomic interferometry gravity measurements [25].

Further, stimulated deexcitation on the µs timescale has the potential (if pulsed) to provide valuable timing information when the formation relies on a quasi-continuous 3BR production scheme where positron-antiproton plasma interaction times can range from miliseconds up to several seconds. The timing in turn allows to probe the velocity distribution of the formed ground state atoms which is a crucial parameter in an in-beam hyperfine splitting measurement. Further, the Doppler broadening due to finite velocities of antiprotons within the plasma and formed $\overline{\mathrm{H}}$ might allow for a spectral velocity selection through sharp linewidths of the srr and deexcitation light sources (one should note here that such Doppler broadening has not been taken into account throughout the simulations presented in this chapter).

3.5.2 Link to collisional deexcitation

The considerations laid down in section 3.4 included detailed theoretical studies of state mixing via collisional processes within a plasma. It was found that within a typical $\overline{\mathrm{H}}$ formation plasma, state mixing relying on positron impact is efficient to equipopulate the initially populated levels of the formed anti-atoms (n-mixing of the order of several tens of µs, m-mixing of the order of several µs, k-mixing of the order of ns). Instead of using these arguments to simplify the set of rate equations that needs to be solved to asses the efficiency of stimulated radiative recombination (cf. section 3.4), one can consider this to be a deexcitation mechanisms on its own. Indeed, studies on how the interaction time between the nascent antihydrogen atoms and the antiproton-positron formation plasma acts upon the state distribution of the anti-atoms emerging from the plasma in a 3BR have been published in [36].

This raises the idea of deexciting the formed Rydberg anti-atoms in a beam via collisional processes along the passage through an electron plasma that is located downstream the $\overline{\mathrm{H}}$ formation region along the atoms' flight path toward, for

example, the spectroscopy apparatus and detector. In this framework, efforts toward detailed simulations of such a process are ongoing within the ASACUSA collaboration [111]. Based on the considerations laid down in this work and assuming state-of-the-art $\overline{\mathrm{H}}$ formation velocities around 1000 m s^{-1}, a 1 cm long 10 K electron plasma with a density of 1×10^8 cm^{-3} would be sufficient to achieve n-mixing via the process

$$\overline{\mathrm{H}}\,(n) + \mathrm{e}^- \rightarrow \overline{\mathrm{H}}\,(n') + \mathrm{e}^-, \tag{3.20}$$

where $n' < n$. The electron on the right hand side of the reaction carries away the liberated binding energy. However, as shown in the previous sections, for efficient deexcitation the mixing of the states (previously referred to as initial mixing or initial equipopulation of the states) needs to occur on a timescale much faster than the actual deexcitation process via a fast spontaneous emission channel. Thus, higher electron plasma densities will be necessary to establish a "steady-state" deexcitation as has been discussed and simulated in this work. On the other hand, solely spreading out parts of the population toward low n or low m states (this is particularly interesting because here mixing is comparatively fast and lifetimes toward ground states can be very short) may already lead to a significant increase in the number of ground state atoms available for measurements. Such a simplified scheme might be, as has been pointed out earlier in a side note as well, a reasonable trade-off for beam experiments where the atoms' state distribution can evolve for several hundreds of µs after the deexcitation plasma interaction throughout the flight path toward the measurement and detection region.

Compared to radiative atom-light interaction, collisional processes however only offer a quite narrow parameter space for optimization or controlled manipulation of specific states. Major losses of antihydrogen have to be expected due to collisional ionization which is much harder to control compared to shining specific THz and microwave light frequencies to mix states (while limiting ionization losses). Simulation software to determine the evolution of excited (anti-)hydrogen states upon electron impact readily exists (e.g. Yacora on the Web [112]; the code will be later used to study plasma processes in section 4.4.1).

3.5.3 Use-case within a magnetic field gradient

The techniques developed to stimulate the decay of Rydberg antihydrogen atoms toward ground state can be employed along the magnetic field gradient of neutral atom traps. State-of-the-art experiments capture $\overline{\mathrm{H}}$ samples in potential wells of some hundreds of mT which corresponds, for ground state atoms, to typical temperatures around $T_{\mathrm{trap,GS}} = \frac{\mu B}{k} \approx 500\,\mathrm{mK}$, where k is the Boltzmann constant and $\mu = \mu_0$ with the Bohr magneton $\mu_0 = 0.67\,\mathrm{K\,T^{-1}}$. For excited states with magnetic quantum numbers $m > 1$, the effective dipole moment $\mu = \mu_0 m$. Thus, they experience a potential $U = kT \propto m$ leading to enhanced trapping capabilities. Consequently, capturing a distribution of highly excited states allows to initially trap atoms with temperatures $T > T_{\mathrm{trap,GS}}$.

The gas dynamics inside the trapping potential are described by

$$m_a \frac{\mathrm{d}^2 \vec{r}}{\mathrm{d}t^2} = -\vec{\nabla}\left(\vec{B}\cdot\vec{\mu}\right), \tag{3.21}$$

where m_a denotes the atom mass and $\vec{r}$ the position. This results in elevated population densities toward the edges of the trap where the atoms' kinetic energies are minimal. Thus, most spontaneous decay events occur when the atoms are far from the trap center and the potential energy U is close to maximal[4]. The initially formed distribution of $\overline{\mathrm{H}}$ states rapidly collapses to predominantly high m (circular) states [114] that are incidentally the longest lived ones and decay, due to selection rules, via the entire $(n, |m|) \to (n-1, |m|-1)$ cascade toward ground state. Latter decay process step-wise dissipates the potential energy $\Delta U = \mu_0 m$ and effectively cools the atom by flattening the effective trap field gradient. Comprehensive theoretical studies on cooling of trapped antihydrogen via spontaneous emission can be found in [113, 115].

The cooling via spontaneous emission can be reinforced by stimulating the decay toward ground state with light when the atoms' kinetic energies are minimal. Microwaves have been proposed to drive transitions from long lived high m states toward low m ones that exhibit significantly shorter lifetimes. Whereas such radiation has shown to only improve deexcitation results marginally when added

[4] In fact, the elevated magnetic field at the trap edges reinforces this effect by enhancing the spontaneous decay rate (cf. Eq. 2 in [113]). This effect is however not dominant over the considerations due to gas dynamics in typical (comparatively shallow) antihydrogen traps.

to already present THz light (cf. subsection 3.3.2), the mixing of the (k, m) sublevels of a single given n manifold (without THz) seems interesting. Simulations yielded a maximum 1.7 improvement factor in the trapping fraction when comparing to spontaneous emission only [116]. The investigated temperatures, however, lie only between 4 and 16 K. It is noteworthy to additionally mention that a (broadband) deexcitation laser might have significantly enhanced the results found. A second possibility lies in stimulated deexcitation schemes relying on THz radiation driving $\Delta n = -1$ transitions as proposed in this work (cf. Fig. 3.6) [4]. Both methods are illustrated in Fig. 3.12. Atoms at the trap edge are deexcited via short lived m states by driving $(n, |m|) \rightarrow (n, |m| - 1)$ (microwave) or $(n, |m|) \rightarrow (n - 1, |m| - 1)$ (THz) transitions that dissipate the atoms' potential energy.

In most cases the trap oscillation frequencies depend on the atoms' temperature[5]. Thus, the trajectories within the trap are generally chaotic, especially when considering the full three-dimensional case. As already indicated, the transitions must be stimulated when the potential energy is maximal and the atoms are almost at rest. In fact, driving $m \rightarrow m - 1$ transitions close to the trap center, where the potential energy is minimal leads to heating effects and in most cases to undesired trap spillage. A variety of techniques to select the atoms at rest is discussed in [70]. A first possibility lies in focusing the light onto the edge of the trap and then shifting the transition zone toward the trap center as a function of time. This spatial selection allows to gradually deexcite initially slower and slower atoms which total energies are too small to reach the trap edge. The second idea relies on a spectral selection of atoms. In brief, the increased Zeeman shift due to elevated magnetic fields at the trap edge allows to tune the frequency of the light sources in such a way that they address only the slow fraction of the trapped atomic sample. Here again, the initially hottest atoms will reach radii further away from the trap center than slower ones. Thus, detuning the wavelength of the light sources over time allows for a deexcitation of different initial temperature ranges separately (for illustration, please refer back to Fig. 3.12).

Based on a code developed by D. Comparat [70], studies of enhanced trapping through stimulated deexcitation have been performed. The results will be the subject of a shortly forthcoming publication [4]. In contrast to the study in [116], a realistic 40 K Maxwell-Boltzmann velocity distribution is initialized at the trap

[5] Harmonic traps are somewhat particular with a single, velocity independent, oscillation period. The possibilities this opens up will be discussed later in this section.

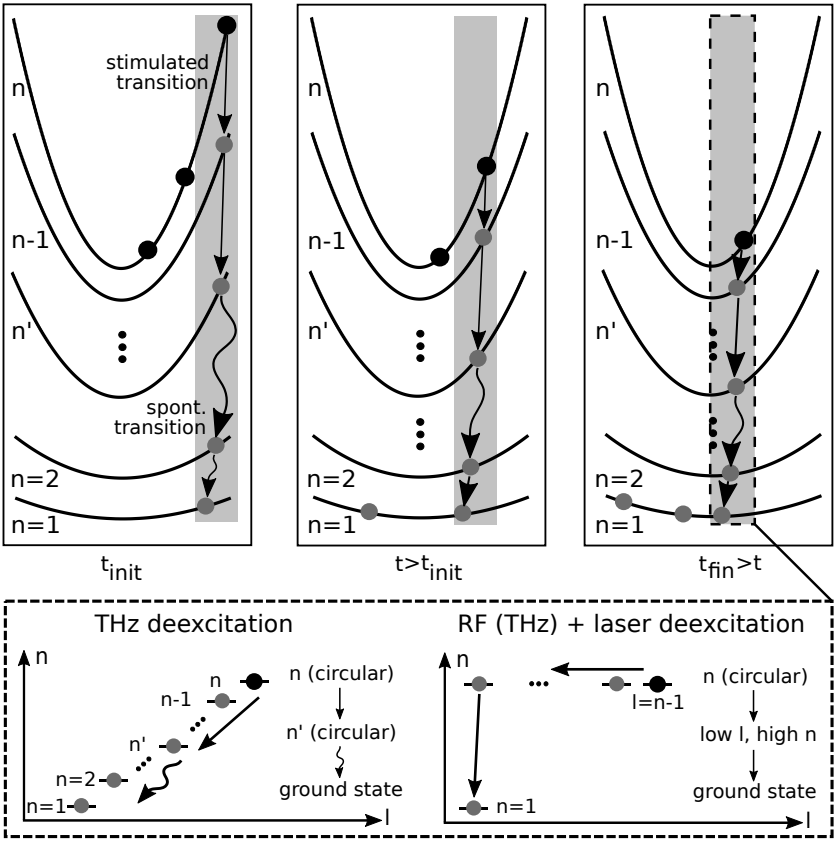

Figure 3.12: Illustration of stimulated deexcitation schemes in a magnetic trap field gradient relying on THz, microwave and/or visible laser light.

center of a ~ 1 cm wide and 0.75 T deep linear cusp trap (anti-Helmholtz coil configuration). The atoms initially populate the $n = 30$ circular state. The gas dynamics are implemented relying on a kinetic Monte-Carlo simulation. Radiative processes are replicated, similar to the studies presented previously, employing rate equations. THz light (top-hat spectral profile) is sent to stimulate (n, m) to $(n-1, m-1)$ transitions. A spectral selection of atoms is implemented and the bandwidth of the light is chosen such that the resulting transition zone covers μB which is the trap depth as seen by ground state atoms. This is a somewhat natural choice since the atoms' maximum kinetic energy acquired throughout their radiative transfer toward ground state must not exceed the final trap depth. The light is initially detuned from the field-free transitions by the maximum Zeeman shift inside the trap (10.5 GHz). The detuning is linearly decreased over a time τ chosen in line with the considerations laid down in [70] (appendix A 1.). For the given configuration, τ is found to be 2.9 ms. Stimulating all THz transitions from $n = 30$ down to $n' = 5$ with a rate of $4 \times 10^7\,\mathrm{s}^{-1}$ results in a ~ 3.5-fold improvement of the trapping fraction compared to spontaneous decay only. Clearly, the generation of light with total intensities of ~ 135 mW in the few THz region remains experimentally challenging. However, trade-offs in the choice of n' as well as the spectral width of the transition zone to reduce the overall required power might be possible.

Finally, an interesting alternative to the schemes discussed above exploits the fact that oscillation frequencies in a harmonic trap potential are velocity independent. Consequently, all atoms with same magnetic moment will come to rest at $T/4$ where T denotes the atoms' oscillation frequency. Thus, one finds time windows where cooling via stimulated deexcitation is most efficient and broadband light sources might be operated in a pulsed mode. This is particularly interesting for $\overline{\mathrm{H}}$ formation via CE where a specific n formation state can be targeted. For initial $\overline{\mathrm{H}}$ distributions that cover a wide range of n levels (and thus magnetic momenta) the limitation of cooling only a single manifold will most likely lead to considerable losses. In such a case, an initial deexcitation to ground state after $\overline{\mathrm{H}}$ formation followed by an excitation to a single high n circular state can be considered. Despite inevitable losses caused by such an intermediate step, the potential gain through excitation of initially fast atoms that exhibit not sufficiently high m to be captured and subsequently cooled can outweigh the deficiencies.

4 Toward controlled Rydberg state manipulation and deexcitation in an atomic hydrogen beam

The simulations performed throughout chapter 3 indicate that it is possible to drastically enhance the number of ground state $\overline{\mathrm{H}}$ atoms (close to unity ground state fractions can be reached within a few tens of µs) right after their formation by stimulated deexcitation or stimulated radiative recombination. Due to the current non-availability of anti-atoms[1], an experimental demonstration of deexcitation on matter is a necessary intermediate step. From a technology development standpoint of view it is anyway desirable to commission the experimental techniques making use of atomic systems that are, compared to anti-atoms, relatively readily available. Therefore, hydrogen is the element of choice. In general however, other alcaline atoms like e.g. cesium are easy to produce and exhibit very similar Rydberg properties.

Section 4.1 is dedicated to a review of light sources that have the potential to efficiently mix and deexcite the initially populated $\overline{\mathrm{H}}$ Rydberg states. A state mixing proof-of-principle experiment reported in section 4.2 has been performed by collaborators at Laboratoire Aimé Cotton making use of an excited cesium beam. A proof-of-principle hydrogen beamline is introduced in section 4.3. Section 4.4.1 and 4.5 are dedicated to efforts toward the production of Rydberg hydrogen states.

[1] CERN's accelerator complex has been shut down during the second long shutdown (LS2).

4.1 Mixing and deexcitation light sources

The simulations presented throughout chapter 3 employed visible, THz and microwave light. Whereas powerful microwave sources are commercially available, the generation of intense THz light is a technological challenge where mW output power is roughly the bottleneck. Comprehensive reviews of THz technology exist [6, 88, 117–120] and will be put into context of antihydrogen state mixing and deexcitation in subsection 4.1.1 (broadband sources) and 4.1.2 (narrowband sources). It is important to recall that multiple frequencies must be produced simultaneously to avoid a mere population exchange between the atomic states at resonance. In the following, only fixed frequency light sources which output wavelengths do not vary as a function of time are discussed. For the THz deexcitation scheme (cf. Fig. 3.6) and $n = 30$ and $n' = 5$, the total (summed over all driven transitions) THz light intensity amounted to $> 10\,\mathrm{mW\,cm^{-2}}$ covering a frequency range from $\sim 200\,\mathrm{GHz}$ to well within the THz region (the frequencies range from over 40 THz for $n = 6 \to 5$ to 0.26 THz for $n = 30 \to 29$). Restricting the THz light to transitions with $25 \leq n \leq 30$ allowed to decrease the required light intensity by more than an order of magnitude to $1\,\mathrm{mW\,cm^{-2}}$ at the expanse of requiring a broadband deexcitation laser toward the $n'' = 3$ levels (cf. Fig. 3.7)

The development of a powerful (and especially broadband) visible 832 nm deexcitation laser is discussed in subsection 4.1.3.

4.1.1 Broadband THz sources

A single broadband THz source can be used to cover all transition frequencies required. Whereas the easy experimental implementation is clearly an advantage, a broadband source will, on the downside, emit plenty of off-resonance frequencies that will not drive the desired transitions. The source's output power at these wavelengths is consequently lost. Obviously, this statement mainly refers to the case where THz light is rather used to deexcite toward low n. For $n \to n - 1$ transitions with $n > 25$ the inter-n-manifold spacing is exceeded by the atomic level broadening in the external 1 T field and the desired THz spectrum is in fact, assuming one wishes to address states with $n \leq 30$, a continuum with frequencies $218\,\mathrm{GHz} \leq \nu \leq 475\,\mathrm{GHz}$ (cf. Fig. 3.5). In such a case a broadband source might

actually be the preferred solution. It has been shown that a uniform distribution of the output power toward all driven inter-n-manifold transitions is desirable to establish equal average $n \to n-1$ transition rates. Such a scaling seems to be rather difficult to implement with a broadband source.

Unfortunately, the costs of broadband light sources such as portable synchrotron [121] or table-top Free Electron Lasers [51, 122–124] are still prohibitive. Pulsed light sources like femtosecond mode-locked lasers can be used to generate light in the desired frequency range making use of, for example, photoconductive switches. For application to antihydrogen deexcitation fast repetition rates would be required to depopulate all initially populated levels. For such high duty cycles the optical-to-THz conversion efficiency drops to $\sim 10 \times 10^{-5}$ [6] rendering the devices unfit for the purpose. Nevertheless, Rydberg transfer of $n = 50$ levels in Rb down to $n \leq 40$ has been reported making use of narrowband half-cycle pulses [52] resulting in a radiative lifetime reduction by a factor 4 and a 2 % increase of ground state population. The achieved deexcitation efficiency, however, only amounted to 10 % and a strong coupling of the population to the continuum was observed. Related theoretical studies and experimental investigations of ionization of Rb atoms at similar wavelengths due to thermal radiation around 320 K can be found in [125, 126].

A rather straight forward solution employed in this work is a blackbody emitter. Such a radiation source emits, assuming a black body with a temperature of 1000 K, $\sim 4\,\mathrm{mW\,cm^{-2}}$ at frequencies between 0.1 and 0.5 THz and has already been proposed in [127] to cool internal degrees of freedom of MgH^+ molecular ions. The emitter employed to obtain results presented in this work is a ASB-IR-12K from Spectral Products. A picture is shown in Fig. 4.1.

4.1.2 Narrowband THz sources

Compared to broadband sources, narrowband ones only cover few or (ideally) a single $\Delta n = \pm 1$ transition. The main advantage is that the spectral width of each source can be adapted to match the field broadening of the manifold one wishes to address removing the drawback of lost output power in off-resonance frequencies. Additionally, several narrowband sources offer the possibility to implement a flat power scaling that has been identified as optimal for state mixing or deexcitation

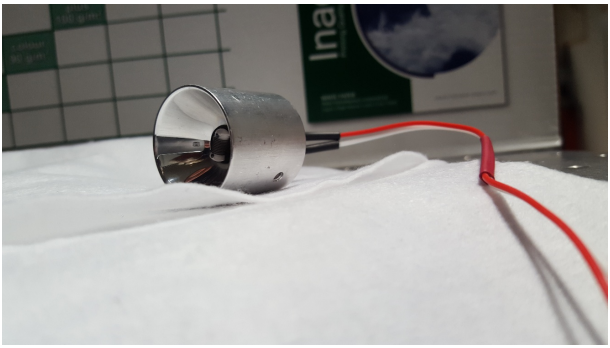

Figure 4.1: Spectral Products ASB-IR-12K mounted into a parabolic mirror to focus the emitted light into a beam. The lamp operates at 975 °C when powered with 11 W.

in the previous chapter. Depending on the exact deexcitation scheme, however, a multitude of sources might be necessary – up to 25 for the schemes investigated in this work.

Quantum cascade or molecular lasers are capable of producing the frequencies and desired light intensities necessary, but, given the number of frequencies to generate, costs are again a prohibitive factor. Especially in view of application to antihydrogen, where the initial state distribution is not well known experimentally, a certain versatility of the deexcitation light sources is a key advantage.

The use of photomixers might be an attractive solution offering maximal flexibility. Demonstrated THz output powers can reach the mW level [83]. As pointed out earlier, photomixing or optical heterodyne relies on the generation of a photocurrent in a semiconductive material that oscillates at $|\omega_1 - \omega_2|$, the beatnote of two input light sources with frequencies ω_1 and ω_2, respectively. The induced charge carriers then emit THz radiation via an antenna. Comprehensive theoretical considerations are laid down in [128] or above-cited references. The main findings and technology characteristics in view of application to antihydrogen deexcitation are summarized below.

- The THz output power P_{THz} can be expressed by

$$P_{\mathrm{THz}}(\omega) = \frac{J_0^2 R_A}{2\left[1+(\omega\tau_c)^2\right]\left[1+(\omega R_A C)^2\right]}, \tag{4.1}$$

  where $J_0 = G_0 V_b$ is the photocurrent, G_0 the DC conductance, V_b the bias voltage, R_A the antenna's radiation resistance, C the capacitance of the conductive gap, τ_c the carrier lifetime and ω the input frequency beatnote. For a frequency independent antenna resistance the carrier lifetime and the RC constant determine the power conversion behavior at high frequency, where, with $\omega\tau_c \gg 1$ and $\omega R_A C \gg 1$, P_{THz} reduces to $\frac{1}{2} J_0^2/\omega^4 R_A (\tau C)^2$. The photomixer maximal THz output power thus decreases by -12 dB per octave (or by a factor 8 for each doubling of the frequency).

- In contrast to nonlinear processes as, for example, in an optical crystal where the frequency conversion efficiency is limited by the photon frequency ratio (optical light at 800 nm (375 THz) can be converted to 1 THz photons with a maximum efficiency of 1/375) photomixers can exceed this Manley-Rowe limit since the energy converted into THz photons originates from the static electric field present within the semiconductor's gap region.

  The technological output power limit for photomixers is thermal failure of the semiconductor gap region amounting, for LT-GaAs devices, to roughly $10^5\,\mathrm{W\,cm^{-2}}$. For gap regions of the order of 100 µm, this limit then amounts to ~ 100 mW [128].

- The generation of multiple frequencies with a single photomixer can be achieved making use of, for example, multi-mode diode lasers [129]. For n_0 different input frequencies ν_i one pairwise generates $n_0(n_0-1)/2$ THz output wavelengths which is a very interesting use-case in view of antihydrogen deexcitation. Recalling again the required versatility it is noteworthy to mention that photomixers, simply reproducing the beating in the input laser spectrum, can as well be used as broadband sources.

4.1.3 Deexcitation laser

For both crossed external field and light stimulated Rydberg state mixing, a deexcitation laser is crucial to drive population toward low lying manifolds that rapidly decay spontaneously to the ground state. The laser specs and possible technological implementations for each case are discussed in the following.

Deexcitation relying on field mixing

Relying on state mixing via crossed electric and magnetic fields calls for broadband lasers that cover the entire spectral range of initial states addressed. The schemes investigated in chapter 3 require spectral widths ranging (in the 1 T and 280 V cm^{-1} at 160° relative angle configuration) from 565 GHz (addressing the $n = 20$ levels) to 1024 GHz (addressing the $n = 30$ levels). An even more extreme case, where the entire formed $\overline{\mathrm{H}}$ state distribution with $20 \leq n \leq 30$ is deexcited with a 5000 GHz broad laser is studied in [2, 3]. Generating light with intensities of several tens of GW m^{-2} to stimulate the $n = 30 \rightarrow 3$ transition at 828 nm (the field configuration has been optimized for mixing the $n = 30$ states) is a technological challenge.

A broadband pulsed laser with a pulse duration of the order of ~ 100 ns could be realized based on Q-switched Cr:LiSAF oscillators. Even though such pulses are insufficient to depopulate the entire $n = 30$ manifold toward ground state, such devices could provide interesting time of flight information and allow to probe population densities within a given n manifold (obviously here a very narrow initial spread in n has to be assumed which is, in principle, achievable relying on a CE reaction). First theoretical studies [130] showed that the required energy densities might be achievable relying on a single laser cavity. The required crystal size would, however, lead to comparatively high costs and operation close to the damaging threshold of the crystal which is not desirable. A setup encompassing two cavities (a separate oscillator and amplifier) might thus be the preferred solution. Working with longer (10 µs to 100 µs) laser pulses to deexcite more initial levels, as suggested by the simulations presented in this work, opens up the possibility to operate Cr:LiSAF lasers in relaxation mode (thus without a Q-switched cavity). The material can be pumped with flash lamps leading to pulse energies of the order of 1 J mm^{-2} for 100 µs. Diode pump lasers – the pump wavelength in such a case is 650 nm – are rather difficult to implement within this power regime. The

main drawback of such a solution are relaxation oscillations introduced by fast variations of the pumping power resulting in uncontrollable power peaks in the laser output. As an alternative to Cr:LiSAF based lasers, a stack of diodes can generate light with the specifications needed around $\sim 830\,\mathrm{nm}$ ($n = 30 \rightarrow n' = 3$). Here, the main challenge is indeed the focusing of the light onto the cloud of $\overline{\mathrm{H}}$ atoms emerging from the trap center. Similar technology with narrower bandwidth can be employed for deexcitation with light mixing as discussed below.

Deexcitation relying on light mixing

Referring back to Fig. 3.7f, which is the somewhat final result for a scheme incorporating THz and microwave state mixing, a laser intensity of $1 \times 10^7\,\mathrm{W\,m^{-2}}$ is required. The spectral bandwidth amounts to 500 MHz at a $n = 25 \rightarrow 3$ wavelength of 832 nm. Assuming a radial expansion of the $\overline{\mathrm{H}}$ cloud of the order of cm, the laser output power amounts to $\sim 1\,\mathrm{kW}$. Such specifications can be met by microchannel-cooled or quasi-continuous wave (QCW) diode laser stacks. Currently achievable single diode output powers lead to a system of ~ 12 diode elements. Off-the-shelf diodes are available with an emission wavelength of 825 nm that can be adjusted by $\sim 30\,\%$. The usual pulse duration of QCW systems of the order of ms can be reduced, to realize for example $\overline{\mathrm{H}}$ time-of-flight measurements, to some tens or hundreds of µs. The costs of such a custom made diode stack have been estimated to lie around ~ 50 kEUR [131]. It is noteworthy to point out that the possibility to develop a deexcitation laser suitable for both CE and 3BR in general exists. However, this heavily depends on the exact experimental conditions and, most importantly, the initial states to be addressed since this determines the required spectral width of the light.

4.2 Proof-of-principle state mixing in a beam of cesium atoms

Alkaline atoms such as cesium in highly excited states exhibit properties close to those of Rydberg hydrogen. At the same time, beam production of cesium atoms is a common technology and light sources to excite the atoms in a beam to Rydberg

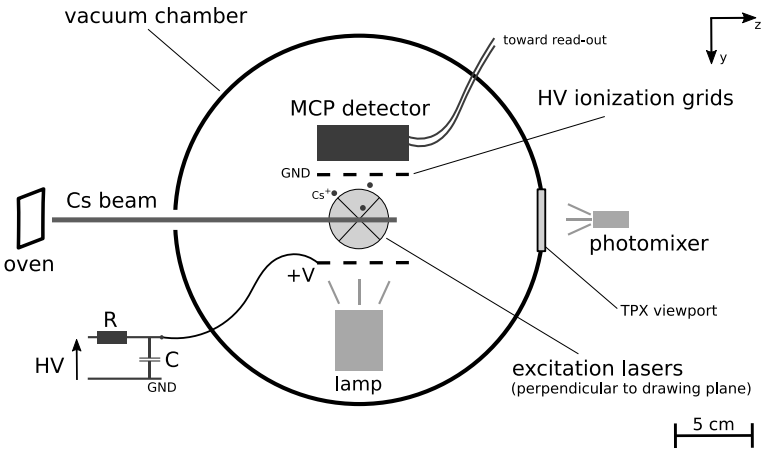

Figure 4.2: Illustration of the cesium beam line. Reprinted from [6].

states readily exist off-the-shelf. As will be shown in section 4.3 this is not the case for hydrogen. Thus, a technology demonstration of Rydberg state mixing has been carried out in the first place relying on a cesium beam [6].

The experimental setup used to asses the efficiency of the narrow and broadband mixing light sources discussed in section 4.1 is illustrated in Fig. 4.2. The atomic cesium beam is emitted out of an oven and enters a vacuum chamber. The atoms are excited from the $6s_{1/2}$ to the $6p_{3/2}$ level relying on a cw diode laser at 852 nm. A second pulsed laser (OPO pumped by a Nd:YAG) then populates the nS or nD Rydberg level. The chamber is equipped with two high voltage grids and a set of mirco-channel plates (MCP) in chevron configuration [132, 133] perpendicular to the beam direction. This particle detector is used to probe the electric field ionization products and therefore the cesium quantum state distribution in the beam. Making use of a simple RC circuit, a high voltage pulse with a characteristic rise time of 4 µs is applied to the lower one of the field ionizer (FI) grids. Since each atomic state ionizes at a characteristic electric field strength, the cesium ions detected by the MCP allow to draw conclusions on the population density of the atomic levels within the beam. The high voltage pulse is triggered with a delay t_D with respect to the pulsed deexcitation laser.

The results obtained when driving the 97 GHz transition from the $36s_{1/2}$ level to the $36p_{3/2}$ state are shown in Fig. 4.3. A GaAs Toptica photomixer was used to generate a THz output power of $\sim 1\,\mu W$ relying on near 852 nm laser lines from a Ti:Sa and a diode laser. The photomixer output spectral width as reproduced from the input lasers was < 5 MHz. As illustrated in Fig. 4.2, the light was sent through a THz transparent viewport and illuminated the atomic sample along the beam axis for $\sim 10\,\mu s$. The population transfer induced by the photomixer is clearly visible in Fig. 4.3. Integrating the signal leads to a measured population transfer of $\sim 15\,\%$ that is significantly lower than expected. Indeed, theoretical considerations lead to a transition rate of $\sim 10^8\,s^{-1}$ (the transition dipole from the $36s_{1/2}$ to $36p_{3/2}$ level is $554\,e\,a_0$ [134]) whereas the measured one only amounts to $10^4\,s^{-1}$. This discrepancy is mainly explained by atomic level broadening due to significant field inhomogeneities introduced by the MCP fringe field along the beam path. Simulations showed that such parasitic fields can be of the order of tens of $V\,cm^{-1}$ broadening the levels addressed by the photomixer by several tens of GHz and thus rendering the population transfer inefficient.

Figure 4.4 illustrates the reduction of the $40d_{5/2}$ lifetime introduced by the broadband lamp shown in Fig. 4.1 (ASB-IR-12K). The filament is mounted into a parabolic mirror inside the chamber in direct proximity to the cesium beam. In contrast to the time of flight measurement presented in Fig. 4.3, here t_D was varied. For each delay time, the signal was integrated around the mean arrival time of the field ionization pulse over 200 ns. It is important to note that especially the signal with the lamp being switched off is non-exponential which can be explained by the ionization signal of neighboring states contributing to the integrated lifetime measurement. It is apparent that the lamp introduces a lifetime reduction of the $40d_{5/2}$ level from 11 µs to roughly 3.5 µs (when indicating the typical $1/e$ depopulation time). At the same time, parasitic ionization and excitation was found to lie close to 50 % [76]. The measurement is consistent with simulation data obtained for a 1100 K black body spectrum which is even slightly higher than the nominal lamp temperature. Here, similar to the studies presented in chapter 3, a set of rate equations was solved under the assumption of non-coherent light sources operating in the low saturation limit. In such conditions this is valid and preferable over treating the full optical Bloch equations. The resulting equation system is solved numerically for a few hundred atoms using code developed by D. Comparat and presented in [70].

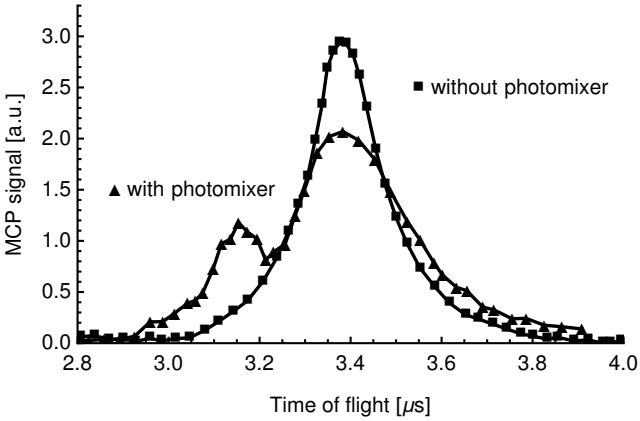

Figure 4.3: Time of flight measurement of the cesium ions with respect to the high voltage ramp applied to the field ionizer grids. The signal is plotted for the photomixer being switched off (square markers) and on (triangle markers). In the first case, the ionization signal of the $36s_{1/2}$ level peaks around 3.4 µs. The ions originating from population transferred toward the $36p_{3/2}$ level arrive roughly 250 ns earlier and result in a second peak at 3.4 µs when the photomixer is switched on. Reprinted from [6].

The results presented can be seen as a technology proof-of-principle. The capabilities of narrow- and broadband sources to stimulate Rydberg transitions for state mixing have been demonstrated on a beam of cesium atoms with direct implications for the antihydrogen case. The photomixer was used to generate near THz frequencies of ~ 0.1 THz which lies within the range of wavelengths required for the antihydrogen case. The effects of fringe fields resulting in a rather inefficient transfer of only 15 % need to be carefully assessed in the case of (anti-)hydrogen deexcitation. It is, however, important to note that light sources for $\overline{\mathrm{H}}$ deexcitation are comparatively broadband[2] and field effects in typical experimental conditions have been carefully calculated in chapter 3.

A deexcitation of the $40\mathrm{d}_{5/2}$ level was realized relying on a broadband IR emitter. As expected, such a broad spectrum of frequencies results in significant losses through ionization and excitation processes that are particular harmful in a $\overline{\mathrm{H}}$ application where anti-atoms are extremely scarce. In principle undesired frequency ranges (low ones to drive $n \to n-1$ transitions that have an increased potential to directly connect the population to the continuum as well as high ones that drive high $n \to n+1$ transitions that can likewise culminate in ionization) can be cut out with optical filters. Efficient techniques of THz transport have been identified in [76]: A simple metallic (copper) pipe of roughly 30 cm length (diameter ~ 1 cm) was able to transmit ≥ 94.5 % of the lamp's output power. The installation of a high temperature lamp in a cryogenic $\overline{\mathrm{H}}$ setup, however, remains somewhat hypothetical. The total output power of the used infrared emitter amounts to 11 W and the heating element operates at a temperature of 975 °C.

4.3 Proof-of-principle Rydberg hydrogen beamline

In order to assess the experimental implementation and effectiveness of the deexcitation methods theoretically investigated in chapter 3, an atomic hydrogen Rydberg beamline has been set up. This is the next consequent step to validate the cesium proof-of-principle experiment (cf. section 4.2) and test, in addition to Rydberg state mixing, the deexcitation laser discussed in subsection 4.1.3 on hydrogen before

[2] Even light sources referred to as narrowband have bandwidths of at least a few hundred MHz. Typical mixing of high n states, where fringe field effects would be highest, requires spectral widths of the order of GHz.

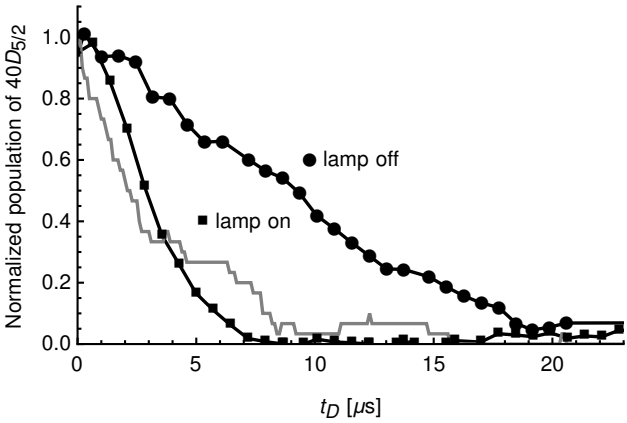

Figure 4.4: Lifetime reduction of the 40d$_{5/2}$ level in cesium using a broadband IR lamp. As mentioned in the text, t_D indicates the delay of the high voltage ramp applied to the field ionizer grids with resepect to the laser excitation pulse toward the given Rydberg state. The gray graph depicts simulation data for a 1100 K blackbody spectrum. Reprinted from [6].

an application within the $\overline{\text{H}}$ experiments at the AD. A new hydrogen beamline employing a plasma source is presented in subsection 4.3.1. The main working principles of atomic hydrogen plasma sources and data from commissioning an Evenson cavity are laid down in subsection 4.3.2.

4.3.1 Hydrogen beamline

A new Rydberg hydrogen beamline has been conceptualized, built and commissioned throughout the work presented in this thesis. Ultra-pure gas of molecular hydrogen is provided by an electrolysis generator dissociating deionized water into H_2 and O. Downstream the generator, a pressure reducer limits the gas flow in such a way that the generator's gas supply is sufficiently high to gradually fill up a $\sim 1\,\text{l}$ reservoir to above-atmospheric pressures to avoid potential inflow of ambient gases leading to contamination in the system. A flowmeter controls the amount of gas entering into a cylindrical 13 mm diameter quartz tube enclosed in an Evenson cavity (cf. subsection 4.3.2) driving a H_2 dissociation plasma within pressure regimes from 1 to 0.1 mbar. The cavity and glass tube are both cooled by convection of compressed air. A spectrometer is mounted in line-of-sight of the plasma to detect the visible emission spectrum. Hydrogen molecules are dissociated mainly through electron collisions within the discharge plasma. Thermal hydrogen atoms emerge from the plasma region and are emitted into the downstream vacuum region via a 0.5 mm circular aperture mounted into a KF-sealing ring. A first KF160 chamber (operated at pressures $\sim 10^{-5}$ mbar) hosts a two-stage aluminum thermal beam shield which is cooled by compressed helium and a cold finger to temperatures of 100 K (first stage) and 35 K (second stage). The shielding prevents thermal radiation from acting upon the quantum state distribution within the beam. Perpendicular laser access to excite the atomic beam is foreseen via quartz viewports and according openings in the cryogenic beam shield (cf. section 4.5). The laser beam is guided through the chamber, perpendicular to the atomic beam direction, toward a second viewport where the light can be dumped outside to minimize parasitic heating of the cryogenic beam shield. A second CF160 chamber (operated at pressures $\sim 10^{-6}$ mbar) is mounted further down the atoms' flight path where a set of electric field ionizer meshes and two micro-channel plate (MCP) chevron stacks are installed parallel to the beam propagation direction. Differential pumping between the two chambers is optimized by customized blank

copper gaskets sparing only the cross section of the beam shielding. Ionization products are detected as a function of the electric field ionization strength to probe the quantum state distribution within the beam. An oscilloscope is capacitively coupled to the floating anode of the MCP stack (the potential drop over the stack is $\sim 2\,\mathrm{kV}$ for charge amplification factors of the order of 10^7). The coupling capacitor is 20 nF. The anode and oscilloscope are both grounded via $1\,\mathrm{M\Omega}$ and $50\,\Omega$ resistors respectively. Finally, two diodes with a breakthrough voltage of 0.7 V prevent damaging the oscilloscope. The scope generates a short trigger for MCP pulses over a certain threshold ($\sim 18\,\mathrm{mV}$). This signal is then shaped to pulse widths of a few µs with a signal generator to facilitate its detection with low sample rates. Triggers are accumulated, for each data point over typically 10 s, relying on a NI USB-6009 DAQ card operated via LabView. Depending on the mode of operation, the MCP front/back/anode voltages are either $-2\,\mathrm{kV}/0/50\,\mathrm{V}$ for proton or $0/2\,\mathrm{kV}/2.05\,\mathrm{kV}$ for electron detection. The polarity of the field ionization plates is always chosen such that positive or negative charged particles are accelerated toward the respective MCP. For more elaborate schemes, both the MCP voltages and/or field ionizing potential could be pulsed with a high voltage solid state switch. This might be of particular interest when suffering from high background which could be, for example, introduced by UV photons impinging on the MCP in the case of Rydberg laser excitation (cf. section 4.1.3) or other processes. Finally, radiation for Rydberg state mixing, deexcitation and/or beam velocity Doppler measurements can be introduced through (different) viewports at the rear end of the beamline. A sketch as well as a photo of the setup is shown in Fig. 4.5.

4.3.2 Atomic hydrogen production with discharge sources

Plasmas are research topic in a variety of different fields ranging from astrophysics[3], space propulsion and fusion research to industrial semiconductor processing, cutting or lighting. A very instructive review of the physics of plasma sources used to generate such ionized gases in the laboratory can be found in [135]. In the presently treated case, weakly ionized plasmas are used to dissociate H_2 gas, produced by electrolysis of H_2O, into atomic hydrogen.

[3] By far most of the visible matter in the Universe is found to be in the condition of a plasma: in the core of stars at very high pressures and temperatures as well as within the interstellar medium at low pressures and temperatures.

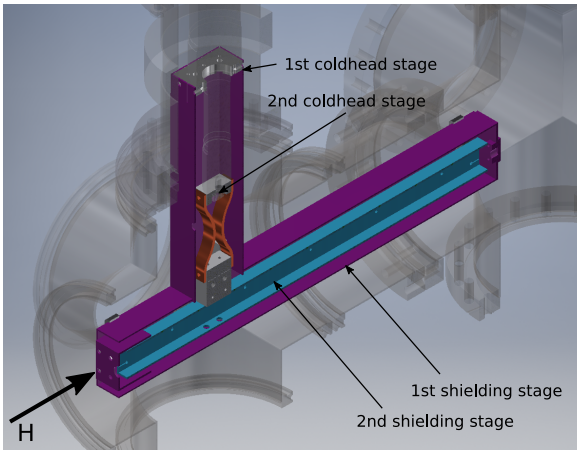

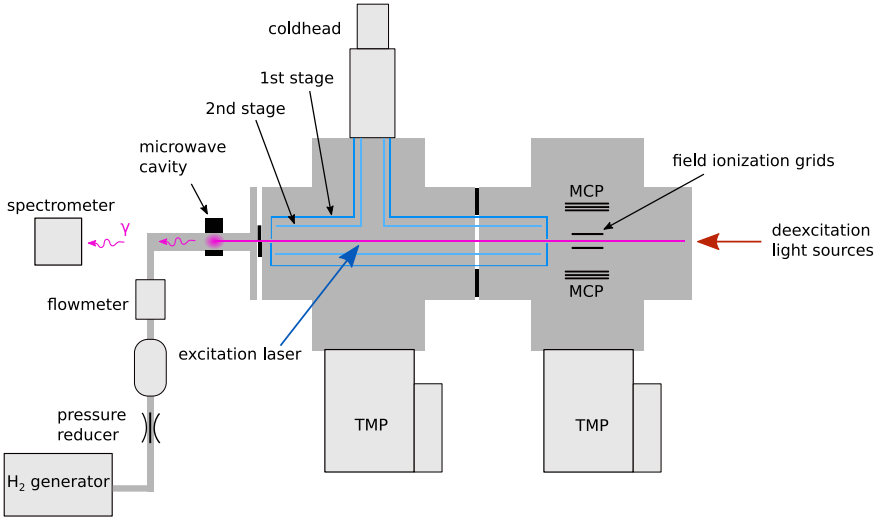

(a) CAD drawing and sketch of the Rydberg beamline.

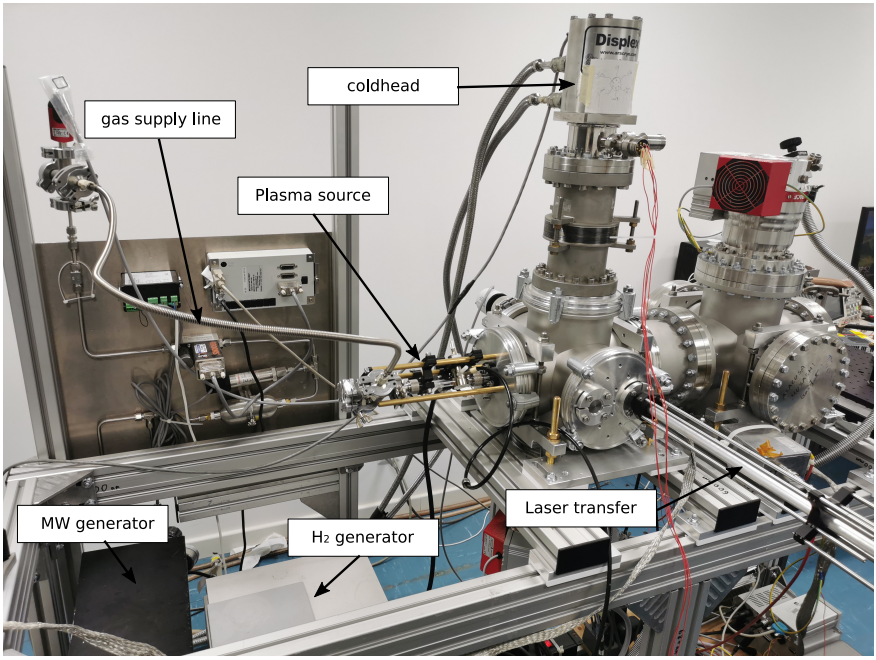

(b) Photo of the Rydberg beamline.

Figure 4.5: CAD drawing and sketch (a) as well as a photo (b) of the atomic Rydberg beamline for a hydrogen proof-of-principle deexcitation experiment.

In general, a plasma contains freely moving charged particles (in the given case primarily protons and electrons) that efficiently couple to external fields. At sufficiently high field oscillation frequencies in the radio-frequency range the gas behaves like a dielectric medium rather than a DC conductor in the case of quasi time-invariant externally applied fields. Consequently, a cavity or antenna enclosing a sealed or flowing gas cell allows to sustain a certain degree of ionization within the probe gas driven by fields that oscillate in the radio-frequency range at typically 2.45 GHz. The H_2 dissociation processes at play have been investigated and are listed in Table 1 of [136]. Formation of atomic hydrogen through the process

$$H_2 + e^- \rightarrow H^+ + H + 2e^-$$

can be neglected due to the high energy onset $E = 18\,\mathrm{eV}$ and small cross section $\sigma = 5 \times 10^{-19}\mathrm{cm}^2$. The reactions

$$\begin{aligned} H_2^+ + e^- &\rightarrow H + H^+ + e^-,\ E = 12.4\,\mathrm{eV},\ \sigma = 3 \text{ to } 16 \times 10^{-16}\,\mathrm{cm}^2 \\ H_2^+ + e^- &\rightarrow H + H,\ E = 0\,\mathrm{eV},\ \sigma \sim 100 \times 10^{-16}\,\mathrm{cm}^2 \\ H_2 + e^- &\rightarrow H + H + e^-,\ E = 8.5\,\mathrm{eV},\ \sigma = 0.6 \times 10^{-16}\,\mathrm{cm}^2 \end{aligned} \tag{4.2}$$

exhibit lower onset energies and much higher cross sections. The density of molecular ions, however, can be considered much smaller than the H_2 concentration [136, 137]. Thus, one can expect that the atomic hydrogen formation is dominated by electron impact dissociation. This reaction, the last line of Eq. 4.2, exhibits an energy onset of 8.5 eV and a cross section of $0.6 \times 10^{-16}\,\mathrm{cm}^2$.

A multitude of discharge source designs was proposed by Evenson et al in [138]. The most efficient and easiest-to-operate concept (design 5 in the above reference) consists of a compact radio-frequency cavity that is employed throughout the studies presented in this work. Fig. 4.6 shows the source in operation as well as technical drawings of the cavity. A threaded tuning stub which can be screwed from the top down into the cavity and a teflon coupling slider that is mounted perpendicular on the axis of the N-type microwave input connector allow to tune the cavity in operation and consequently remove the necessity of external impedance matching (as can be required for other designs [139, 140]). A removable cap on the bottom side enables easy installation also on existing setups without the need to break the vacuum. The cavity and, most importantly, the glass encapsulating the plasma region is cooled by a flow of compressed air. Generally, quartz glassware is

the preferred solution over pyrex due to heat resistance and purity. Indeed, pyrex additives such as B, Na, Al and O allow ample opportunity for undesired chemical reactions that can be partly triggered by hydrogen ions which are driven into the glass by the plasma sheath field [141]. These processes have been observed to quickly deteriorate the glass (after a few hours of operation) and lead to a contamination that has the potential to disturb the discharge.

Principal operational parameters such as plasma pressure and forwarded microwave power have been systematically studied. For this purpose, the atomic ground state rate emitted from the plasma is measured with a quadrupole mass spectrometer (QMS) at the ASACUSA hydrogen beam[4]. This beamline [142] has been developed to commission ASACUSA antihydrogen spectroscopy methods and is currently used (in a modified version) to test Lorentz invariance with hydrogen [143]. The results are shown in Fig. 4.7. Within a pressure range reaching from 0.24 mbar to 1.12 mbar the background subtracted atomic hydrogen count rate is measured as a function of the forwarded microwave power. While precisely controlling the forwarded power, the cavity is tuned such that less than 5 % of the forwarded power is reflected. The data reveals different critical plasma cut-off powers, i.e. the lowest power where the plasma can be sustained in a stable manner without potential occurrences of cut-offs, that reach up to 25 W for 0.24 mbar. Close to the cut-off, plasma instabilities manifest themselves in significantly larger errors compared to higher power settings at same pressure. Except at the region around the cut-off, the detected rate is rather insensitive to varying forwarded power. Pressures ~ 4 times higher than the minimal setting, however, lead to a more than two fold increase in count rate at the mass spectrometer to absolute values of around 6.5 kHz. Maximal rates are obtained at rather high pressure around 1 mbar which will consequently be the operating regime in the following studies presented throughout section 4.4.2. It is nevertheless noteworthy to point out that the mentioned 4-fold increase in pressure to obtain maximal rates, corresponds to a ~ 5-fold increase in required gas flow. Thus, cracking efficiencies are actually highest at low plasma pressures.

Whereas measured rates are of the order of $10^3\,\mathrm{s}^{-1}$, atomic production within the plasma is much higher (this is mainly due to the solid angle coverage of the

[4] In contrast to the novel Rydberg beamline presented in subsection 4.3.1, where excited quantum states can be detected via electric field ionization, here a measurement of the ground state emittance is possible which offers the possibility to directly study the H_2 cracking efficiency of the source.

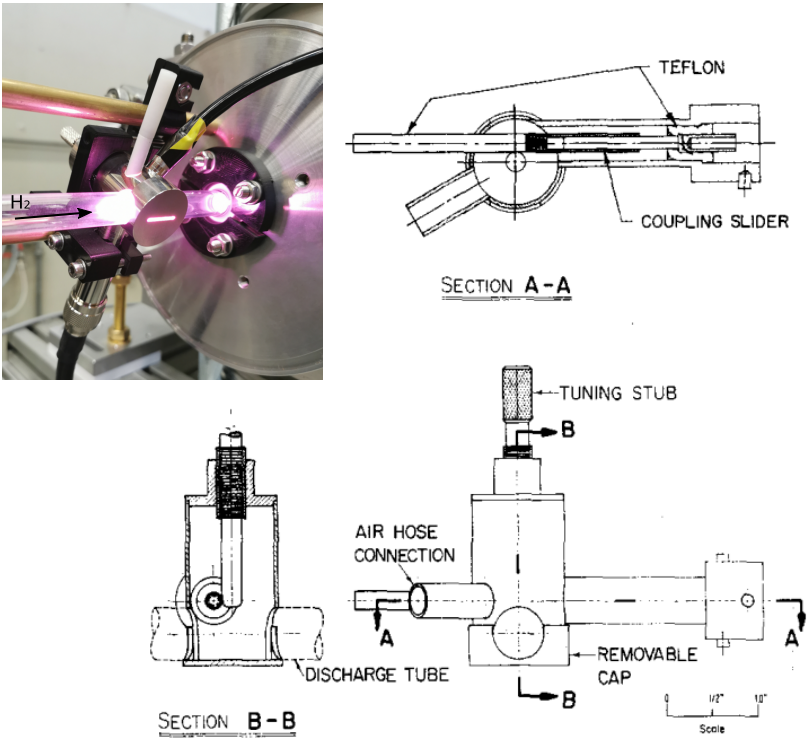

Figure 4.6: Evenson cavity with burning plasma (top left photo). The compressed air for cooling is supplied from the top right corner of the picture and the coaxial N-type connector to couple in the microwaves is shown on the bottom left part. The gas flows from the left to the right where an aperture is manufactured into a KF16 centered O-ring that is pressed onto a KF vacuum flange. The technical drawings are reprinted from [138].

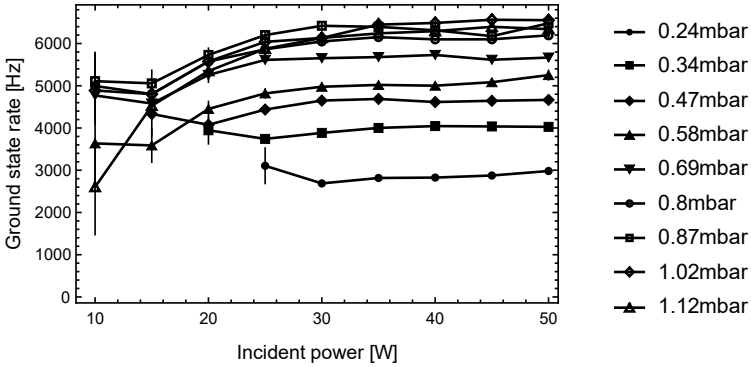

Figure 4.7: Evenson cavity ground state hydrogen production rate as measured with a mass spectrometer. The vertical error bars indicate the standard deviation of the four acquired data sets. The lines are to guide the eye.

detector at the end of the beamline, detection efficiency, de-focusing of high-field seeking atoms with sextupole magnets required for spectroscopy measurements, potential recombination within a PTFE tube used to cool the beam to 50 K, velocity selection along the beam path, etc. For details, please refer to [142]). In principle, molecular hydrogen flows of 1 $cm^3\,min^{-1}$ at standard conditions (101.325 kPa and 273.15 K) correspond, to $7.44 \times 10^{-10}\,mol\,s^{-1}$. Assuming a plasma dissociation efficiency of 100 %, this leads to an atomic hydrogen rate produced by the source of roughly $10^{18}\,s^{-1}$.

4.4 Rydberg hydrogen beam production in a discharge plasma

In order to study mixing and deexcitation light sources on Rydberg levels in hydrogen, an excited beam must be produced in the first place. In this thesis two different approaches are investigated. Simulations suggest that a broad distribution

of Rydberg states can be formed through collisional and recombination processes (that are indeed similar to $\overline{\mathrm{H}}$ 3BR production) inside a discharge plasma. This scheme will be subject of subsection 4.4.1 and 4.4.2. Another possibility lies in laser excitation toward targeted (ideally circular) Rydberg quantum levels. A dedicated discussion can be found in subsection 4.5. The pros and cons of either method will be highlighted.

4.4.1 Processes involved

Collisional processes that take place in high frequency microwave discharge plasmas have been thoroughly studied in the context of ion production. It was found that the generation of protons (which is the main emission product one aims for in, for example, fusion experiments) is dominated by a two-stage process comprising an electron collisional dissociation of H_2 into H (as discussed in subsection 4.3.2 in view of atomic hydrogen production) followed by electron impact ionization [144]. Apart from ionization of the produced H atoms through electrons, there are similar processes which, in principle, allow for the formation of atomic hydrogen Rydberg states within such a plasma. The resulting distribution of highly excited levels is of interest for the experimental tests of deexcitation developed throughout this work.

In order to accurately describe the excitation and deexcitation reactions inside the plasma, different population models have been established. Corona models restrain themselves to solely electron collisional excitation from the ground state and deexcitation via radiative spontaneous emission. This can be justified at low electron plasma densities $n_e \leq 10^{17}\,\mathrm{m}^{-3}$. Within the corona regime, the population coefficient for an excited state p, $R_{0p} = n_p/\left(n_e n_0\right)$ with n_0 denoting the ground state density, is constant as a function of the electron density n_e. Consequently, the population density n_p increases linearly with n_e. For intermediate electron densities $10^{17}\,\mathrm{m}^{-3} \leq n_e \leq 10^{22}\,\mathrm{m}^{-3}$ collisional deexcitation processes start to act upon the states' population densities (beforehand the decay was assumed to be dominated by radiative spontaneous emission). This effect is predominantly (and earliest) visible for highly excited states where the energy spacing of consecutive n-manifolds is small and radiative lifetimes are long. Within this regime, collisional radiative (CR) models are applied. For $n_e \geq 10^{22}\,\mathrm{m}^{-3}$ electron collisions lead to a local thermal equilibrium (LTE), the states thermalize and their population density follows a local Boltzmann distribution function. The transition between these

models depends, in addition to n_e, on the electron temperature T_e. Collisions start to act upon the states earlier for increased temperatures of the respective reactants. A quite comprehensive review is available in [145] (cf. Fig. 3.5 therein).

The plasmas dealt with in the presently treated work exhibit electron densities between $1 \times 10^{14}\,\mathrm{m}^{-3}$ and $1 \times 10^{15}\,\mathrm{m}^{-3}$ [146] which is mainly determined by the discharge geometry and pressure [135]. Precise measurements of n_e relying on, for example, Stark broadening of the spectral emission lines [147] become only feasible at much higher electron densities. Yacora on the Web [112] provides easy access to a CR model[5] based on the flexible solver Yacora. In addition to electron collisional excitation and deexcitation, the coupling of other ion species to the hydrogen population coefficients of excited levels can be studied. Available channels are direct excitation, dissociative excitation, two and three body recombination of H^+, dissociative recombination of H^+, dissociative recombination of H_3^+ and the mutual neutralization of H^- with positive ions. The reactions are listed in detail in Table 4.1. References for the implemented reaction cross sections etc. can be found in [148].

Electron temperatures can be determined by a comparison of the plasma spectral line emission intensities (line ratio method). Relying on the visible Balmer series, an easy-to-detect line ratio can be written as

$$\frac{\mathrm{H}_\alpha}{\mathrm{H}_\beta} = \frac{n_3 A_{3,2}}{n_4 A_{4,2}},$$

where $A_{n,n'}$ denotes the commonly used Einstein coefficient. It should be noted, that the same methodology can be applied to different atomic transitions as well. Yacora on the Web allows to output the n_3 and n_4 population densities that can be matched to line ratios experimentally observed using a spectrometer (QE65000 from Ocean Optics; resolution of $\sim 0.8\,\mathrm{nm}$ for wavelengths between 200 and 1000 nm) viewing the plasma sustained by the Evenson cavity.

Referring to Fig. 3.3 (a) in [145], T_e can be expected to lie around 1 eV for H-α/H-β ratios close to 10 and electron densities around $10^{15}\,\mathrm{m}^{-3}$. For rather low electron densities, the peak ratio is found to be insensitive to n_e and one can safely extrapolate the data to presently treated values around $10^{14}\,\mathrm{m}^{-3}$. For electron temperatures < 1 eV H-α/H-β rapidly increases. In reference [145], only the direct

[5] It is, of course, valid to employ a comparatively sophisticated CR model within the corona regime.

#	Process	Reaction
1	Excitation by electron collision	$\mathrm{H}(n) + \mathrm{e}^- \rightarrow \mathrm{H}(n' > n) + \mathrm{e}^-$
2	Deexcitation by electron collision	$\mathrm{H}(n) + \mathrm{e}^- \rightarrow \mathrm{H}(n' < n) + \mathrm{e}^-$
3	Spontaneous emission	$\mathrm{H}(n) \rightarrow \mathrm{H}(n' < n) + h\nu$
4	Ionization	$\mathrm{H}(n) + \mathrm{e}^- \rightarrow \mathrm{H}^+\mathrm{e}^-$
5	Recombination of H^+	$\mathrm{H}^+ + \mathrm{e}^- \rightarrow \mathrm{H}(n') + h\nu$
		$\mathrm{H}^+ + 2\mathrm{e}^- \rightarrow \mathrm{H}(n') + \mathrm{e}^-$
6	Dissociation of H_2	$\mathrm{H}_2 + \mathrm{e}^- \rightarrow \mathrm{H}(n') + \mathrm{H}(1) + e^-$
7	Dissociation of H_2^+	$\mathrm{H}_2^+ + \mathrm{e}^- \rightarrow \mathrm{H}(n') + \mathrm{H}^+ + e^-$
8	Dissociative recombination of H_2^+	$\mathrm{H}_2^+ + \mathrm{e}^- \rightarrow \mathrm{H}(n') + \mathrm{H}(1)$
9	Dissociative recombination of H_3^+	$\mathrm{H}_3^+ + \mathrm{e}^- \rightarrow \mathrm{H}(n') + \mathrm{H}_2$
10	Mutual neutralization	$\mathrm{H}^+ + \mathrm{H}^- \rightarrow \mathrm{H}(n') + \mathrm{H}$
		$\mathrm{H}_2^+ + \mathrm{H}^- \rightarrow \mathrm{H}(n') + \mathrm{H}_2$

Table 4.1: Plasma processes as implemented into Yacora on the Web. Adapted from [148].

electron collision channel is simulated and it turns out difficult to additionally consider other processes due to the lack of knowledge of the respective ion (H^+, H_2^+ and H_3^+) densities. This is of particular importance when anticipating that the electron temperatures found for the Evenson cavity discharge clearly point toward a so-called recombining plasma regime where processes other than electron collisions become increasingly important. One can however argue, that recombining channels will first act upon the population densities of highly excited states while for n_3 and n_4 the most prominent population mechanism is still electron impact. Finally, in [145] hydrogen temperatures of 0.8 eV are assumed, but cross-checks have shown that the hydrogen gas temperature has little impact on the results due to the large mass compared to electrons. The same argument applies to H^-, H^+, H_2^+ and H_3^+ ion temperatures. In summary, the considerations provide at best a rough estimate of T_e and results should be handled critically.

Scanning different plasma pressures and incident microwave powers with the Evenson cavity, line ratios between 10 and 16 have been measured experimentally [149] throughout the parameter range scanned in Fig. 4.7. Such ratios correspond to electron temperatures around 1 eV for low pressure and high power settings and

T_e of roughly 0.5 eV at intermediate power and high pressure. As already pointed out, the plasma is found to clearly be in a recombining regime and extrapolating the referred theoretical plots, where such channels are neglected, becomes increasingly difficult.

Instead of relying only on the emission spectrum of a single atomic species one can also consider mixing additional probe gases to the discharge to observe atomic spectral lines with different collisional onset energies [147]. However, this requires care to accurately control the gas densities which have a direct impact on the emission intensity of the respective spectral line. Still, the use of multiple gases does not address the mentioned lack of input data into models like Yacora on the Web to improve the theoretical result the experiment needs to be compared to. Ultimately, exact measurements that as well allow to probe different spatial regions of the plasma including, for example, its sheath region, can be obtained with Langmuir probes. In a Langmuir probe experiment the current drawn by a biased electrode inside the plasma region is measured as a function of the bias voltage. The resulting graph then allows to extract plasma parameters such as electron and ion density, the electron temperature as well as their velocity distribution. Further information can be found in [147]. In the presently treated case, such a probe electrode could be mounted to a standard KF16 flange (that would replace the spectrometer viewport shown in Fig. 4.5) so that it projects downstream along the quartz tube encasing the plasma.

Having approximately pinned down the plasma parameters n_e and T_e now allows to theoretically investigate Rydberg state production. Fig. 4.8 shows $R_{0,20}$, the population coefficient of the $n = 20$ manifold, for electron densities of $1 \times 10^{14}\,\mathrm{m}^{-3}$ and $1 \times 10^{15}\,\mathrm{m}^{-3}$ as a function of T_e. It is noteworthy to mention that the maximum manifold accessible with Yacora on the Web is $n = 20$. The minimum electron temperature is 1 eV. The contributions of the different population channels are normalized (in other words: ion density factors of 1 have been assumed). In line with results found in [145] and previous considerations, dissociative $\mathrm{H}^- + \mathrm{H}_2^+$ (#10 in Table 4.1) and recombination H_2^+ channels (#8 in Table 4.1) dominate by orders of magnitude over others, including the electron excitation channel. The summed population coefficients are found to lie around $10^{-21}\,\mathrm{m}^3$ for both electron temperatures considered. The main contributing channels are insensitive to the electron temperature within the considered regime which can be seen as a further argument why approximate knowledge of this plasma parameter can be sufficient.

In summary, the results point toward a Rydberg state production within a discharge plasma in the given experimental conditions. In a purely recombining corona regime, the population coefficient for highly excited states is not expected to largely vary as a function of n. Further argumentation regarding the dependence of n_p on n includes a discussion on which population channels can be assumed to be dominant over others. Additional considerations are provided in subsection 4.4.2.

4.4.2 Detection and interpretation

In order to discuss the experimental data on Rydberg state production within a microwave discharge plasma, the necessary theory of electric field ionization is laid down first below.

Electric field ionization of (anti-)hydrogen atoms

Hydrogen Rydberg states produced within the discharge plasma are detected in the following relying on electric field ionization. The proton count-rate originating from ionization processes in the detection chamber is recorded with a MCP at varying electric field strengths between the field ionizer meshes. In order to allocate the acquired signal to the respective hydrogenic quantum states, a connection between the ionization field strength and the probed quantum state distribution needs to be established.

Field ionization, is a common technique to detect Rydberg quantum states in alkaline Rydberg atoms (cf. section 4.2). In a classical picture, one can consider, for $m = 0$ states, a combined atomic Coulomb and external Stark potential $V = -1/r + Fz$, where F denotes the ionizing electric field strength, z the quantization axis and r the electron orbital radius. This leads to a potential saddle point at $z = -1/\sqrt{F}$ where V amounts to $-2\sqrt{F}$. Thus, for a binding energy E, classical ionization occurs at a field $F = \frac{E^2}{4}$ [82]. Expressing the binding energy in terms of n, leads to

$$F = \frac{1}{16n^4} \tag{4.3}$$

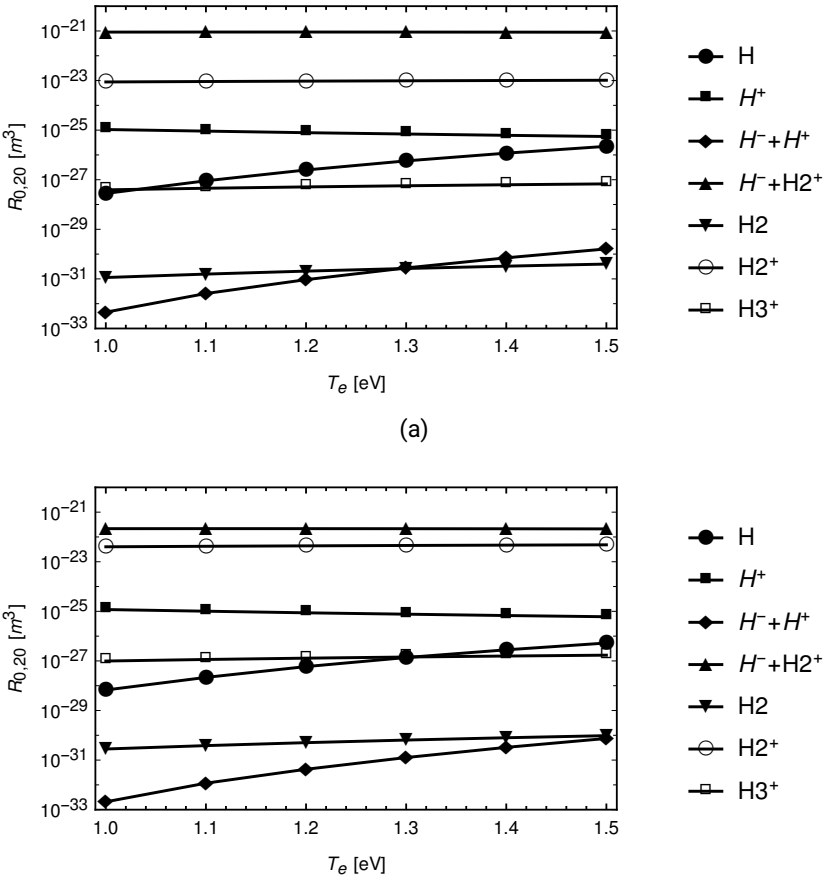

Figure 4.8: Population coefficient of the $n = 20$ manifold for different reaction channels (cf. Table 4.1) in hydrogen as a function of the electron temperature T_e and for electron densities of 1×10^{14} m^{-3} (a) and 1×10^{15} m^{-3} (b). The indicated lines are to guide the eye. The simulations have been performed with Yacora on the Web [112].

The considerations leading to Eq. 4.3 do not take into account the levels' Stark shift, the spatial distribution of their wavefunctions and the electron's centrifugal potential (as indicated, the formulas are valid only for $m = 0$ states).

In an external electric field, the electron wavefunctions of hydrogenic states that are shifted to lower energy (red states) lead to a charge distribution maximum in proximity to the Coulomb-Stark potential saddle point. In contrast, the charge distribution for states shifted to higher energies (blue states) exhibits a minimum and therefore leads to an increased electric field ionization strength. For illustration, the charge distributions of some states are plotted in Fig. 6.1 of [82]. A better approximation of the field required to start the ionization of a given n-manifold (beginning with the red states) can be found by including the Stark shift (still for $m = 0$ states) to the binding energy. This leads to $E = \frac{1}{2n^2} - \frac{3n^2F}{2}$ and ultimately

$$F = \frac{1}{9n^4}. \tag{4.4}$$

More sophisticated quantum calculations include tunneling of the electron at energies below the classical limit and rely on higher order perturbation theoretical approaches to determine the electron binding energy of (n, n_1, n_2, m) states where $n_2 = n - n_1 - |m| - 1$. Indeed, the ionization rate $\Gamma\,(n, n_1, n_2, m)$ for an electric field F is given by [150]

$$\begin{aligned}\Gamma =& \frac{(4R)^{2n_2+m+1}\, e^{-2R/3}}{n^3 n_2!\,(n_2+m)!} \times \\ & \times \exp\left[-n^3\frac{F}{4}\left(34n_2^2 + 34n_2m + 46n_2 + 7m^2 + 23m + \frac{53}{3}\right)\right],\end{aligned} \tag{4.5}$$

where $R = (-2E)^{3/2}/F$. Fourth order perturbation theory calculations of E can be found in [151] and lead to[6]

[6] One should note that a different formula for the binding energy is given in [152]. The equation differs in the sign of the first and third order term as well as a $3093\,(n_1 - n_2)^4$ instead of a $-147\,(n_1 - n_2)^4$ contribution to the fourth order term. The formula given in [153], however, is identical to Eq. 4.6 except from a typo: the square on the second order F term is missing. This is the formula that will be used throughout this thesis and the obtained ionization rates are found to be in agreement with literature.

$$
\begin{aligned}
E = &-\frac{1}{2n^2} + \frac{3}{2}nF\left(n_1 - n_2\right) - \frac{1}{16}n^4F^2\left(17n^2 - 3\left(n_1 - n_2\right)^2 - 9m^2 + 19\right) + \\
&+ \frac{3}{32}n^7F^3\left(n_1 - n_2\right)\left(23n^2 - \left(n_1 - n_2\right)^2 + 11m^2 + 39\right) + \\
&- \frac{1}{1024}n^{10}F^4\left(5487n^4 + 35182n^2 - 1134m^2\left(n_1 - n_2\right)^2 + \right. \\
&+1806n^2\left(n_1 - n_2\right)^2 - 3402n^2m^2 - 3093\left(n_1 - n_2\right)^4 + \\
&\left.-549m^4 + 5754\left(n_1 - n_2\right)^2 - 8622m^2 + 16211\right). \qquad (4.6)
\end{aligned}
$$

In the present study it is crucial to precisely know which n-manifolds are (fully, partially or not yet) ionized at a given electric field strength. This requires to fix a range of ionization rates Γ according to experimental constraints. In the given case the ionization is required to happen within a few mm of beam path between the 30 mm long field ionizer meshes. Typical beam velocities dealt with in both hydrogen and antihydrogen experiments are $0.1\,\mathrm{km\,s^{-1}} \leq v \leq 10\,\mathrm{km\,s^{-1}}$. This results in required ionization rates of the order of $10^5\,\mathrm{s^{-1}} \leq \Gamma \leq 10^7\,\mathrm{s^{-1}}$. Fig. 4.9 illustrates, for the two extremes of this range of rates and a fixed field $F = 8\,\mathrm{kV\,cm^{-1}}$, the fraction of ionized substates of a given n-manifold as a function of n. For this field configuration, partial ionization of the $n = 16$ states is only visible for the lower end of the range of rates considered (i.e. $1 \times 10^5\,\mathrm{s^{-1}}$). For the $n = 17$ manifold the spread of the ionization fraction for the different Γ is maximal and amounts to $\sim 15\,\%$. For $n > 17$ the fraction of substates ionized per manifold is quite similar.

From Fig. 4.9 one can extract the maximum n which remains intact (n_{max}) and the minimum n which is fully ionized (n_{min}) for a given electric field. When scanning the field, one obtains Fig. 4.10. The minimal and maximal n quantum number of only partially ionized manifolds as a function of the strength of the ionizing field is shown for the minimal and maximal ionization rate Γ chosen above. With the inter-n-manifold spacing decreasing with n^{-3}, the spread of n manifolds partially contributing to the ionization signal obtained for weakly bound states is drastically increased compared to the stronger bound levels. The graphs for the two different Γ considered only differ marginally. Indeed, the plot presented, for example, in Fig. 6 of [154] shows that for a range of ionization rates over several orders of

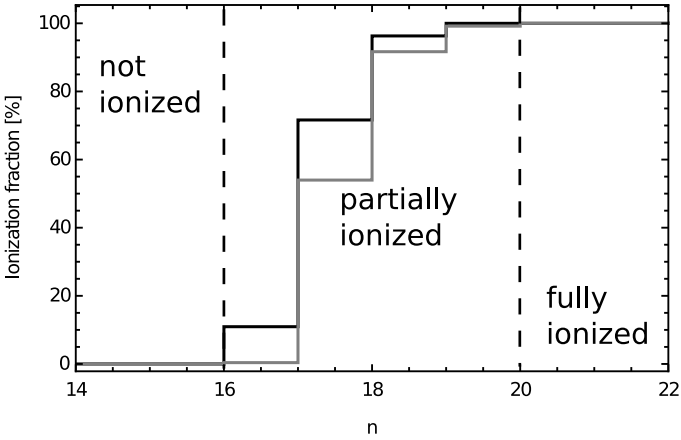

Figure 4.9: Ionization fraction of different n-manifolds for a fixed electric field strength of 8 kV cm^{-1}. The fraction indicated is the number of substates ionized divided by n^2. The ionization rates are 1×10^5 s^{-1} (1×10^7 s^{-1}) for the black (gray) graph.

magnitude (once the ionization onset field is reached) the corresponding ionization field only varies slightly.

Rydberg state detection out of a discharge plasma

In order to measure the Rydberg content of the hydrogen beam at the end of the beamline, the field ionizer was used in conjunction with a MCP (cf. subsection 4.3.1). The MCP (front/back/anode) voltages amounted to (−2 kV/GND/50 V). The signal recorded was measured as a function of the voltage applied to the field ionizer meshes. When both FI meshes are grounded, the MCP detects a background rate originating from protons or other ions such as, for example, H_2^+ emitted from the plasma. A detailed SIMION [155] simulation showed that incoming protons from the beam cannot be responible for a higher detected rate on the MCP at high field ionizer settings [156]. In fact, the negative MCP front plate potential collects (for grounded field ionizer meshes) all positively charged particles from the beam

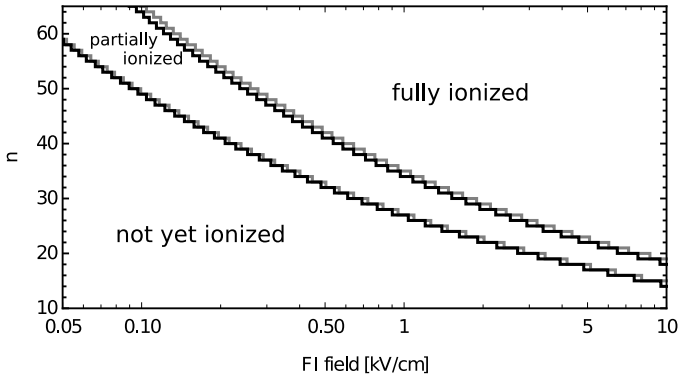

Figure 4.10: Minimal n_{min} and maximal n_{max} quantum numbers partially contributing to the (anti-)hydrogen ionization signal as a function of the electric field strength. The lower curves indicate the ionization onset and thus the n-manifold in which few of the easiest to ionize states are ionized. The upper curves, in contrast, show the n quantum number of the lowest manifold that is fully ionized. Below this threshold, substates that are comparatively easy to ionize within their n-manifold may contribute to the detected ionization signal. The ionization rates are 1×10^5 s^{-1} (1×10^7 s^{-1}) for the black (gray) graph.

such that they are accounted for in the measurement background if not deflected before and blocked by the apertures between the different chambers. This was experimentally confirmed, in a prior setup (not shown), by collecting charged particles emitted out of the source with a separate set of deflector plates such that only neutral atoms would travel unperturbed all the way to the detection region. In the beamline presented here, latter plates were omitted for the sake of a better cryogenic shielding of the beam.

Fig. 4.11 shows the cumulative background-subtracted rate of detected protons from hydrogen ionization as a function of the principal quantum number n of the addressed levels. The maximum electric field strength amounts to $7.2\,\mathrm{kV\,cm^{-1}}$ ionizing substates down to $n = 16$. The E-field was scanned in steps of $400\,\mathrm{V\,cm^{-1}}$. The horizontal error bars mainly originate from the theoretical considerations above and represent the range of n-manifolds partially ionized for the given field ionizer setting. Errors introduced by mounting inaccuracies of the field ionizer meshes which are mounted at a distance of 5.0(5) mm and the high voltage control operating at a precision of $\pm 1\,\mathrm{V}$ are taking into consideration. The field ionization potential (positive polarity) was applied to the ionization mesh on the far side of the MCP whereas the mesh on the near side was grounded. The H_2 flow amounted to $0.8\,\mathrm{cm^3\,min^{-1}}$ (at standard conditions) and the microwave power forwarded to the plasma sustained by the Evenson cavity was 30 W.

Rydberg hydrogen atoms formed in the source and exiting toward the end of the beamline are subject to spontaneous emission as well as light induced deexcitation, excitation and ionization that can be partly due to blackbody photons emitted by the surrounding experiment. The thermal beam shield was operated at 58(1) K. At this temperature, the blackbody band emittance for frequencies $200\,\mathrm{GHz} \leq \nu \leq 500\,\mathrm{GHz}$ (this is the range required to mix states with $25 \leq n \leq 30$ in a deexcitation experiment, cf. section 3) is reduced by a factor 6 compared to temperatures of 300 K.

Prior calculations showed that an atomic hydrogen flux of the order of $10^{18}\,\mathrm{s^{-1}}$ can be expected (cf. subsection 4.3.2). For the presently treated electron densities and normalized contributions of the excitation and recombination channels in Yacora, the $R_{0,20}$ population coefficient is of the order of $10^{-21}\,\mathrm{m^3}$ (cf. subsection 4.4.1). This leads to n_{20}/n_{H} between 1×10^{-6} and 1×10^{-7}. In order to estimate the expected Rydberg beam rate at the field ionization region in the Rydberg beamline, the solid angle coverage of the pinhole (diameter 0.5 mm) at a position of 10 cm

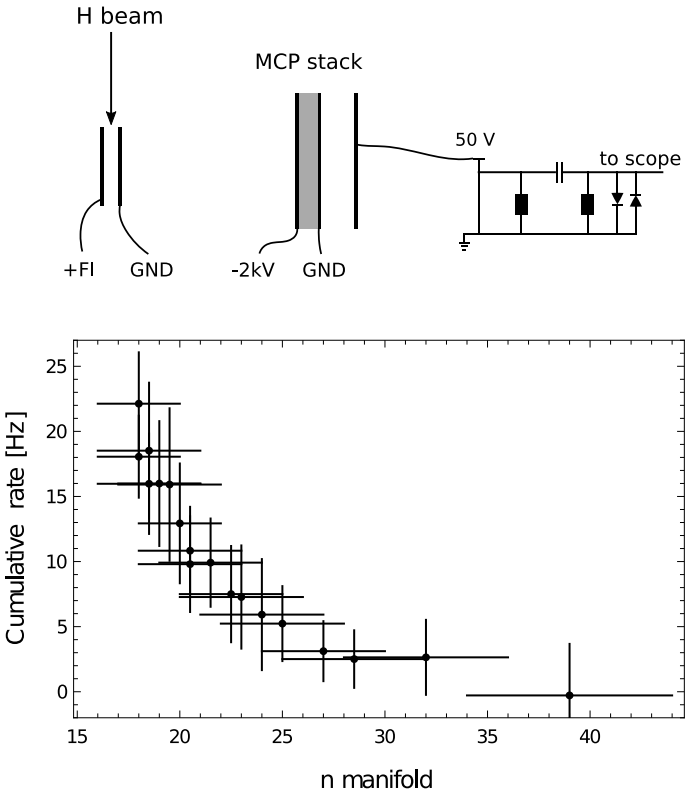

Figure 4.11: Cumulative background subtracted proton rate from ionization of Rydberg hydrogen states as a function of their respective principal quantum number n. Vertical errorbars indicate the standard deviation of the signal acquired. Horizontal error bars originate from theoretical limits of electric field ionization (assuming an ionization rate of 1×10^5 s^{-1}) and experimental uncertainties of the electric field strength as outlined in the text.

downstream the plasma region needs to be taken into account and amounts to 1×10^{-6}. One could thus expect beam rates between $1 \times 10^5\,\mathrm{s}^{-1}$ and $1 \times 10^6\,\mathrm{s}^{-1}$ for states with $n = 20$.

The discrepancy to the detected rates of some tens of Hz most probably originates from rather small ion densities in the Evenson discharge plasma. Taking this into account, the population coefficient can rapidly vary over several orders of magnitude (cf. Fig. 4.8). Further, the radiative decay of short lived states (the lifetime $\tau \propto l^2$) toward ground state must be considered to have a significant impact. Indeed, flight times of the order of hundreds of µs need to be taken into account. The absence of states $n > 40$ can be explained by ionization through the microwaves sustaining the plasma discharge. Indeed, a power of 30 W on 1 cm leads to field strengths of $150\,\mathrm{V\,cm}^{-1}$ resulting in the ionization of states down to $n \sim 45$. Another possibility to explain the absence of states with $n > 40$ lies in ionization in the beam, upstream of the FI, by the fringe field of the MCP front plate. Simulations showed [156] that field strengths close to $100\,\mathrm{V\,cm}^{-1}$ along the beam path are possible. In any case, a more quantitative theoretical assessment of these processes remains difficult due to the lack of knowledge of the initial state distribution emerging from the plasma.

The data shown in Fig. 4.11 has been acquired across a range of different molecular hydrogen flows and incident microwave powers sustaining the discharge inside the Evenson cavity. No statistically significant change in signal has been observed. The plasma parameter thus do not drastically change within the range of experimental parameters probed. Earlier considerations, based on the light spectra emitted by the plasma, resulted in estimated electron temperatures between 0.5 and 1 eV. From Fig. 4.8, one can indeed conclude that the recombination channels (and most others except from the H and $H^- + H^+$ one) are, in this range, rather insensitive to the electron temperature. In contrast, recalling the two-fold change in ground state atom emittance out of the plasma (cf. Fig. 4.7) as a function of varying H_2 flow, one might as well expect a change in the Rydberg beam content. Part of an explanation can again be a comparatively low ion density that limits recombination processes and thus higher atomic ground state densities do not lead to higher Rydberg state production.

The graph is non-linear and points toward a slightly elevated Rydberg state production rate toward $n \sim 16$ which is the limit probed by the field ionizer. Such a behavior could well be due to formation channels other than recombination

processes, most prominently electron collisions, that can start to dominate toward the stronger bound levels. In contrast to ions, the plasma contains electrons in large quantities and one could thus expect a change in low n states as a function of the H_2 flow. More elaborate studies in this low n region are, however, quite difficult. The electric field required to investigate states below $n \sim 15$ rapidly increases. In addition, one needs to consider that spontaneous emission depopulates levels below $n < 15$ within lifetimes of the order of a few tens of µs. The signal is thus, in the present experimental configuration, expected to level off quite rapidly.

The data shown in Fig. 4.11 has been acquired at a constant radiation shield temperature. Similar to the scans of forwarded power and pressure mentioned above, the temperature was scanned between room temperature and $\sim$40 K (here the band emittance at frequencies between 200 and 500 GHz is reduced by more than an order of magnitude compared to 300 K). The results do not reveal a statistically significant impact of black-body radiation on the atomic beam. This may be due to (possibly a combination) of two reasons: The atomic flight times of the order of hundreds of µs are too long to observe an effect of an order of magnitude reduction of BBR band emittance and/or the beam predominantly contains high m (circular) states at the detection region that exhibit small ionization cross sections (cf. Fig. 11 in [1] and Fig. 12 in [79]). Such an argument is strongly supported by theoretical studies by Flannery et al. [114] who investigated the Rydberg spontaneous decay cascade favorably forming circular states.

As mentioned before, the availability of Rydberg states directly from the source, as demonstrated here, is highly interesting in the framework of deexcitation since it somewhat reproduces the conditions faced in experiments at CERN's AD where, in general, a range of antihydrogen states needs to be brought to ground state rapidly (cf. section 1.2). However, detected rates are small and seemingly insensitive within the range of plasma parameters currently in reach with the Evenson cavity. More diagnostics (as already pointed out, the installation of a Langmuir probe looks promising) would certainly be needed before further attempts of rate optimization and ultimately deexcitation.

Finally, in addition to deexcitation studies, the obtained data can be valuable to benchmark Rydberg formation cross sections in collisional radiative models such as, for example, Yacora.

4.5 Rydberg hydrogen beam production relying on optical excitation

The production of Rydberg states within a discharge plasma has been discussed in subsection 4.4.1 and 4.4.2. An alternative approach is to (fully or partially) rely on optical excitation. The goal here is to populate a specific long-lived circular Rydberg state which is different from the distribution of levels generated via collisions and other channels inside the plasma. While the latter is closer to experimental conditions in $\overline{\mathrm{H}}$, the former would drastically facilitate the detection of Rydberg mixing and deexcitation. This is particularly critical when commissioning the required light sources in the first place. The theory is laid down in subsection 4.5.1 and the development of a single-mode Rydberg excitation laser is discussed in subsection 4.5.2.

4.5.1 Circular state production

Rydberg states can be produced from the meta-stable 2s hydrogen state with a visible laser driving transitions toward a highly excited p level. The meta-stable atoms can be produced from the ground state via, for example, collisional impact of electrons in a beam as reported in [157][7]. A detailed study of the excitation cross-section and beam scattering angles in such a process has been reported in [158]. An electron gun has been developed by collaborators from SMI in Vienna. The Rydberg beamline (cf. Fig. 4.5) has been designed in such a way, that the hydrogen beam can also be injected off-axis with only minor modifications by rotating the entire first chamber around its vertical axis. In such a setting, the momentum transfer of the scattered electrons deflects the beam on-axis in the central region of this chamber. The mean atomic beam deflection for hydrogen amounts to 20° [157] and is compensated by a customized vacuum bellow assembly. An additional

[7] In principle, a 2s beam should be emitted by the hydrogen discharge plasma sustained by the Evenson cavity. Studies on possible quenching of the meta-stable states at the edge of the plasma and on the detection of photons from 2s electric field quenching in the detection region of the Rydberg beamline are ongoing. Further, a beam velocity Doppler measurement is foreseen. A diode laser at 656 nm is currently being commissioned to excite from 2s to 3p and detect 3p to ground-state UV photons with the MCPs. If successful, this measurement will evidence, in addition to providing the beam velocity, the presence of 2s states.

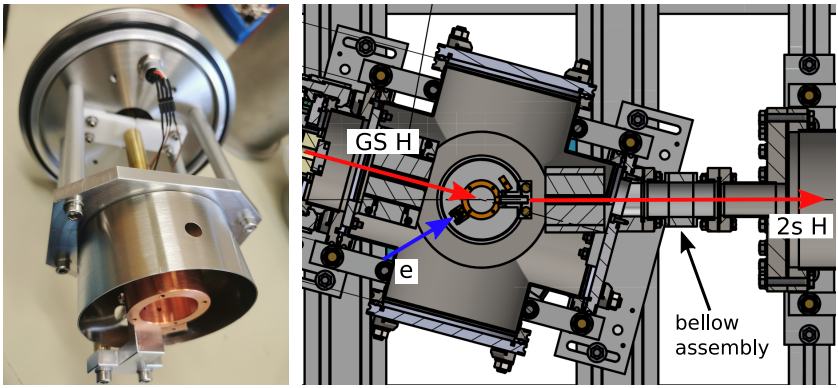

Figure 4.12: Picture of the electron gun and CAD drawing of the bellow assembly including the respective beam paths in the case of electron scattering in the first chamber for 2s collisional excitation from the ground state.

flexible bellow allows to scan a small range of angles around 20° which might be necessary for an optimization of electron impact angle and energy to achieve maximal excitation rates. A picture of the electron gun and the described modified chamber assembly is shown in Fig. 4.12.

Meta-stable 2s production via purely optical excitation from the ground state is generally possible for alkaline and alkaline earth atoms, but the transition wavelengths for single-photon transitions are small and notoriously hard to generate (at least with sufficient power and narrow linewidth). In hydrogen, a practical alternative is to rely on a two-photon 1s-2s transition at 243 nm (a single photon transition from ground state to 2s is highly forbidden due to angular momentum conservation). Further information including excitation cross sections can be found in, for example, [159]. A third option is optical pumping from the ground state toward the 3p states with a lamp to obtain meta-stable atoms according to the 12 % branching ratio via spontaneous decay [160].

Angular momentum to produce circular states with $m = \pm(n-1)$ from low-m levels can be provided by (1) additional microwave photons that are absorbed in the presence of an electric field which is adiabatically decreased [161]. Alternatively,

the excitation can take place (2) in the presence of a circularly polarized microwave field which is switched off adiabatically [162] or by (3) adiabatic redefinition of the quantization basis relying on electric fields in the presence of a near perpendicular small magnetic field [163] (crossed-field method). The study presented in [164] provides great detail and experimental results on option (2) and (3) in hydrogen. The method relying on crossed electric and magnetic fields (3) is closely linked to the pulsed deexcitation studies presented in chapter 3. The appropriate formalism to compute energy levels and transition dipoles is developed in chapter 2. In the framework of circular state production, the idea is to excite atoms toward the outermost Stark shifted states while applying weak magnetic (perpendicular to the beam propagation direction) and modest electric (parallel to the beam) external fields. Within this Stark limit ($\Delta E_{\mathrm{Stark}} \gg \Delta E_{\mathrm{Zeeman}}$), these are states with $m = 0$ and are thus accessible via lasers from, for example, $n = 2$. Once electrons have been excited, the electric field is adiabatically decreased to zero and the states are transferred to (in the Zeeman limit ($\Delta E_{\mathrm{Zeeman}} \gg \Delta E_{\mathrm{Stark}}$) circular $|m| = -(n-1)$ levels (cf. Fig. 1 in [164]). Building upon the deexcitation theory presented in [2] and throughout this work, excitation transition rates for different of such crossed field configurations have been investigated in [149]. Implementing the required crossed magnetic (2 mT) and electric (50 V cm^{-1}) fields with permanent magnets and standard electrodes seems experimentally feasible. The adiabatic switching condition for the electric field F is [164]

$$\dot{F} \ll \frac{18B^2}{n} = 240,$$

where F is given in units of V cm^{-1} µs^{-1} and B in Gauss. Hence, a field switching time of the order of $\sim$10 µs seems reasonable. At beam velocities of some 1000 m s^{-1} this corresponds to a flight path of the order of cm. An alternative to actively switching the field might thus be to keep the field constant and benefit from the electrodes' few cm fringe field region to adiabatically transfer the atoms into a field-free configuration. A detection scheme relying on field ionization to evidence the production of circular Rydberg states is already in place (cf. the ionization signal to be expected as shown in Fig. 14 of [164]).

It is important to note that when exciting from the meta-stable 2s state toward $n \sim 30$, the mentioned electric field of 50 V cm^{-1} will start to Stark quench the 2s levels. Here, depopulation toward the ground-state via the 2p states is

highly undesired and would result in a drastically reduced excitation efficiency. Consequently, the fields need to be handled with care.

4.5.2 Rydberg single-mode emission excitation laser

A laser capable of exciting hydrogen atoms from the 2s state toward a low (l, m) Rydberg level with $n \sim 30$ has been developed, building upon a setup discussed in [165], by collaborators at Laboratoire Aimé Cotton. A commercial 10 ns pulsed Nd:YAG laser (Nano T 290-10 from Litron) is frequency doubled to 523 nm and injected into a gain switched Ti:Sa cavity. As an alternative to controlling the flash lamp intensity of the Nd:YAG laser for regulation of the pumping power, a waveplate and cubic beam splitter at the exit of the pump allow to dump (s-part) and transmit (p-part) certain fractions of the 532 nm beam. A telescope is used to reduce the beam waist to roughly 3 mm. The Ti:Sa cavity has a length of 0.4 m and consists of two prisms, the Ti:Sa crystal itself, an output coupler (20 % reflectivity) and two mirrors one of which is mounted onto a translational piezo-electric actuator to adjust the cavity length. The piezo is driven by a custom FPGA to either apply a sawtooth ramp to sweep the length of the cavity or to "mode-lock" the cavity to a desired wavelength (cf. Fig. 4.14a) [165]. In addition to the green pump, a continuous-wave (cw) Sacher TEC520 diode laser is fed into the cavity for initial alignment and later injection seeding. At the cavity exit a small fraction of the lasing beam is reflected, for diagnostics, onto a photodiode (Thorlabs biased silicion detector) and a fiber coupled wavemeter (HighFinesse WS-7). The cavity output is frequency doubled with a BBO crystal to obtain light pulses around 366 nm. A scheme of the setup is illustrated in Fig. 4.13.

The laser has been successfully commissioned at CERN. The initial alignment of the cavity can be evidenced by applying a voltage ramp to the piezo actuator and observing interferences of the diode laser beam inside the cavity with the photodiode detector. An example of proper alignment is given in Fig. 4.14a. In a second step the pumping beam needs to be superimposed to the laser diode inside the Ti:Sa crystal. Aligning the pump and the diode laser beam downstream of the prism and Ti:Sa crystal close to the piezo-electric mirror suffices (the wavelength dependent refraction at the Ti:Sa crystal is rather small) to get close to lasing. Small adjustments on the cavity optics then allow to optimize, at a fixed pump power, for maximum pulse energies. Average pulse energies (without injection seeding)

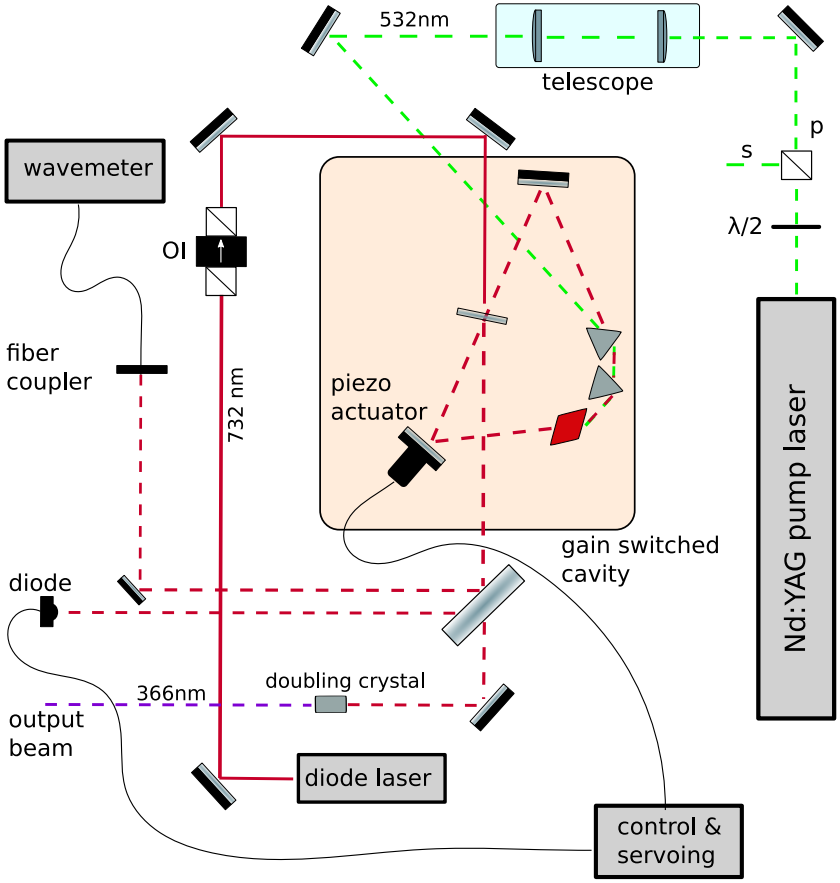

(a) Scheme of the Rydberg excitation laser.

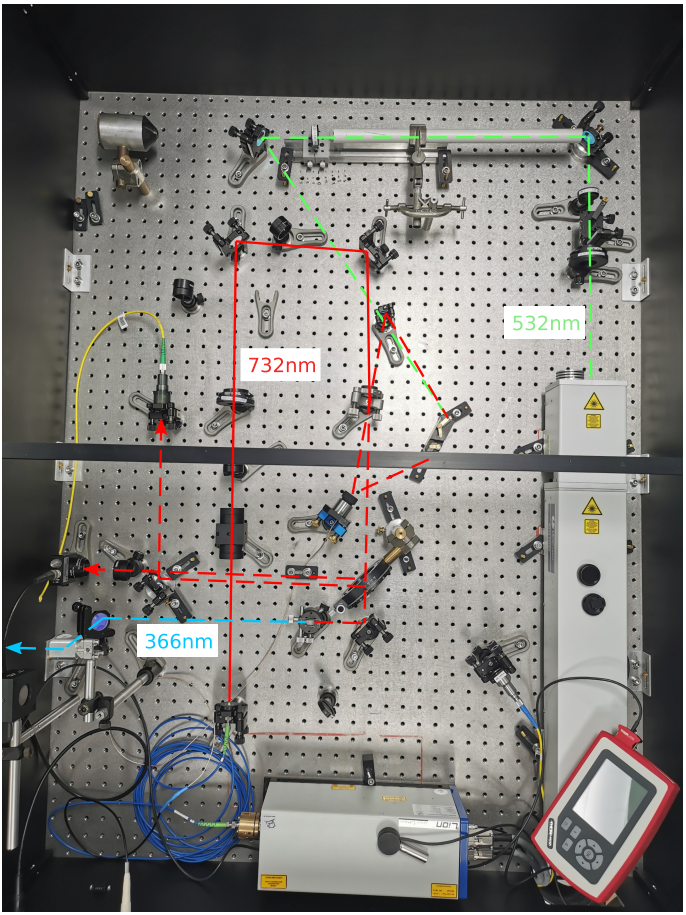

(b) Photo of the Rydberg excitation laser.

Figure 4.13: Sketch (a) and photo (b) of the laser. The setup employs a gain switched Ti:Sa cavity that is pumped by a commercial frequency doubled Nd:YAG laser. The cavity is seeded with a red diode laser. The emerging single mode 732 nm lasing beam is frequency doubled with a BBO crystal to generate the output light at 366 nm.

of the different frequencies are plotted in Fig. 4.14b. Once an optimal alignment of the pump and the cavity is found, the injection diode needs to most likely be realigned. In contrast to unseeded multi-mode operation, now the cw diode laser injects optical power into a single cavity mode. Thus, this mode starts to build up from much higher power compared to others and then dominates the cavity output resulting in spectrally narrow light emission. Seeding can be equally evidenced by a ~ 20 ns shorter pulse build-up time (cf. Fig. 4.14c). Finally, the forward pulse energy is roughly doubled. In fact, the beam inside the cavity is circulating, if seeded, only unidirectional compared to bidirectional in the unseeded case [165].

In summary, the required light for the targeted transition toward 30p levels is available. However, due to their short lifetimes (the spontaneous emission rate scales as l^{-2}), the detection of 30p states at the end of the beamline relying on field ionization is only possible after excitation to a high (l, m), ideally circular, level. The installation of the necessary electric and magnetic fields is scheduled within the next months.

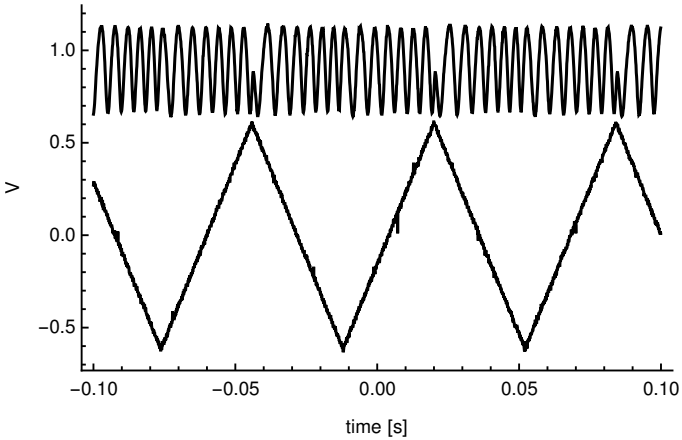

(a) Diode detector signal and piezo-mirror voltage ramp showing cavity interferences of the seeding diode laser

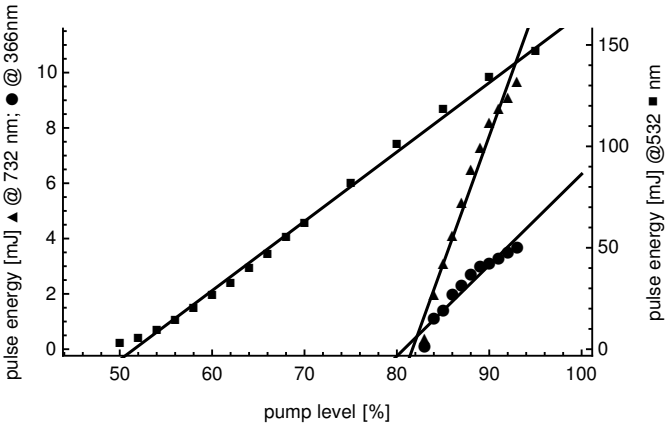

(b) Output power of the pumping laser, (unseeded) cavity and THG beam as a function of the pump level

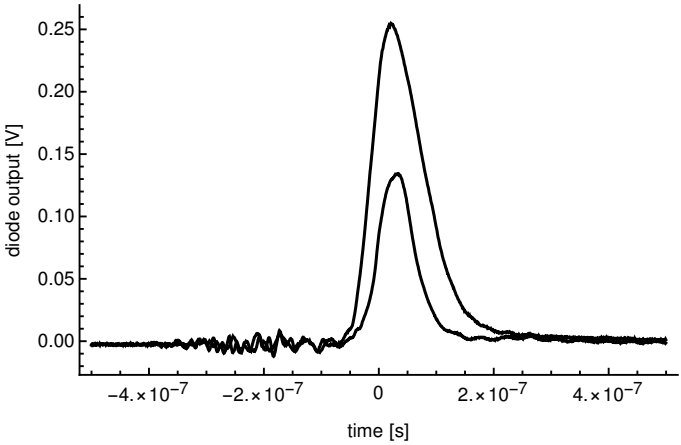

(c) Diode detector signal for a seeded and unseeded cavity output beam

Figure 4.14: (a) Diode laser interferences building up inside the cavity for varying cavity lengths as a function of the piezo-mirror voltage (b) Output average pulse energies as measured for the different wavelengths generated (c) Diode detector signal at the exit of the Ti:Sa cavity for single-mode (injection seeded, larger pulse) and multi-mode emission (unseeded, smaller pulse) beam.

5 Conclusion

The results and main findings of the work reported in this thesis are recapitulated in section 5.1. A link of this work to disciplines and applications beyond antihydrogen research at CERN is established in section 5.2 .

5.1 Summary and outlook

The work presented throughout this thesis lays the foundation toward the production of large antihydrogen samples in ground state via controlled manipulation of Rydberg quantum states.

A theoretical framework and appropriate software has been developed to simulate the interaction of (anti-)hydrogen atoms with light in crossed electric and magnetic as well as pure magnetic fields relying on rate equations. The efficiency of deexcitation schemes in various experimental conditions and configurations, suitable for CE and/or 3BR production of anti-atoms, has been assessed theoretically. For both formation mechanisms, results that comply with the experimental requirements were identified. Close to unity ground state fractions of the initial $n = 30$ substates have been obtained within a few tens of µs. Combining such stimulated deexcitation of bound levels with stimulated radiative recombination yielded promising ground-state anti-atom formation rates compared to the current state-of-the-art. Building upon prior work from Wolf et al. [54], a first detailed simulation of this process has been performed within a magnetic field as present in state-of-the-art antimatter experiments. The impact of the simulation results on antihydrogen beam experiments has been discussed. Further, the general working principles of a deexcitation use-case for enhanced trapping and cooling of atoms

within a magnetic field gradient (as present inside a neutral atom trap) has been laid down.

A link of the presented studies to deexcitation relying on collisional processes along the passage through, for example, an electron plasma has been established. This seems particular interesting for states $n > 30$ where collisional population transfer is most efficient due to the increasingly small energy spacing of the addressed levels. A combination of such a scheme with light stimulated deexcitation targeting states around $n \sim 30$ and below might yield a drastically increased absolute number of ground state atoms.

On the experimental side, a discussion on the feasibility and suitability of different light sources for antihydrogen deexcitation was followed by the report on a proof-of-principle Rydberg state transfer within an excited beam of cesium atoms. Building upon this, developments toward a hydrogen proof-of-principle have been treated. A plasma discharge source to produce an atomic hydrogen beam has been commissioned at a newly designed and built beamline. Different ways to produce an excited beam have been investigated. First, relying on electric field ionization, a distribution of Rydberg states that is emitted out of the plasma has been detected. Alternatively, radiative-radiative or collisional-radiative excitation schemes from the ground state have been discussed. For this purpose, a pulsed YAG pumped Ti:Sa excitation laser capable of stimulating transitions from $n = 2$ to $n \sim 30$ states has been commissioned in a newly built laser laboratory at CERN.

An appropriate configuration including the required switching conditions of electric and magnetic fields required to excite toward circular Rydberg states has been identified. The experimental implementation is still pending, but permanent magnets and a foreseen rather simple design of a set of electrostatic electrodes will allow swift installation. In order to proceed, once circular Rydberg states have been detected, with hydrogen deexcitation studies, the required light input toward the photomixer to produce light in the THz frequency range needs to be developed. Initial studies with the mentioned black body emitter can be done right away. The development of a deexcitation laser in collaboration with industry partners has been initiated.

Simulation results of plasma processes in view of both atomic hydrogen beam production and Rydberg state formation have been presented using Yacora on the Web. It might be meaningful to switch to an offline version that allows access to

population densities of states with $n > 20$ and at $T_e < 1\,\mathrm{eV}$ which is the current limitation using the web version. Further, it would be interesting to study the population of sublevels, ideally in a magnetic and/or electric field environment. Finally, the observed formation of Rydberg states has the potential to benchmark CR models within the Rydberg regime where the knowledge of cross sections etc. is still sparse. Such studies would be of particular interest in the framework of stimulated deexcitation within an electron plasma as discussed in subsection 3.5.2.

5.2 Transfer potential of the work presented

The controlled manipulation, mixing and (de-)excitation of Rydberg states in alkaline (and other) atoms is of interest across a wide range of disciplines in fundamental research and emerging quantum technologies. A (by far not complete) selection of applications is briefly discussed in the following to convey an impression of the interdisciplinary nature of the field and, in particular, the work presented throughout this thesis.

In quantum computing, trapped neutral atoms have become a viable alternative to superconducting qbits and those based on trapped ions [166]. Indeed, atomic systems exhibit a variety of exclusive advantages such as long decoherence times, accurate state manipulations via lasers and the general scalability of such platforms. In particular, Rydberg atoms are ideal candidates for quantum state entanglement due to their large dipole moments and polarizability (scaling as n^7) enabling atomic Rydberg-Rydberg interactions over several µm. The interaction strength strongly depends on n. In, for example, Rb atoms the 100s states interact roughly 12 orders of magnitude stronger than atoms in ground state. In contrast to Coulomb interacting trapped ions, the atoms' coupling can thus be switched on and off with lasers which appears beneficial when working toward many-qbit registers [167]. In atomic arrays, the Rydberg excitation of an atom can prevent the excitation of neighbouring atoms within the interaction (blockade) radius (Rydberg excitation blockade [168]). This phenomenon, relying on induced energy shifts of atomic states in such a way that the excitation laser is off-resonance, is an ideal playground for the construction of quantum logic gates since the excitation of one atom conditions the quantum state evolution of neighbouring ones. Competitive high-fidelity entanglement (> 0.99) of atomic states and their detection has just been

recently demonstrated making use of an array of strontium atoms [169]. The techniques required to prepare and control the atomic quantum states as well as limitations introduced by mechanisms like e.g spontaneous decay are indeed quite similar to what has been discussed in this work.

Alkaline Rydberg atoms exhibit a great variety of easy-to-drive – the dipoles are very large – transitions within the microwave and THz frequency range that are sensitive to external electric (and magnetic) fields as discussed in chapter 2 and 3. Field induced shifts of atomic transition frequencies can be exploited for self calibrated sensing of small amplitude external electromagnetic fields. Setups making use of cesium or rubidium vapor cells with sensitivities $< 1\,\mu\mathrm{V\,cm^{-1}}$ per frequency $f^{1/2}$ have been demonstrated [170]. Detection techniques include electromagnetically induced transparency (EIT) introduced by so-called probe and coupling lasers. The presence of an electromagnetic field can be detected via the effect it has on the upper EIT state varying the transmission of the probe laser through the atomic vapor (cf. [171] or the review of Rydberg quantum technologies [172]). Alternatively, fluorescence of light (often referred to as THz imaging) can be used to detect the coupling of two Rydberg levels (one of which needs to be again prepared in the first place by lasers). A proof-of-principle of Rydberg atom AC/DC voltage measurements can be found in [173].

Single photon sources (for example solid state sources [174], quantum dots [175] or single molecules) that are required in quantum communication and sensing applications usually operate at cryogenic temperatures. Due to their strong interaction, Rydberg atoms allow to build single photon sources on atomic vapor cells at room temperature [176]. Nanosecond pulsed lasers (timescales at which the thermal sample can be assumed to be frozen) excite the atoms, quite similar to what has been discussed throughout the experimental part of this work, to Rydberg states. Rydberg blockade processes suppress multiple excitation within the gas. Spontaneous emission in the carefully chosen atomic level system then allows to obtain single photons on demand.

Quantum Rydberg gas trace sensors at the 10 ppm level operating at atmospheric pressures have been demonstrated [177]. In such setups, Rydberg excited nitric oxide (NO) is laser excited to a Rydberg state and ionized via colissional processes within a He gas mixture. Related processes for state mixing have been discussed in the framework of stimulated radiative recombination in section 3.4 and deexcitation in section 3.5.2. The nascent charges are detected on metallic electrodes and

amplified through dedicated electronics. Such quantum trace gas sensors offer very good selectivity and high sensitivity with potential applications in the health sector or, for example, automobile exhaust emission testing.

Finally, a variety of private companies and start-ups [178] are working toward quantum information processing [179] and sensing [180] using, among others, Rydberg atom technology.

Bibliography

[1] T. Wolz, C. Malbrunot, M. Vieille-Grosjean, and D. Comparat, “Stimulated decay and formation of antihydrogen atoms”, Phys. Rev. A **101**, 043412 (2020).

[2] D. Comparat and C. Malbrunot, “Laser stimulated deexcitation of Rydberg antihydrogen atoms”, Phys. Rev. A **99**, 013418 (2019).

[3] D. Comparat and C. Malbrunot, “Erratum: Laser-stimulated deexcitation of Rydberg antihydrogen atoms [Phys. Rev. A 99, 013418 (2019)]”, Phys. Rev. A **101**, 019904 (2020).

[4] C. Malbrunot, T. Wolz, L. Nowak, and D. Comparat, “Simulation of antihydrogen deexcitation in neutral atom traps for improved trapping and cooling”, J. Phys. B, in press (2022).

[5] B. Kolbinger, C. Amsler, S. C. Arguedas, H. Breuker, et al., “Measurement of the principal quantum number distribution in a beam of antihydrogen atoms”, Eur. Phys. J. D **75**, 3 (2021).

[6] M. Vieille-Grosjean, Z. Mazzotta, D. Comparat, E. Dimova, T. Wolz, and C. Malbrunot, “Induced terahertz transitions in Rydberg cesium atoms for application in antihydrogen experiments”, Eur. Phys. J. D **75**, 27 (2021).

[7] C. S. Wu, E. Ambler, R. W. Hayward, D. D. Hoppes, and R. P. Hudson, “Experimental test of parity conservation in beta decay”, Phys. Rev. **105**, 1413–1415 (1957).

[8] J. Christenson, J. W. Cronin, V. L. Fitch, et al., “Evidence for the 2π Decay of the K_0^2 meson”, Phys. Rev. Lett. **13**, 138 (1964).

[9] A. Sakharov, “Violation of CP invariance, C asymmetry and baryon asymmetry of the universe”, J. Exp. Theor. Phys. **5**, 24 (1967).

[10] J. Ellis, “Antimatter matters”, Nature **424**, 631–634 (2003).

[11] C. D. Anderson, “The positive electron”, Phys. Rev. **43**, 491–494 (1933).

[12] O. Chamberlain et al., “Observation of antiprotons”, Phys. Rev. **100**, 947 (1955).

[13] B. Cork et al., “Antineutrons produced from antiprotons in charge-exchange collisions”, Phys. Rev. **104**, 1193 (1956).

[14] G. Baur, G. Boero, S. Brauksiepe, and A. Buzzo, “Production of antihydrogen”, Phys. Lett. B **368**, 251–258 (1996).

[15] M. Hori and J. Walz, “Physics at CERN’s antiproton decelerator”, Prog. Part. Nucl. Phys. **72**, 206–253 (2013).

[16] M. Ahmadi, B. X. R. Alves, C. J. Baker, W. Bertsche, et al., “Characterization of the 1s-2s transition in antihydrogen”, Nature **557**, 71–75 (2018).

[17] M. Ahmadi, B. X. R. Alves, C. J. Baker, W. Bertsche, et al., “Observation of the 1s-2p Lyman-α transition in antihydrogen”, Nature **561**, 211–215 (2018).

[18] M. Ahmadi, B. X. R. Alves, C. J. Baker, W. Bertsche, et al., “Observation of the hyperfine spectrum of antihydrogen”, Nature **548**, 66–69 (2017).

[19] M. Ahmadi, B. X. R. Alves, C. J. Baker, W. Bertsche, et al., “Investigation of the fine structure of antihydrogen”, Nature **578**, 375–380 (2020).

[20] M. Ahmadi, B. X. R. Alves, C. J. Baker, W. Bertsche, et al., “Description and first application of a new technique to measure the gravitational mass of antihydrogen”, Nat. Commun. **4**, 1785 (2013).

[21] E. S. Chang, “Radiative lifetime of hydrogenic and quasihydrogenic atoms”, Phys. Rev. A **31**, 495–498 (1985).

[22] M. Ahmadi, B. X. R. Alves, C. J. Baker, W. Bertsche, et al., “Antihydrogen accumulation for fundamental symmetry tests”, Nat. Commun. **8**, 681 (2017).

[23] N. Kuroda, S. Ulmer, D. J. Murtagh, S. V. Gorp, et al., “A source of antihydrogen for in-flight hyperfine spectroscopy”, Nat. Commun. **5**, 3089 (2014).

[24] R. Lundmark, C. Malbrunot, Y. Nagata, B. Radics, et al., “Towards a precise measurement of the antihydrogen ground state hyperfine splitting in a beam: the case of in-flight radiative decays”, J. Phys. B **48**, 18, 184001 (2015).

[25] The AEGIS Collaboration, *Proposal for the AEGIS experiment at the CERN antiproton decelerator*, Proposal (CERN, 2007).

[26] C. Amsler, M. Antonello, A. Belov, et al., “Pulsed production of antihydrogen”, Nat. Commun. **4**, 19 (2021).

[27] G. Gabrielse, P. Larochelle, D. Le Sage, B. Levitt, et al., “Antihydrogen production within a Penning-Ioffe trap”, Phys. Rev. Lett. **100**, 11, 113001 (2008).

[28] *AEGIS website*, `https://aegis.web.cern.ch/aegis/home.html`, Accessed: 2021-11-07.

[29] D. Krasnicky, G. Testera, and N. Zurlo, “Comparison of classical and quantum models of anti-hydrogen formation through charge exchange”, J. Phys. B **52**, 11, 115202 (2019).

[30] D. Krasnický, R. Caravita, C. Canali, and G. Testera, “Cross section for Rydberg antihydrogen production via charge exchange between Rydberg positroniums and antiprotons in a magnetic field”, Phys. Rev. A **94**, 2, 022714 (2016).

[31] M. Doser, C. Amsler, A. Belov, and G. Bonomi, “Exploring the WEP with a pulsed cold beam of antihydrogen”, Class. Quantum Gravity **29**, 18, 184009 (2012).

[32] G. Gabrielse, P. Larochelle, D. L. Sage, B. Levitt, et al. (ATRAP Collaboration), “Antiproton confinement in a Penning-Ioffe trap for antihydrogen”, Phys. Rev. Lett. **98**, 113002 (2007).

[33] P. Yzombard, M. Hamamda, S. Gerber, M. Doser, et al., “Laser cooling of molecular anions”, Phys. Rev. Lett. **114**, 213001 (2015).

[34] G. Cerchiari, P. Yzombard, and A. Kellerbauer, “Laser-assisted evaporative cooling of anions”, Phys. Rev. Lett. **123**, 103201 (2019).

[35] F. Robicheaux, “Atomic processes in antihydrogen experiments: a theoretical and computational perspective”, J. Phys. B **41**, 19, 192001 (2008).

[36] B. Radics, D. J. Murtagh, Y. Yamazaki, and F. Robicheaux, “Scaling behavior of the ground-state antihydrogen yield as a function of positron density and temperature from classical-trajectory Monte Carlo simulations”, Phys. Rev. A **90**, 3, 032704 (2014).

[37] S. Jonsell and M. Charlton, “Formation of antihydrogen beams from positron–antiproton interactions”, New J. Phys. **21**, 7, 073020 (2019).

[38] G. Gabrielse, N. S. Bowden, P. O. A. Speck, et al., “Driven production of cold antihydrogen and the first measured distribution of antihydrogen states”, Phys. Rev. Lett. **89**, 23, 233401 (2002).

[39] C. Malbrunot, C. Amsler, S. A. Cuendis, H. Breuker, et al., “The ASACUSA antihydrogen and hydrogen program: results and prospects”, Philos. Trans. Royal Soc. A **376**, 2116, 20170273 (2018).

[40] G. Gabrielse, N. S. Bowden, P. Oxley, A. Speck, et al., “Background-free observation of cold antihydrogen with field-ionization analysis of its states”, Phys. Rev. Lett. **89**, 21, 213401 (2002).

[41] Y. Enomoto, N. Kuroda, K. Michishio, C. H. Kim, et al., “Synthesis of cold antihydrogen in a cusp trap”, Phys. Rev. Lett. **105**, 24, 243401 (2010).

[42] G. B. Andresen, M. D. Ashkezari, M. Baquero-Ruiz, W. Bertsche, et al. (ALPHA Collaboration), “Evaporative cooling of antiprotons to cryogenic temperatures”, Phys. Rev. Lett. **105**, 013003 (2010).

[43] N. Madsen, M. Amoretti, C. Amsler, G. Bonomi, et al. (ATHENA Collaboration), “Spatial distribution of cold antihydrogen formation”, Phys. Rev. Lett. **94**, 033403 (2005).

[44] Y. Enomoto, N. Kuroda, K. Michishio, C. H. Kim, et al., “Synthesis of cold antihydrogen in a cusp trap”, Phys. Rev. Lett. **105**, 243401 (2010).

[45] M. Tajima, N. Kuroda, C. Amsler, H. Breuker, et al., “Antiproton beams with low energy spread for antihydrogen production”, **14**, 05, P05009–P05009 (2019).

[46] G. B. Andresen, M. D. Ashkezari, M. Baquero-Ruiz, W. Bertsche, et al. (ALPHA Collaboration), “Autoresonant excitation of antiproton plasmas”, Phys. Rev. Lett. **106**, 025002 (2011).

[47] S. Jonsell and M. Charlton, “On the formation of trappable antihydrogen”, New J. Phys **20**, 4, 043049 (2018).

[48] N. Madsen, F. Robicheaux, and S. Jonsell, “Antihydrogen trapping assisted by sympathetically cooled positrons”, New J. Phys. **16**, 6, 063046 (2014).

[49] C. J. Baker, W. W. Bertsche, A. Capra, et al., “Sympathetic cooling of positrons to cryogenic temperatures for antihydrogen production”, Nat. Commun. **12** (2021).

[50] W. A. Bertsche, E. Butler, M. Charlton, and N. Madsen, “Physics with antihydrogen”, **48**, 23, 232001 (2015).

[51] A. Wetzels, A. Gürtler, L. D. Noordam, and F. Robicheaux, “Far-infrared Rydberg-Rydberg transitions in a magnetic field: Deexcitation of antihydrogen atoms”, Phys. Rev. A **73**, 6, 062507 (2006).

[52] P. K. Mandal and A. Speck, “Half-cycle-pulse-train induced state redistribution of Rydberg atoms”, Phys. Rev. A **81**, 1, 013401 (2010).

[53] C. J. Baker, W. Bertsche, A. Capra, C. Carruth, et al., “Laser cooling of antihydrogen atoms”, Nature **592**, 35–42 (2021).

[54] A. Wolf, “Laser-stimulated formation and stabilization of antihydrogen atoms”, Hyperfine Interact. **76**, 1, 189–201 (1993).

[55] D. J. Griffiths and D. F. Schroeter, *Introduction to quantum mechanics*, 3rd ed. (Cambridge University Press, 2018).

[56] H. A. Bethe and E. E. Salpeter, *Quantum mechanics of one-and two-electron atoms* (Springer Science & Business Media, 2012).

[57] T. Breeden and H. Metcalf, “Stark acceleration of Rydberg atoms in inhomogeneous electric fields”, Phys. Rev. Lett. **47**, 1726–1729 (1981).

[58] J. Main, M. Schwacke, and G. Wunner, “The hydrogen atom in combined electric and magnetic fields with arbitrary mutual orientations”, Phys. Rev. A **57** (1997).

[59] E. A. Solov’ev, “Second order perturbation theory for the hydrogen atom in crossed electric and magnetic fields”, Zh. Eksp. Teor. Fiz. **85**, 109–114 (1983).

[60] Y. N. Demkov, B. S. Monozon, and V. N. Ostrovskiĭ, “Energy levels of a hydrogen atom in crossed electric and magnetic fields”, Sov. Phys. JETP **30**, 4 (1970).

[61] W. Pauli, “Über das Wasserstoffspektrum vom Standpunkt der neuen Quantenmechanik”, Z. Phys. **36**, 336–363 (1924).

[62] D. A. Varshalovich, A. N. Moskalev, and V. K. Khersonskii, *Quantum theory of angular momentum* (World Scientific Pub. Co., Teaneck, NJ, 1987).

[63] H. Friedrich and H. Wintgen, "The hydrogen atom in a uniform magnetic field—an example of chaos", Phys. Rep. **183**, 2, 37–79 (1989).

[64] R. H. Garstang and S. B. Kemic, "Hydrogen and Helium Spectra in Large Magnetic Fields", Astrophys. Space Sci. **31**, 1, 103–115 (1974).

[65] B. Blaive and M. Cadilhac, "A comparison of the hydrogenlike dipole radial matrix elements with overlap integrals and a step toward explicit expressions of the multipole matrix elements", J. Phys. B **42**, 16, 165002 (2009).

[66] A. Matsumoto, "Multiple matrix elements for hydrogen atom", Phys. Scr. **44**, 2, 154–157 (1991).

[67] C. J. Foot, *Atomic physics*, Oxford master series in physics (Oxford University Press, 2005).

[68] A. Einstein, "Zur Quantentheorie der Strahlung", Z. Phys. **18**, 121–128 (1917).

[69] L. Rodney, *The Quantum Theory of Light* (Clarendon Press, Oxford, 1973).

[70] D. Comparat, "Molecular cooling via Sisyphus processes", Phys. Rev. A **89**, 043410 (2014).

[71] E. Arimondo and G. Orriols, "Nonabsorbing atomic coherences by coherent two-photon transitions in a three-level optical pumping", Lett. Nuovo Cimento **17**, 333–338 (1976).

[72] M. Auzinsh, N. N. Bezuglov, and K. Miculis, "Manipulation of dark states and control of coherent processes with spectrally broad light", Phys. Rev. A **78**, 053415 (2008).

[73] T. Lindvall, T. Fordell, I. Tittonen, and M. Merimaa, "Unpolarized, incoherent repumping light for prevention of dark states in a trapped and laser-cooled single ion", Phys. Rev. A **87**, 013439 (2013).

[74] D. J. Berkeland and M. G. Boshier, "Destabilization of dark states and optical spectroscopy in Zeeman-degenerate atomic systems", Phys. Rev. A **65**, 033413 (2002).

[75] V. Debierre, T. Durt, A. Nicolet, and F. Zolla, “Spontaneous light emission by atomic hydrogen: Fermi’s golden rule without cheating”, Phys. Lett. A **379**, 40, 2577–2585 (2015).

[76] M. Vieille-Grosjean, “Atomes de Rydberg : Etude pour la production d’une source d’électrons monocinétique. Désexcitation par radiation THz pour l’antihydrogène”, Thèse de doctorat dirigée par Daniel Comparat, PhD thesis (Laboratoire Aimé Cotton, Orsay, France, 2018).

[77] P. Cacciani, L. Eliane, J. Pinard, C. Thomas, et al., “Rydberg atoms in parallel magnetic and electric fields. II. Theoretical analysis of the Stark structure of the diamagnetic manifold of hydrogen”, J. Phys. B **21**, 3499 (1999).

[78] P. A. Braunand and E. A. Solov’ev, “The stark effect for the hydrogen atom in a magnetic field”, Zh. Eksp. Teor. Fiz **86**, 68–83 (1984).

[79] C. Seiler, J. A. Agner, P. Pillet, and F. Merkt, “Radiative and collisional processes in translationally cold samples of hydrogen Rydberg atoms studied in an electrostatic trap”, J. Phys. B **49**, 9, 094006 (2016).

[80] P. M. Koch and K. A. H. van Leeuwen, “The importance of resonances in microwave “ionization” of excited hydrogen atoms”, Phys. Rep. **255**, 5-6, 289–403 (1995).

[81] A. Krug and A. Buchleitner, “Universal ionization threshold for strongly driven Rydberg states”, Phys. Rev. A **72**, 6, 061402 (2005).

[82] T. F. Gallagher, *Rydberg Atoms* (Cambridge University Press, Cambridge, 1994).

[83] S. Preu, G. H. Döhler, S. Malzer, L. J. Wang, et al., “Tunable, continuous-wave Terahertz photomixer sources and applications”, J. Appl. Phys. **109**, 6, 061301–061301 (2011).

[84] L. Yongqian, S. Park, and A. M. Weiner, “Terahertz waveform synthesis via optical pulse shaping”, Selected Topics in Quantum Electronics, IEEE Journal of **2**, 3, 709–719 (1996).

[85] A. J. Metcalf, V. R. Supradeepa, D. E. Leaird, A. M. Weiner, et al., “Fully programmable two-dimensional pulse shaper for broadband line-by-line amplitude and phase control”, Opt. Express **21**, 23, 28029–28039 (2013).

[86] M. Hamamda, P. Pillet, H. Lignier, and D. Comparat, "Ro-vibrational cooling of molecules and prospects", J. Phys. B **48**, 18, 182001 (2015).

[87] I. A. Finneran, J. T. Good, D. B. Holland, P. B. Carroll, and other, "Decade-spanning high-precision terahertz frequency comb", Phys. Rev. Lett. **114**, 16, 163902 (2015).

[88] P. Latzel, F. Pavanello, S. Bretin, M. Billet, et al., "High efficiency UTC photodiode for high spectral efficiency THz links", in 2017 42nd International Conference on Infrared, Millimeter, and Terahertz Waves (IRMMW-THz) (2017), pp. 1–2.

[89] G. I. Budker and A. N. Skrinskiı, "Electron cooling and new possibilities in elementary particle physics", Sov. Phys. Uspekhi **21**, 4, 277 (1978).

[90] R. Neumann, H. Poth, A. Winnacker, and A. Wolf, "Laser-enhanced electron-ion capture and antihydrogen formation", Z. Phys. **313**, 4, 253–262 (1983).

[91] G. Gabrielse, S. L. Rolston, L. Haarsma, and W. Kells, "Antihydrogen production using trapped plasmas", Phys. Lett. A **129**, 1, 38–42 (1988).

[92] A. Müller and A. Wolf, "Production of antihydrogen by recombination of $\bar{p}$ with e^+: What can we learn from electron–ion collision studies?", Hyperfine Interact. **109**, 1-4, 233–267 (1997).

[93] F. B. Yousif, P. V. der Donk, Z. Kucherovsky, J. Reis, et al., "Experimental observation of laser-stimulated radiative recombination", Phys. Rev. Lett. **67**, 1, 26 (1991).

[94] M. Rogelstad, F. Yousif, T. J. Morgan, and J. Mitchell, "Stimulated radiative recombination of H^+ and He^+", J. Phys. B **30**, 3913–3931 (1997).

[95] M. Amoretti, C. Amsler, G. Bonomi, P. D. Bowe, et al., "Search for laser-induced formation of antihydrogen atoms", Phys. Rev. Lett. **97**, 21, 213401 (2006).

[96] Y. Hahn, "Improved rates for three-body recombination at low temperature", Phys. Lett. A **264**, 6, 465–471 (2000).

[97] M. Fujiwara, M. Amoretti, C. Amsler, G. Bonomi, et al., "Temporally controlled modulation of antihydrogen production and the temperature scaling of antiproton-positron recombination", Phys. Rev. Lett. **101**, 053401 (2008).

[98] J. Bauche, C. Bauche-Arnoult, and O. Peyrusse, *Atomic properties in hot plasmas: from levels to superconfigurations* (Springer, 2015).

[99] B. W. Morrissey, "Microscopic reversibility and detailed balance. An overview", J. Chem. Educ. **52**, 5, 296 (1975).

[100] D. E. Osterbrock, *Astrophysics of gaseous nebulae and active galactic nuclei* (University Science Books, 1989).

[101] J. Weiner, V. S. Bagnato, S. Zilio, and P. S. Julienne, "Experiments and theory in cold and ultracold collisions", Rev. Mod. Phys. **71**, 1, 1 (1999).

[102] K. M. Jones, E. Tiesinga, P. D. Lett, and P. S. Julienne, "Ultracold photoassociation spectroscopy: long-range molecules and atomic scattering", Rev. Mod. Phys. **78**, 2, 483 (2006).

[103] S. T. Thompson, E. Hodby, and C. E. Wieman, "Ultracold molecule production via a resonant oscillating magnetic field", Phys. Rev. Lett. **95**, 19, 190404 (2005).

[104] S. Gerber, "Modeling of antihydrogen beam formation for interferometric gravity measurements", J. Phys. B **51**, 3, 035008 (2018).

[105] D. Vrinceanu, R. Onofrio, and H. R. Sadeghpour, "On the treatment of l-changing proton–hydrogen Rydberg atom collisions", Mon. Notices Royal Astron. Soc. **471**, 3, 3051–3056 (2017).

[106] P. Mansbach and J. Keck, "Monte Carlo trajectory calculations of atomic excitation and ionization by thermal electrons", Phys. Rev. **181**, 1, 275 (1969).

[107] F. Devos, J. Boulmer, and J. F. Delpech, "Transitions between Rydberg levels of helium induced by electron and neutral collisions", J. Phys. (Paris) **40**, 3, 215–223 (1979).

[108] L. Vriens and A. H. M. Smeets, "Cross-section and rate formulas for electron-impact ionization, excitation, deexcitation, and total depopulation of excited atoms", Phys. Rev. A **22**, 3, 940 (1980).

[109] T. Pohl, D. Vrinceanu, and H. R. Sadeghpour, "Rydberg atom formation in ultracold plasmas: small energy transfer with large consequences", Phys. Rev. Lett. **100**, 22, 223201 (2008).

[110] D. Comparat from Laboratoire Aimé Cotton (CNRS), Paris, "Private communication", 2020.

[111] M. Hori, E. Widmann, et al. (ASACUSA Collaboration), *ASACUSA status report - recent progress and plans for 2020*, tech. rep. (CERN, 2020).

[112] D. Wünderlich, M. Giacomin, R. Ritz, and U. Fantz, "Yacora on the Web: Online collisional radiative models for plasmas containing H, H2 or He", J. Quant. Spectrosc. Radiat. **240**, 106695 (2020).

[113] T. Pohl, H. R. Sadeghpour, Y. Nagata, and Y. Yamazaki, "Cooling by spontaneous decay of highly excited antihydrogen atoms in magnetic traps", Phys. Rev. Lett. **97**, 213001 (2006).

[114] M. R. Flannery and D. Vrinceanu, "Quantal and classical radiative cascade in Rydberg plasmas", Phys. Rev. A **68**, 030502 (2003).

[115] C. L. Taylor, J. Zhang, and F. Robicheaux, "Cooling of Rydberg $\overline{\mathrm{H}}$ during radiative cascade", J. Phys. B **39**, 23, 4945–4959 (2006).

[116] C. L. Cesar, F. Robicheaux, and N. Zagury, "Possible mechanism for enhancing the trapping and cooling of antihydrogen", Phys. Rev. A **80**, 041404 (2009).

[117] M. Hangyo, "Development and future prospects of terahertz technology", Jpn. J. Appl. Phys. **54**, 12, 120101 (2015).

[118] S. S. Dhillon, M. S. Vitiello, E. H. Linfield, and A. G. Davies, "The 2017 terahertz science and technology roadmap", J. Phys. D **50**, 4, 043001 (2017).

[119] K. Zhong, W. Shi, D. Xu, P. Liu, et al., "Optically pumped terahertz sources", Sci. China Technol. Sci. **60**, 12, 1801–1818 (2017).

[120] T. Elsässer, K. Reimann, and M. Woerner, *Concepts and applications of nonlinear terahertz spectroscopy* (Morgan & Claypool Publishers, 2019).

[121] P. R. Griffiths and C. C. Homes, "Instrumentation for far-infrared spectroscopy", Handbook of Vibrational Spectroscopy (2006).

[122] S. M. Hooker, "Developments in laser-driven plasma accelerators", Nat. Photonics **7**, 10, 775–782 (2013).

[123] Y. Shibata, K. Ishi, S. Ono, and Y. Inoue, "Broadband free electron laser by the use of prebunched electron beam", Phys. Rev. Lett. **78**, 14, 2740 (1997).

[124] K. Nakajima, “Laser-driven electron beam and radiation sources for basic, medical and industrial sciences”, Proc. Jpn. Acad., Ser. B **91**, 223–245 (2015).

[125] T. Kopyciuk, “Deexcitation of one-dimensional Rydberg atoms with a chirped train of half-cycle pulses”, Phys. Lett. A **374**, 34, 3464–3467 (2010).

[126] A. Takamine, R. Shiozuka, and H. Maeda, “Population redistribution of cold Rydberg atoms”, in Proceedings of the 12th International Conference on Low Energy Antiproton Physics (LEAP2016) (2017), p. 011025.

[127] I. S. Vogelius, L. B. Madsen, and M. Drewsen, “Rotational cooling of molecules using lamps”, J. Phys. B **37**, 4571–4574 (2004).

[128] T. Masahiko, M. Osamu, M. Shuji, and H. Masanori, “Generation of terahertz radiation by photomixing with dual- and multiple-mode lasers”, Semicond. Sci. Technol. **20**, 7, S151–S163 (2005).

[129] R. B. Kohlhaas, A. Rehn, S. Nellen, M. Koch, et al., “Terahertz quasi time-domain spectroscopy based on telecom technology for 1550 nm”, Opt. Express **25**, 11, 12851–12859 (2017).

[130] L. Cabaret, “Etude préliminaire d’un laser Cr:LiSAF émettant en bande large”, 2019.

[131] F. Tüngerthal from RPMC lasers, “Private communication”, 2020.

[132] T. W. Ducas, W. P. Spencer, A. G. Vaidyanathan, and W. H. Hamilton, “Detection of far-infrared radiation using Rydberg atoms”, Appl. Phys. Lett. **35**, 5, 382–384 (1979).

[133] L. Hollberg and J. L. Hall, “Measurement of the shift of Rydberg energy levels induced by blackbody radiation”, Phys. Rev. Lett. **53**, 3, 230 (1984).

[134] N. Ŝibalić, J. D. Pritchard, C. S. Adams, and K. J. Weatherill, “ARC: An open-source library for calculating properties of alkali Rydberg atoms”, Comput. Phys. Commun. **220**, 319–331 (2017).

[135] P. Chabert and N. Braithwaite, *Physics of radio-frequency plasmas* (Cambridge University Press, 2011).

[136] C. C. Goodyear and A. von Engel, “Dissociation and ionization of hydrogen in high frequency discharges”, Proc. Phys. Soc. **79**, 4, 732–740 (1962).

[137] P. C. Thonemann, J. Moffatt, D. Roaf, and J. H. Sanders, “The performance of a new radio-frequency ion source”, Proc. Phys. Soc. **61**, 5, 483–485 (1948).

[138] F. C. Fehsenfeld, K. M. Evenson, and H. P. Broida, “Microwave discharge cavities operating at 2450 MHz”, Rev. Sci. Instrum. **36**, 3, 294–298 (1965).

[139] R. W. McCullough, J. Geddes, A. Donnelly, M. Liehr, et al., “A new microwave discharge source for reactive atom beams”, Meas. Sci. Technol. **4**, 1, 79–82 (1993).

[140] D. Loggen, “A new hydrogen beam source for quantum bounce experiments - simulation and construction”, Master Thesis (Universität Wien, 2019).

[141] J. Curry from Opthos Instrument Company, “Private communication”, 2021.

[142] C. Malbrunot, M. Diermaier, M. C. Simon, C. Amsler, et al., “A hydrogen beam to characterize the ASACUSA antihydrogen hyperfine spectrometer”, Nucl. Instrum. Methods Phys. Res. A **935**, 110–120 (2019).

[143] C. Malbrunot, C. Amsler, S. A. Cuendis, H. Breuker, et al., “The ASACUSA antihydrogen and hydrogen program: results and prospects”, Philos. Trans. Royal Soc. A **376**, 2116, 20170273 (2018).

[144] W. L. Fite and R. T. Brackmann, “Collisions of Electrons with Hydrogen Atoms. I. Ionization”, Phys. Rev. **112**, 1141–1151 (1958).

[145] M. Giacomin, “Application of collisional radiative models for atomic and molecular hydrogen to a negative ion source for fusion”, Master Thesis (University of Padova, 2017).

[146] P. Chabert from Laboratoire de Physique des Plasmas, Ecole Polytechnique Paris, “Private communication”, 2020.

[147] I. H. Hutchinson, *Principles of plasma diagnostics*, 2nd ed. (Cambridge University Press, 2002).

[148] D. Wünderlich, S. Dietrich, and U. Fantz, “Application of a collisional radiative model to atomic hydrogen for diagnostic purposes”, J. Quant. Spectrosc. Radiat. **110**, 1, 62–71 (2009).

[149] P. Kulkarni, “Rydberg excitation of hydrogen for studies towards antihydrogen deexcitation”, Bachelor Thesis (Universität Leipzig, 2019).

[150] R. J. Damburg and V. V. Kolosov, “An asymptotic approach to the Stark effect for the hydrogen atoms”, J. Phys. B. **11**, 11 (1978).

[151] C. Bordas and H. Helm, “Electric-field ionization of Rydberg states of H_3”, Phys. Rev. A **47**, 1209–1219 (1993).

[152] J. D. Bekenstein and J. B. Krieger, “Stark Effect in Hydrogenic Atoms: Comparison of Fourth-Order Perturbation Theory with WKB Approximation”, Phys. Rev. **188**, 130–139 (1969).

[153] S. P. Alliluev and I. A. Malkin, “Calculations of the Stark effect in hydrogen atoms by using the dynamical symmetry $O(2,2) \times O(2)$”, Zh. Eksp. Teor. Fiz. **66**, 1283–1294 (1974).

[154] D. S. Bailey, J. R. Hiskes, and A. C. Riviere, “Electric field ionization probabilities for the hydrogen atom”, Nucl. Fusion **5**, 1, 41–46 (1965).

[155] *SIMION*, `https://simion.com`, Accessed: 2021-11-12.

[156] C. Killian from Stefan Meyer Institute of Subatomic Physics, Vienna, “Private communication”, 2021.

[157] F. Biraben, J. C. Garreau, L. Julien, and M. Allegrini, “A metastable hydrogen atomic beam: construction and characteristics”, Rev. Sci. Instrum. **61**, 5, 1468–1473 (1990).

[158] R. F. Stebbings, W. L. Fite, D. G. Hummer, and R. T. Brackmann, “Collisions of Electrons with Hydrogen Atoms. V. Excitation of Metastable $2S$ Hydrogen Atoms”, Phys. Rev. **119**, 1939–1945 (1960).

[159] G. A. Bickel and G. A. McRae, “Determination of the 1s–2s two-photon excitation cross-section in atomic hydrogen”, Spectrochim. Acta Part B **55**, 1, 57–63 (2000).

[160] K. C. Harvey, “Slow metastable atomic hydrogen beam by optical pumping”, J. Appl. Phys. **53**, 5, 3383–3386 (1982).

[161] R. G. Hulet and D. Kleppner, “Rydberg atoms in circular states”, Phys. Rev. Lett. **51**, 1430–1433 (1983).

[162] C. H. Cheng, C. Y. Lee, and T. F. Gallagher, “Production of circular Rydberg states with circularly polarized microwave fields”, Phys. Rev. Lett. **73**, 3078–3081 (1994).

[163] J. Hare, M. Gross, and P. Goy, “Circular atoms prepared by a new method of crossed electric and magnetic fields”, Phys. Rev. Lett. **61**, 1938–1941 (1988).

[164] R. Lutwak, J. Holley, P. P. Chang, S. Paine, et al., “Circular states of atomic hydrogen”, Phys. Rev. A **56**, 1443–1452 (1997).

[165] P. Lottigier, A. Jucha, L. Cabaret, C. Blondel, et al., “Single-mode scannable nanosecond Ti:sapphire laser for high-resolution two-photon absorption laser-induced fluorescence (TALIF)”, Appl. Phys. B **125**, 14 (2019).

[166] W. Li, “A boost to Rydberg quantum computing”, Nat. Phys. **16**, 820–821 (2020).

[167] M. Saffman, T. G. Walker, and K. K. Mølmer, “Quantum information with Rydberg atoms”, Rev. Mod. Phys. **82**, 2313–2363 (2010).

[168] E. Urban, T. A. Johnson, T. Henage, L. Isenhower, et al., “Observation of Rydberg blockade between two atoms”, Nat. Phys. **5**, 110–114 (2009).

[169] I. S. Madjarov, J. P. Covey, A. L. Shaw, J. Choi, et al., “High-fidelity entanglement and detection of alkaline-earth Rydberg atoms”, Nat. Phys. **16**, 857–861 (2020).

[170] H. Fan, S. Kumar, J. Sedlacek, H. Kübler, et al., “Atom based RF electric field sensing”, **48**, 20, 202001 (2015).

[171] A. Yang, Y. Peng, Y. Xu, and M. Liang, “Dispersion readout of micro-wave electric field using double-dark-state Rydberg atoms”, Laser Physics **29**, 4, 045201 (2019).

[172] C. S. Adams, J. D. Pritchard, and J. P. Shaffer, “Rydberg atom quantum technologies”, J. Phys. B **53**, 1, 012002 (2019).

[173] N. Prajapati, A. K. Robinson, E. B. Norrgard, M. T. Simons, et al., “Rydberg Atom-Based AC/DC Voltage Measurements”, in Conference on Lasers and Electro-Optics (2021), SW2I.2.

[174] N. Somaschi, V. Giesz, L. D. Santis, et al., “Near-optimal single-photon sources in the solid state”, Nat. Photonics **10**, 340–345 (2016).

[175] P. Senellart, G. Solomon, and A. White, “High-performance semiconductor quantum-dot single-photon sources”, Nat. Nanotech **12**, 1026–1039 (2017).

[176] F. Ripka, H. Kübler, R. Löw, and T. Pfau, “A room-temperature single-photon source based on strongly interacting Rydberg atoms”, Science **362**, 6413, 446–449 (2018).

[177] J. Schmidt, Y. Münzenmaier, P. Kaspar, P. Schalberger, et al., “An optogalvanic gas sensor based on Rydberg excitations”, J. Phys. B **53**, 9, 094001 (2020).

[178] *Qbyte*, `https://qbyte.io`, Accessed: 2021-11-07.

[179] *PASQAL*, `https://pasqal.io`, Accessed: 2021-11-07.

[180] *Rydberg Technologies*, `https://www.rydbergtechnologies.com`, Accessed: 2021-11-07.

6 CV

CV removed in online version